Trapping and cooling two-dimensional crystals of barium ions

Alexander Kato

A dissertation submitted in partial fulfillment
of the requirements for the degree of

Doctor of Philosophy

University of Washington

2022

Reading Committee:

Boris Blinov, Chair
Subhadeep Gupta
Kai-Mei Fu

Program Authorized to Offer Degree:
Physics

University of Washington

Abstract

Trapping and cooling two-dimensional crystals of barium ions

Alexander Kato

Chair of the Supervisory Committee:
Professor Boris Blinov
Department of Physics

The design and characterization of a trap specifically designed to create 2D crystals of trapped barium ions is presented. The trap is used to study the Doppler cooling of 2D crystals.

Ions in RF traps are subject to micromotion, a time-dependent driven motion caused by the RF fields themselves. This micromotion leads to Doppler shifts in laser-ion interactions. Laser cooling of 2D crystals can become increasingly difficult as crystals get bigger and are therefore subjected to more micromotion. We explore two methods for Doppler cooling in the presence of significant micromotion. The first method is to power broaden and detune cooling beams, reducing the distortions on atomic lineshape due to micromotion. The second method is to use nanosecond pulses of laser light synchronized with the trap RF in order to selectively cool the ions over a narrow range of velocities.

Contents

List of Figures

Acronyms

1D 1-dimensional. Referring to ions that crystallize in a straight line.

2D 2-dimensional. Referring to ions that form a shape that extends into a plane, but not into a third dimension.

3D 3-dimensional. Referring to ion crystals that extend into all 3 dimensions.

AOM Acousto-optic modulator. A photonic device that diffracts light using sound waves.

CCD Charge-coupled device. An imaging device where brightness information is stored in pixels as a charge and read out by summing along columns and rows.

CMOS Complementary metal-oxide-semiconductor. Each pixel has it's own amplifier and can be read out separately.

CPT Coherent Population Trapping . A phenomenon that occurs due to two-photon resonance in a three or higher level quantum system. Related to EIT.

DAQ Data acquisition. Usually referring to a device that collects digital or analog signals, or produces them.

DC Direct current. Voltage signal that does not change in time.

ECDL External Cavity Diode Laser. A laser diode with cavity formed by a diffraction grating, with reflection feeding back into the diode to enable single-frequency operation.

EIT Electromagnetically Induced Transparency. A phenomenon that occurs from two-photon resonance leading to transmission of light through an otherwise absorptive medium.

EMCCD Electron-multiplying CCD. A CCD device with an integrated electron multiplier that greatly increases sensitivity. These devices are often used for medical imaging, or more relevantly, ion trapping imaging.

FDM Finite difference method. A method of calculating spatial derivatives numerically by evaluating nearby points on a grid.

FWHM Full-width at half-maximum. The width of a curve (such as Gaussian) at half height.

GUI Graphical user interface. The interface for software with which a user interacts, usually on a computer.

HV High voltage. Voltages that are high enough to warrant special care, typically 100s to 1000s of V.

KTHNY Theory to describe melting in bulk 2D structures, named after J. Kosterlitz, D. Thouless, B. Halperin, D. Nelson, and A. Young.

MD Molecular dynamics. Typically, this refers to a simulations where particle position and velocity are tracked.

NA Numerical Aperture. The sine of the acceptance angle of an imaging system.

OBE Optical Bloch Equations. The equations that describe time evolution in a quantum system, found my using the Lindblad master equation.

OD Outer Diameter. Refers to the diameter of the outermost edges of a circular shaped object, such as a tube.

ODE Ordinary Differential Equation. Differential equations that only contain full derivatives with no partials.

PEEK Polyetheretherketone. A useful plastic that is compatible with UHV pressures.

PMT Photomultiplier tube. A device that converts photons into electrical pulses and is used to detect small amounts of light or single photons.

QE Quantum Efficiency. Overall efficiency in a device that uses quantum processes.

RF Radio frequency. This generally refers to frequencies in the 1 MHz-100 GHz range.

SWR Standing wave ratio. Typically, this refers to the ratio of forward and reflected signals in a transmission line, allowing one to determine resonant frequencies or perform impedance matching.

TDC Time-to-Digital converter. A device that times a signal using a digital output voltage.

ToA Time of Arrival. Timestamp of arrival of a signal or single photon.

ToT Time over threshold. The time a measured signal remains over a predetermined threshold value.

TTL Transistor-transistor logic. Protocol using bipolar transistors to achieve switching and maintain logic states. Typically, a square pulse in the range 3-5 V is used to trigger an instrument or operate a switch.

UHV Ultra-high vacuum. Generally referring to pressures below 10^{-8} Torr.

UW University of Washington.

Acknowledgements

There are a lot of people to thank for helping me achieve my goals. The story begins nearly 100 years ago in Vancouver. In the 1920s my great grandmother realized the value of education. Being Japanese Canadian, education meant a huge opportunity for advancement in society, and my great grandmother and great aunt Rose made huge sacrifices so that my grandfather, Yoichi, could continue to attend school. During the war, Japanese Canadians were sent to internment camps had their property seized, and my grandfather was removed from the University of British Columbia. Despite the odds, he was allowed to attend the University of Manitoba and graduated as an electrical engineer in 1945. His passion for education trickled down through the generations and was a driving factor in allowing me the means to as well as inspiring me to pursue my PhD.

Thanks to my first physics teacher, Mr. Trousdell, who always found a way to make physics exciting, from the legendary ninja quizzes to calculating "the force of love". Thanks to Jack Sankey at McGill taught me that working in a lab was actually fun. And I continue to steal his code. Thanks to my honours physics classmates, who truly humbled me.

Special thanks to Megan Ivory, who once upon a time took a chance on hiring me at ColdQuanta and let me be free range. Later on, I followed her to Boris's lab, where she started the 2D experiment and handed over the reigns before moving on to Sandia. Perhaps our paths will cross one day again. There are many people to thank at ColdQuanta. Thanks to Evan, Steve, Max, Hans, Kyle, Janet, Thad, Farhad, Dan, Jaime, Lisa, Joan, Steffen, Jayson, Mike, Marie, and Dana for making this a wonderful experience. Thanks to Seema for always making me feel included, and continuing to look out for me even after my time in Boulder. And thank you to Tom Noel, whose footsteps I followed in reverse. Finally, thanks to Jungsang Kim and and his lab members at Duke for inspiring me to continue on in ion trapping, and remembering me after I left ColdQuanta.

Thanks to my colleagues in the basement on the atomic physics side, Tahiyat Rahman and

Vasileous Niaouris, who provided many valuable conversations and made long days in the basement more bearable. Thanks to Professors Kai-Mei Fu and Subhadeep Gupta for providing much helpful advice, allowing me to borrow equipment, and for reading through the many pages of this dissertation. Thanks to Andrei Nomerotski at Brookhaven National Labs and hi student, Peter Svihra, for providing me the Tpx3 Cam and supporting me through its installation and use.

Thanks to all my lab mates for making the dark hours in the lab more pleasant: Jennifer Lilieholm and Liudmila Zhukas, Sara Branson, Carl Thomas, and Jane Gunnell, and the more recent students, Hunter Parker and Audrey Budlong. Thanks to the Master's students who I had the pleasure of working with: Leslie English and Samuel Goertz. And to the undergrads who worked on various aspects of my research: Ali Hassanzadeh, Gabriel Moureau, Raymond Lee, Apurva Goel, Zeyu Ye, Jian-Jun Liu, Samip Karki, Maverick Millican, Naomi Namba and Anisa Tapper.

In 2020 the pandemic began– thanks to my numerous roommates: Jared, Anthony, Josh, Dan Anna, and Dahli for getting me through this time. Thanks to my Bowen friends back home continue to remind me that life is not all about work.

Thanks to my parents Ron and Penny who always encouraged my interests and supported me in pursuing higher education, even though it wasn't in architecture. And to my brother Tim, who paved a path forwards and made it easy to follow. And of course thanks to my wife, Audrey for supporting me emotionally and financially through grad school and encouraging me all the way through. I couldn't have done it without you.

Finally, I must thank my advisor, Boris Blinov, for encouraging and tolerating me through my journey at UW. I appreciate Boris's hands on yet also hands off approach to labwork, always offering helpful suggestions for moving forward when I needed it but never looking over my shoulder. And thanks to Gorby for being my rock, day after day in the lab.

For Dahlia S.

Chapter 1

Introduction

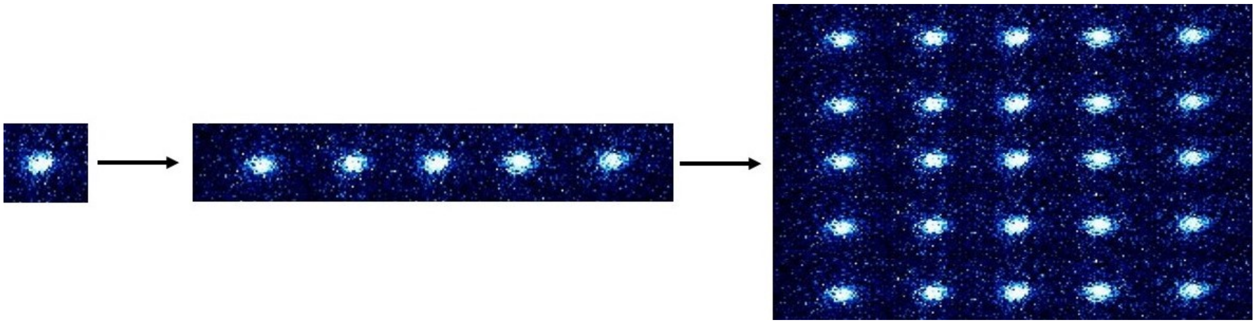

Figure 1.1: A single ion, a chain of ions, and a 2D lattice of ions. Scaling up a trapped ion quantum computer means increasing the number of usable qubits in a given area, which can potentially be achieved by by increasing the dimensionality.

Trapped ions are remarkably well-suited for quantum information applications. They are held in a UHV chamber that is lower in background pressure than atmosphere by 14 orders of magnitude, and cooled with lasers to mK temperatures and below, or 5 orders of magnitude lower than room temperature. Due to their charge, single ions repel each other and can be isolated in space, forming near-ideal qubits. The ions can then be further cooled towards their motional ground state. Additionally, trapped ions have sophisticated and well defined energy level structures, and every ion of the same species is identical. Combining these qualities together, trapped ions are one of the most ideal realization of a qubit that exists in nature.

1.1 Trapped ions in quantum information

The performance and quality of a quantum computer can be measured by several quantities, including coherence time and fidelity. Coherence time is a measure of how long information can be stored in a qubit before it is lost to noise in the environment. Fidelity describes how noisy target operation (single- or two-qubit gate, state preparation, or readout) is relative to the ideal operation.

In ions, certain energy levels may be used as the states that define a qubit. These energy levels can be particularly long-lived, meaning they make very good memories. In fact, for $^{171}\mathrm{Yb}^{+}$ the coherence time has been shown to exceed 1 hour [1]! At present, some of the most state-of-the-art quantum algorithms and quantum simulations have been performed with trapped ions. Single and two-qubit gates, state preparation, and readout, have all been conducted with high fidelities that should enable fault-tolerant quantum computing [2].

One criticism of trapped ion systems is the inability to scale up the system. *Scalability* describes increasing the useful size of the system in a sustainable way–that doesn't require excessive amounts of power, space, and complexity. The bulk of quantum information work with trapped ions has been performed in linear Paul traps. In these traps, ions form a line, or chain. Then individual ions in the chain can be addressed by lasers to perform single and multiple qubit operations. But what if we could extend this into two dimensions. Wouldn't having more ions, or qubits, be useful?

1.2 2D crystals of trapped ions

It turns out that we are not the first to consider using 2D arrays of ions for quantum information applications. But unfortunately, it is impossible to make the ideal square lattice in Fig. 1.1 in a standard ion trap. 2D crystals of trapped ions can be made in RF traps or Penning traps. Penning traps have produced some beautiful 2D crystals of hundreds of ions–an example is shown in Fig. 1.2. In Penning traps, 2D crystals are actively being pursued as a platform for quantum simulations and quantum information processing, with demonstrations of entanglement between hundreds of ions in a 2D lattice [3, 4, 5], and near-ground state cooling in a 100-ion crystal [6].

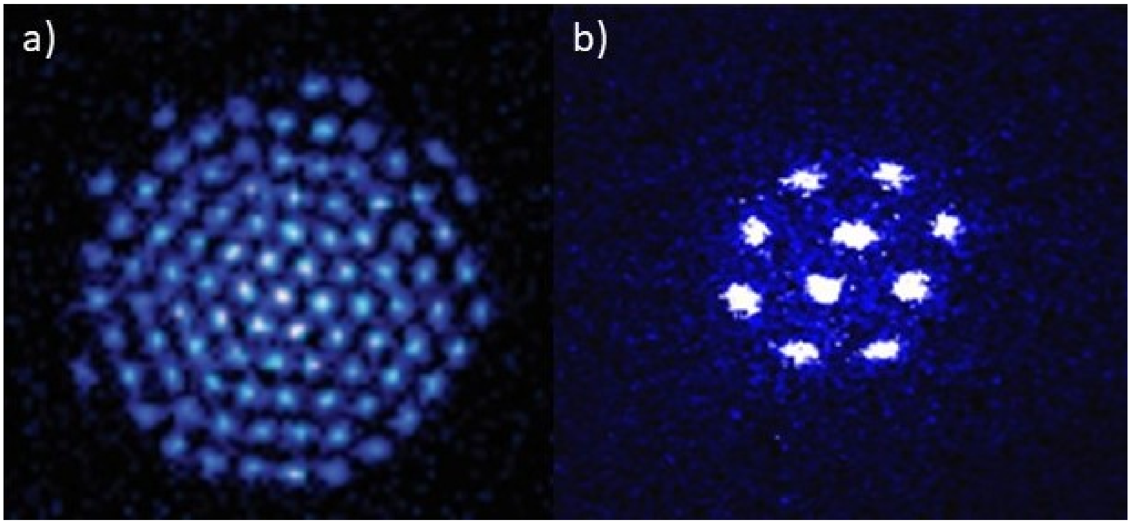

Figure 1.2: a) 94 ions in 2D crystal formation in a Penning trap from the Ion Storage Group at the National Institute of Standards and Technology [7]. Ions in penning traps are difficult to address individually with laser beams, which remains an outstanding challenge in quantum information processing. b) 10 ions in 2D formation produced in the Blinov group parabolic mirror ion trap.

But in a Penning trap, ions continuously rotate around the trap at 100s of kHz, a necessary condition to maintain confinement that lead to difficulties in addressing single qubits for quantum logic operations. Quantum information processing in Penning traps remains an active area of study, but is outside the scope of this dissertation.

RF traps can also produce 2D crystals. In RF traps, ions are statically confined and can be targeted individually by focused laser beams, making quantum gate operations much simpler logistically. However trapping and cooling large 2D crystals in RF traps remains a challenge. In this work, I focus on 2D crystals formed in RF traps, and the difficulties that come along with it.

1.3 Micromotion

Why aren't 2D crystals used in all ion trapping experiments for quantum information? The answer can largely be boiled down to a single word: micromotion. It turns out that ions in RF traps aren't actually static, but undergo small oscillations about an equilibrium position. Micromotion is a fast, driven motion that occurs in all RF traps and in contrast to other types of motion, it cannot be laser

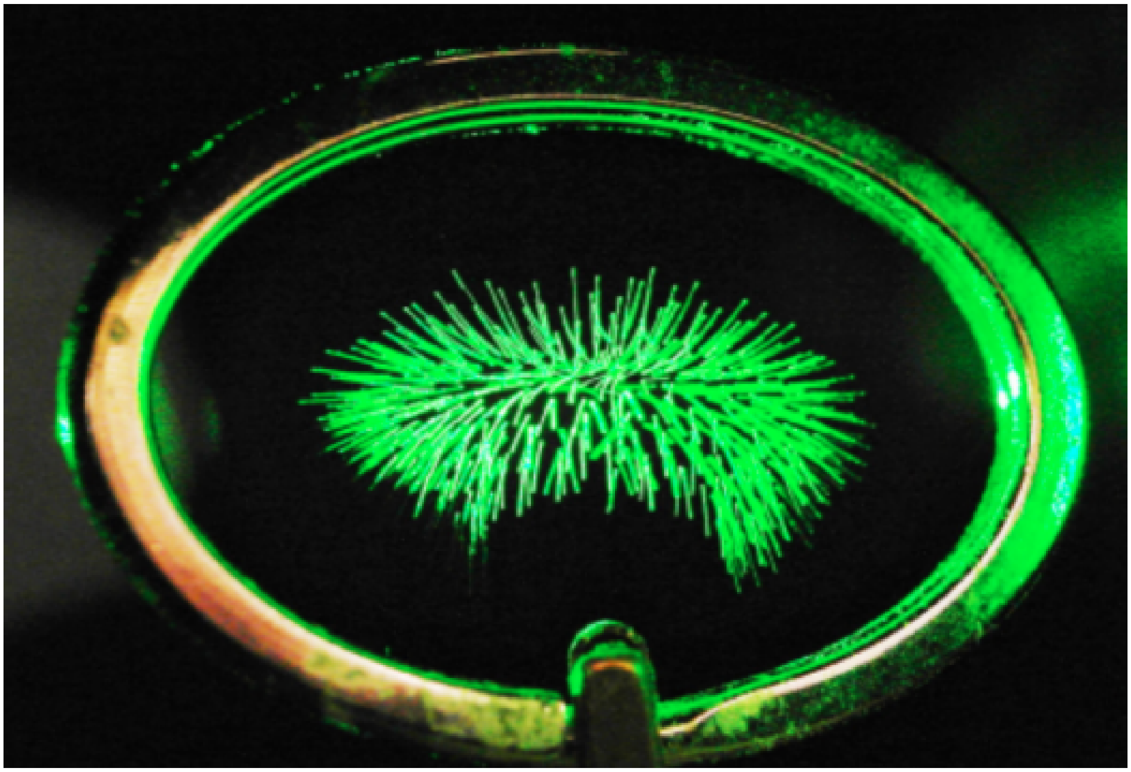

Figure 1.3: Excess micromotion in a microparticle ring trap [8]. These extended trajectories indicate a fast, periodic motion of the particles along the lines indicated. When micromotion in an ion trap occurs along the direction of a laser beam, this motion will effect the light-matter interactions through an apparent shift in the light frequency: the Doppler effect.

cooled.

Micromotion amplitude scales with the size of the crystal. Although in ion traps micromotion is often too small to see directly, in dust traps that also use RF to trap charged particles, the frequency of the drive voltage is sufficiently small that the particle covers a significant distance over one cycle and micromotion can be easily made out by the naked eye. An extreme example of micromotion is depicted in Fig. 1.3, which shows the extended trajectories of charged microparticles due to micromotion. Now consider a similarly structured crystal of trapped ions with a laser beam pointing through. Each ion has a different amplitude of micromotion, and points in a different direction. At any given time, the ions in the crystal have a large distribution of velocities with respect to the direction of travel of the laser beam.

What effect does this have on the interaction of the laser with the ions? Each ion is travelling at a slightly different velocity, so each ion is subject to a slightly different Doppler shift with respect to light being emitted from the laser. Moreover, the micromotion is time-dependent and leads to a frequency modulation. Finally, the amplitude of micromotion may exceed the spot size of a focused laser beam, which can lead to amplitude modulation.

This apparent frequency and amplitude modulation in the rest frame of the ions cause them to interact differently with lasers that are necessary for cooling and for performing qubit operations. Micromotion is a significant enough problem that ion trappers have primarily worked with linear ion traps [9, 10] or surface traps (see chapter 2), geometries that allows micromotion to be minimized.

Despite these problems, significant work has begun on using 2D crystals for quantum information. In this work, I focus specifically on the effect of micromotion on Doppler cooling–that is the initial stages of cooling that are essential for forming crystals in the first place, and a prerequisite for quantum information experiments.

1.4 Quantum information with 2D crystals

2D crystals of trapped ions represent a natural way to scale up the capabilities of trapped ions in a 1D chain [11, 12]. Error-correction is considered to be an important path for enabling the advancement of quantum computing [13, 14]. In particular, error correction can allow for fault-tolerance, or the limiting of the spread of error throughout the system [15]. Having more nearest neighbours, or qubits that occupy an adjacent lattice site as in a 2D crystal, may enable a higher error threshold for fault-tolerant quantum computing [16, 17]. In addition, quantum simulation of 2D systems such as spin liquids [18], frustrated systems [19], quantum magnetism [20], and spin-spin interaction [21, 22] may be more well suited to a native 2D geometry.

The main concern of micromotion is that it may push ions beyond the Lamb-Dicke regime [23, 24]–a regime where ions can be kept cold enough for high fidelity quantum logic operations. Moreover, micromotion leads to frequency and amplitude modulation in addressing beams [17], presenting further obstacles.

However, several recent proposals suggest 2D and 3D crystals may be used for quantum computing and simulations [17, 25, 26, 27, 28]. Quantum simulations with 2D crystals may be achieved by making use of transverse motional modes to generate entanglement [26, 27, 17]. To overcome the adverse effect of micromotion on gate fidelity, it has been shown that the segmenting of laser pulses used to address these motional modes may be used [17, 25].

1.5 Context of this work

In this dissertation I address difficulties of cooling 2D crystals due to ion micromotion to help enable the realization of 2D crystals as a platform for quantum information. Proposals for quantum computation and simulation with 2D crystals assume that the crystals can be initially trapped and stabilized, and laser cooled near the Doppler limit (chapter 3). Significant micromotion causes difficulties in Doppler cooling, the first stage of laser cooling with trapped ions that allows enough energy to be removed from the system before the ions get into an ordered formation (crystallize). Doppler cooling is typically a straightforward process for trapped 1D trapped ion crystals [24, 29], and the inability to perform this efficiently inhibits the ability to stabilize large 2D crystals in an RF trap.

Effective Doppler cooling of crystals where ions have both large and differing amplitudes of micromotion parallel to the cooling beam's k-vector remains an outstanding challenge. In this dissertation, I attempt to address this issue. Building up the necessary background in chapters 2 and 3, I will present a trap specifically designed for the production of 2D crystals in chapter 4. In chapter 5, I present realistic simulations of the trap potential and ion trajectories within the trap. In chapter 6 and 7, I demonstrate two techniques that may help enable more efficient Doppler cooling of large 2D crystals: two-tone cooling and pulsed cooling.

Chapter 2

Motion of trapped particles in oscillating electric fields

Our goal now is to understand how 2D crystals of trapped ions crystals form, and some of their properties. To do this we need to look at the equations of motion for a charged particle in an oscillating electric field that describe an ion trap.

2.1 Ion trap principles

A charged particle cannot be trapped at a stable equilibrium point in 3D by static electric fields alone. This is *Earnshaw's theorem.* The best we can do is create a trap in two out of three directions and an anti-trap in the third direction. A good intuition can be gained by considering a 2D saddle point potential. The potential surface would be described in 3D by the shape of a Pringle chip, as in Fig. 2.1. If you spin that saddle point, you can get a potential that confines a charged particle. This can be understood intuitively by considering a ball rolling on a saddle point. Without spinning, the ball will roll from its original position and eventually roll off of the saddle. However, if the saddle is spun at the right speed, the ball will not roll off of the saddle. As it rolls over the one of the outward sloping aspects of the saddle, it will roll towards the edge, and as it rolls over the inward sloping aspects, it will roll towards the centre of the saddle. The result is an oscillation around the ball's original position.

In 3D, such a potential is described in Cartesian coordinates by the equation

$$V(x,y,z) = Ax^2 + By^2 + Cz^2, \tag{2.1.1}$$

where one of the coefficients A, B, or C, is negative. Spinning the saddle point, we obtain

$$V(x,y,z) = (Ax^2 + By^2 + Cz^z)\cos(\Omega t). \tag{2.1.2}$$

It turns out that the equations of motion that can be derived from this support stable oscillations under the right conditions (coefficients A, B, and C as well as frequency Ω). This is explored in the following sections. The time-averaged behaviour of such a potential is often referred to as *pondermotive*.

Now just imagine a really small ball in a small but very rapidly rotating saddle. This is the basis of an RF ion trap. For a charged particle in an electric field, the energy due to the pondermotive potential can be described by a static, time-averaged quantity known as the *pseudopotential*, Φ. For a charged particle with mass m, and electric field rotating at Ω, we obtain the expression

$$\Phi(x,y) = \frac{e^2 \left|\vec{\nabla} V\right|^2}{4m\Omega^2}. \tag{2.1.3}$$

In Fig. 2.2 I have plotted Φ for $m = \Omega = e = 1$ for simplicity.

2.2 Hyperbolic Paul trap and equations of motion

The easiest way to obtain the quadrupole potential described by Eq. 2.1.1 is to shape the electrodes exactly in a hyperbola [31]. This trap is called the Paul trap, due to its development as an RF ion trap by Wolfgang Paul. In the ideal case one gets $A = B = -C/2$ The potential in the x- and y-directions is degenerate, and we refer to this as the radial direction. The z-direction is called the axial, or transverse direction.

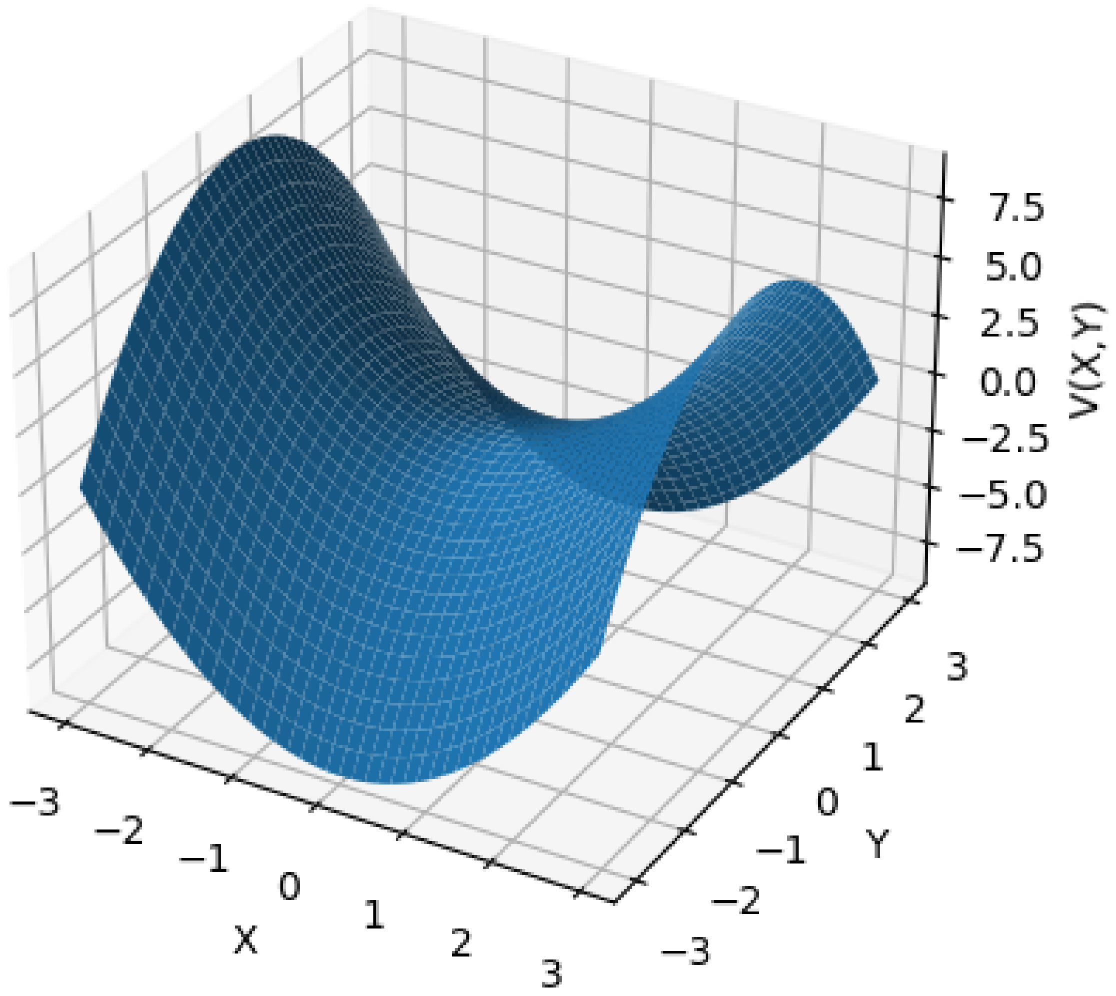

Figure 2.1: 2D Saddle point potential. An RF ion trap is a rotating saddle potential. At any given time, the ion is only confined in two out of three dimensions. Good demonstrations of how a rotating saddle can confine a ball can be found online [30].

The motion of an ion in an oscillating electric field is straightforward for a single ion in an electrode structure that produces a quadrupole potential, but quickly gets complicated for more complex electrode structures, and by introducing additional ions into the trap. To build up an understanding, I begin with the simple case of a single ion in a hyperbolic RF trap.

The motion of an ion in an oscillating potential is described by the Matthieu equation. For a hyperbolic electrode structure, the potential is given in cylindrical coordinates (r, θ, z) by [34]

$$V = \frac{V_0(r^2 - 2z^2)}{r_0^2 + 2z_0^2}, \tag{2.2.1}$$

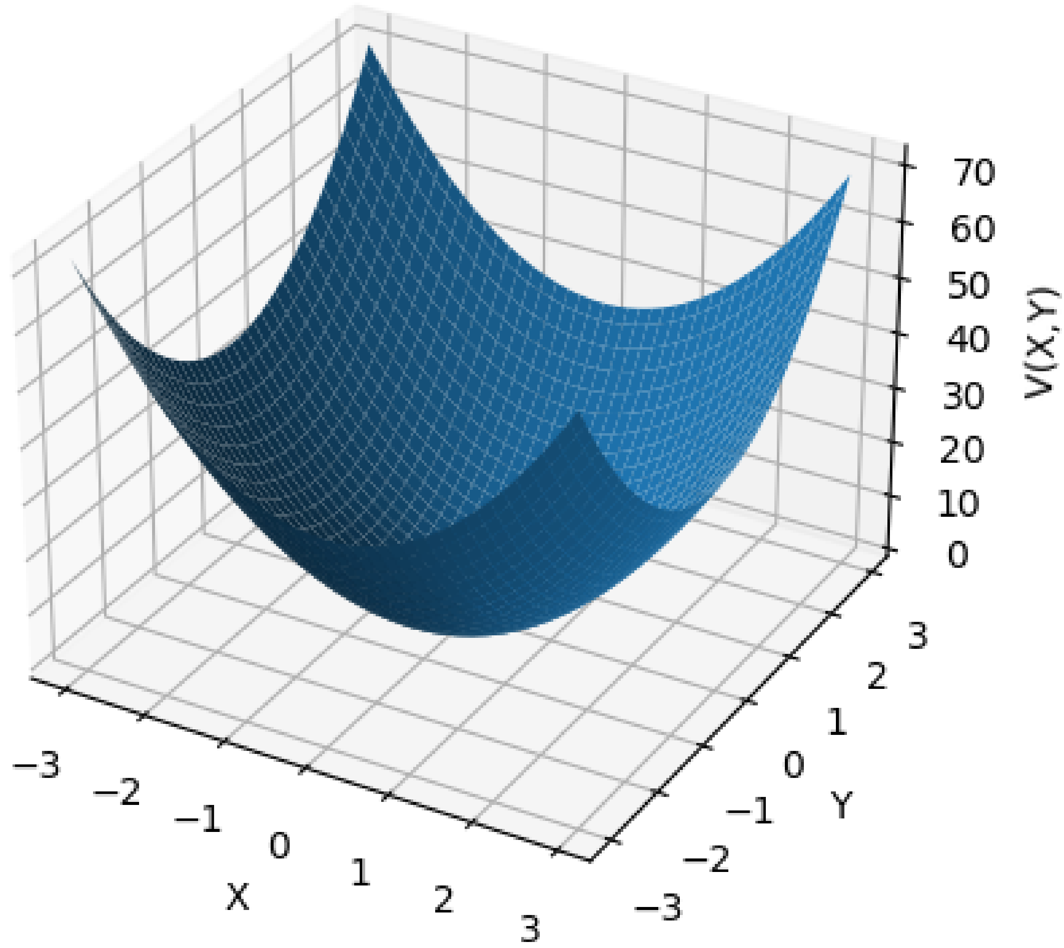

Figure 2.2: Pseudopotential surface described by Eq. 2.1.3. Choosing a particle of mass $m = 1$, we can compute the time averaged potential energy over a period of Ω.

where V_0 is the voltage applied to the endcap electrodes, r_0 is the radial distance to the ring electrode from the trap center, and z_0 is the distance to the endcap electrode. There is no angular dependence due to the symmetry of the hyperbolic geometry. For an ideal Paul trap,

$$2z_0^2 = r_0^2. \tag{2.2.2}$$

Applying both RF (at angular frequency Ω) and DC potentials to the trap, we obtain

$$V_0 = U_{DC} + U_{RF}\cos(\Omega t). \tag{2.2.3}$$

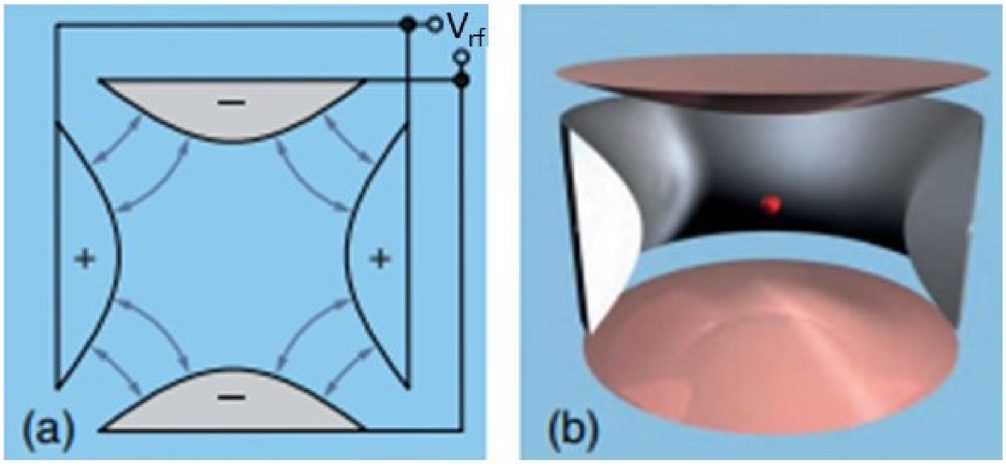

Figure 2.3: Schematic of a Paul trap. a) Snapshot of the RF voltage applied to electrodes. This configuration leads to a saddle point potential as shown in Fig. 2.1. b) Cross section view of the trap. Over a period of Ω a charged particle experiences a pondermotive force and remains localized. Reproduced from [2].

where U_{DC} and U_{RF} are the DC and RF potentials respectively. Now, given that the force on a singly charged particle (with elementary charge e) in an electric field is $\vec{F} = -e\vec{E}$, we differentiate the potential to obtain

$$F_z = \left(\frac{\partial V}{\partial z}\right)_r = \frac{4eVz}{r_0^2 + 2z_0^2}, \tag{2.2.4}$$

and

$$F_r = \left(\frac{\partial V}{\partial r}\right)_z = \frac{-2eVr}{r_0^2 + 2z_0^2}. \tag{2.2.5}$$

From here, we plug Eqs. 2.2.4-2.2.5 into $F = ma$ to obtain

$$m\ddot{z} = \frac{4e(U_{DC} + U_{RF}\cos(\Omega t)z}{r_0^2 + 2z_0^2} \tag{2.2.6}$$

and

$$m\ddot{r} = \frac{-2e(U_{DC} + U_{RF}\cos(\Omega t)r}{r_0^2 + 2z_0^2}. \tag{2.2.7}$$

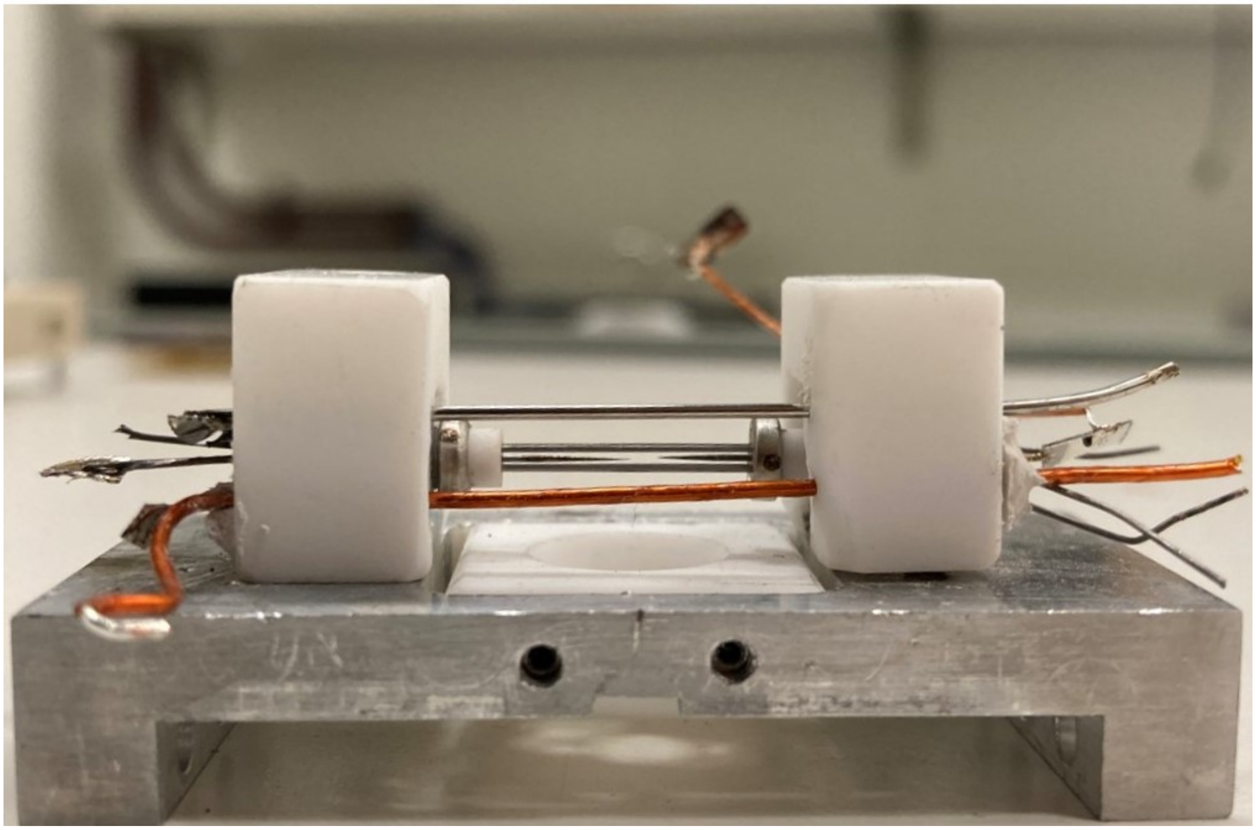

Figure 2.4: Photo of a Linear Paul Trap taken from our lab. This trap was used for experiments with single ions, and a study of the highly forbidden transition [32, 33].

We now introduce the Matthieu parameters

$$a_z = \frac{-16eU_{dc}}{m(r_0^2 + 2z_0^2)\Omega^2},\ a_r = -\frac{a_z}{2}, \tag{2.2.8}$$

and

$$q_z = \frac{8eU_{RF}}{m(r_0^2 + 2z_0^2)\Omega^2},\ q_r = -\frac{q_z}{2}. \tag{2.2.9}$$

Thus, we obtain

$$\ddot{z} + [a_z - 2q_z \cos(\Omega t)]\frac{\Omega^2}{4} z = 0, \tag{2.2.10}$$

and

$$\ddot{r} + [a_r - 2q_r \cos(\Omega t)]\frac{\Omega^2}{4} r = 0. \tag{2.2.11}$$

From here, one makes the substitution $\zeta = \frac{\Omega t}{2}$ to obtain

$$\frac{d^2x}{d\zeta^2} + [a_x - 2q_x \cos(2\zeta)]\,x = 0. \tag{2.2.12}$$

where $x = r, z$. This is the *Matthieu equation*, while a and q are known as the Matthieu parameters. For certain values of a, q, and Ω, the solutions are stable. For a thorough discussion of stability, please see [35] and [23].

It is useful to define the trap frequencies ω_i (here $i = r, z$), sometimes referred to as the secular frequencies. These are frequencies that describes the strength of a harmonic oscillator. The harmonic oscillator motion is called the secular motion, or thermal motion. In an ion trap, there are 3 such frequencies, one for each direction. For a Paul trap, the trap frequencies in the x and y directions are degenerate, and we have

$$\omega_r = \frac{eU_{RF}}{\sqrt{2}m\Omega r_0^2}, \tag{2.2.13}$$

and for the z direction (axial, or transverse direction)

$$\omega_z = \frac{\omega_r}{2}. \tag{2.2.14}$$

These frequencies are useful for quickly evaluating the feasibility of an ion trap given a certain trap size and availability of voltages and frequencies. For geometries that deviate from the ideal, additional simulations are needed in order to calculate these quantities. See chapter 5 for examples of how to estimate the trap frequency based off a given trap geometry.

The equations of motion are comprised of fast oscillations at frequency Ω (micromotion), and slower oscillations at the secular frequencies ω_i. For amplitude of secular motion r_1, the radial equation of motion for a single ion in an RF trap $r(t)$ around equilibrium position r_0 is

$$r(t) = r_0 + r_1 \cos(\omega_r t) + [r_0 + r_1 \cos(\omega_r t)]\frac{q_r}{2}\cos(\Omega t). \tag{2.2.15}$$

A similar equation describes the axial motion. For detailed visualizations of the motion of an ion in an RF trap, see chapter 5.

Some thermal motion is always present at frequency ω, and therefore some micromotion (at frequency Ω) is always present. However, if $r_0 \neq 0$, then we have additional micromotion. This is referred to as *excess micromotion*. Moving ions to a location where $r_0 = 0$ is referred to as minimizing micromotion, since at this point, the amplitude if micromotion cannot be further reduced. A point where micromotion can be minimized has zero electric field, and is sometimes referred to as the RF null.

2.3 Multiple ions in a trap

The forces due to that trap are the same for multiple ions, but now we must consider the Coulomb repulsion between ions. The equations of motion quickly become impossible to solve analytically. To solve for the trajectory of a particle we have the equation

$$\ddot{\vec{x}}_i + (a_x - 2q_x \cos(\Omega t))\frac{\Omega^2}{4}\vec{x}_i - \frac{e^2}{4\pi\varepsilon_0}\sum_i \frac{\vec{x}_i - \vec{x}_j}{\left\|\vec{x}_i - \vec{x}_j\right\|^3} = 0, \tag{2.3.1}$$

where $\vec{x}_i$ is the displacement vector of the i^{th} ion and ε_0 is the vacuum permittivity.

The approach is to solve the system of equations numerically. There are several ways to to this. By using Newton's method or similar, and providing reasonable guesses, one can find equilibrium positions for all of the ions. Or, one can numerically solve the differential equations using an ODE solver, and keep track of positions and velocities for all ions as they evolve in time. We take this approach, which may be broadly referred to as MD simulations. I explain these simulations in chapter 5.

2.4 Linear Paul trap, aspect ratio

Varying the electrode geometry can lead to alternative shapes of trapping potentials, and trap ions in different configurations. This can be described in terms of an *aspect ratio*

$$\alpha = \frac{\omega z}{\omega r}. \tag{2.4.1}$$

In an ideal hyperbolic trap, $\alpha = 2$.

Another configuration that has been extensively studied is the *linear Paul trap*. The quadrupole field is provided by four rods of alternating polarity and two distant endcaps, such as in Fig. 2.4. In this case α depends on the spacing of the endcaps compared to the distance between rods, but is typically quite small. The ions form a line, or chain along the trap axis, that runs along the centerline between the rods. This axis of symmetry is important when considering micromotion, and the reason that these RF traps are the most widely used for quantum information applications. For a linear trap, we typically have that $\alpha << 1$.

The aspect ratio is important because it defines the overall shape of the crystalline structures that form when the ions relax to equilibrium positions. To realize 2D crystals it is necessary to have $\alpha >> 1$. Several configurations of ions with increasing aspect ratio are shown in Fig. 2.5. Below we describe the rough shape that a crystal will take based on the range of α values considered.

$\omega_x \simeq \omega_y >> \omega_z$, $\alpha << 1$: Ions form in a line, as in Fig. 2.5 (a) and (b).

$\omega_x \simeq \omega_y > \omega_z$, $\alpha < 1$: Ions form in a zig-zag configuration, as in Fig. 2.5 (c).

$\omega_x \simeq \omega_y \simeq \omega_z$, $\alpha = 1$: Ions form in a spherical shape, with no preferred direction.

$\omega_x \simeq \omega_y < \omega_z$, $\alpha > 1$: Ions form in an oblate spheroid (that is, a spheroid compressed axially). For small numbers of ions, the crystal may be 2D.

$\omega_x \simeq \omega_y << \omega_z$, $\alpha >> 1$: Ions form in a 2D crystal configuration, as in Fig. 2.5 (d).

Detailed numerical studies of the 3D to 2D transition have been carried out to gain an understanding of the exact values of α that are needed [36]. It turns out that this occurs when

$$\alpha^2 = \sqrt{\frac{96N}{\pi^3\eta^3}}, \tag{2.4.2}$$

where N is the number of ions and $\eta = 1.11$. This assumes that $\omega_x = \omega_y$, in the case that these frequencies are different, it is possible to create 2D crystals for lower values of α.

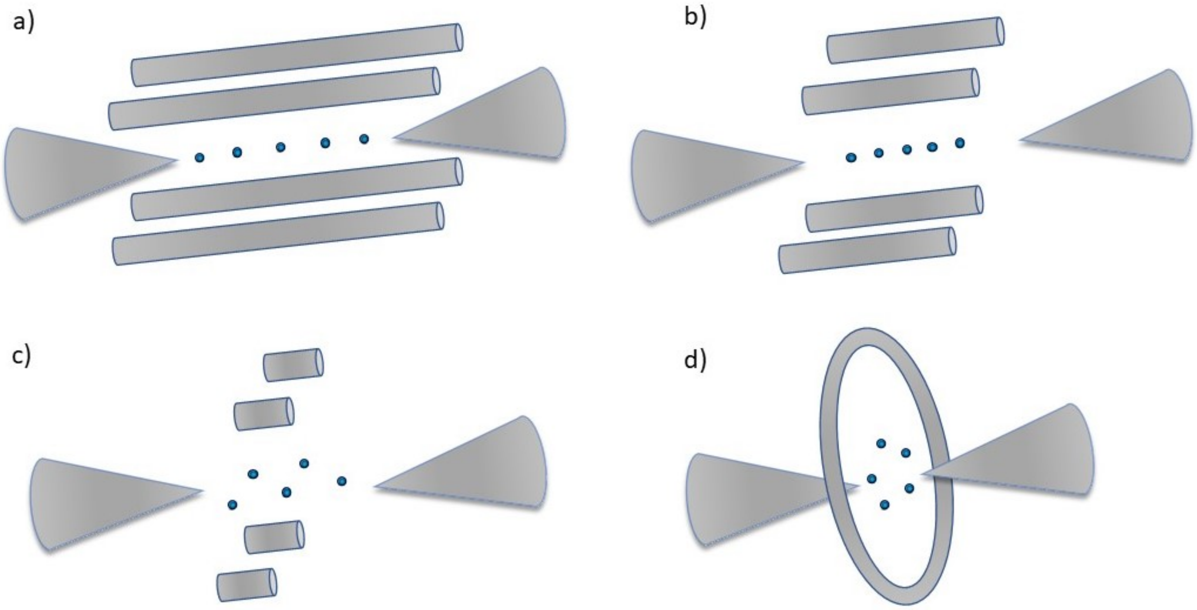

Figure 2.5: Visualization of the formation of 2D crystals ion a linear Paul trap. If enough DC voltage is applied to the endcap electrodes, the ions are forced into a planar formation. The same effect can be achieved by just bringing the endcaps close together. The panels (a-d) are described in the main text.

Chapter 3

Atomic and optical physics

3.1 Electronic structure, atomic transitions

Central to the discussion in this dissertation is atomic energy level structure, which is necessary to understand the dynamics of laser cooling. Atoms contain electrons that arrange themselves in orbitals that surround the nucleus of the atom. The structure of these orbitals give rise to discrete energy levels. Unpaired electrons may then be excited to different energy levels within this atomic structure. These are referred to as atomic, or electronic transitions. The details of these atomic transitions are extensive, and well described by former group members. I omit many details, and refer the reader to several excellent theses that explain these concepts [37, 38, 39] , and instead provide a brief description below.

In quantum mechanics or atomic physics, the hydrogen atom is commonly studied because of its simple electronic structure. Hydrogen has only a single electron and as a result the energy levels and atomic wavefunctions are much more easily understood and to a good approximation, can be solved analytically. As you increase in atomic number, the calculations quickly get much more complex. Additionally, the transitions are often higher in energy, making them difficult to access using lasers. However, atoms with a single valence electron can be understood by treating the atom as a large, hydrogen-like atom where the outer electron behaves in a similar manner, and typically

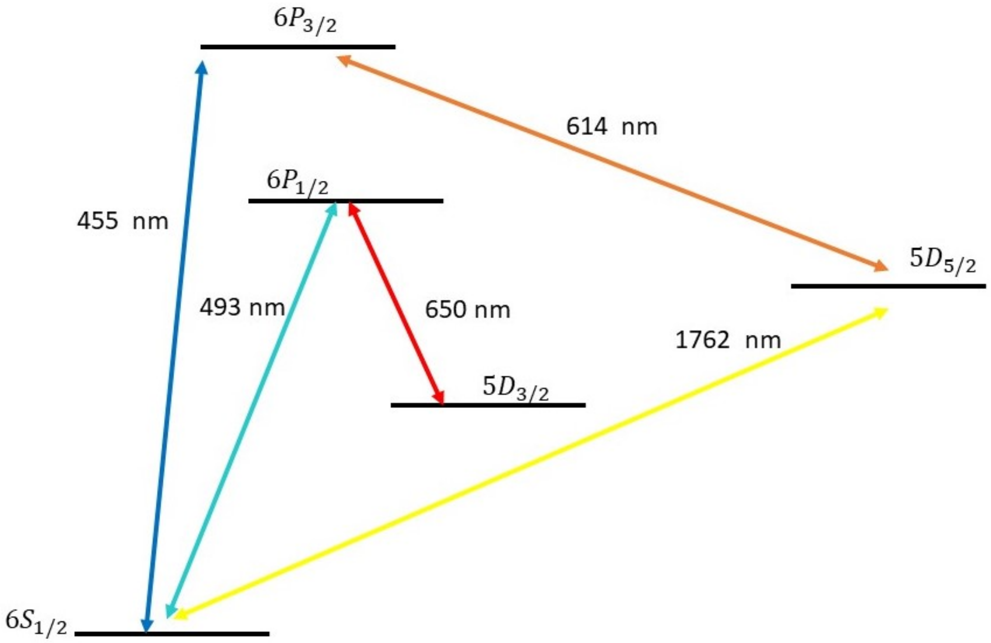

Figure 3.1: Partial energy level scheme for $^{138}\mathrm{Ba}^+$. The 493 nm and 650 nm transitions are used for Doppler cooling. The other transitions are used for the so called shelving to the $5D_{5/2}$ state, which is long-lived (metastable) and has many other applications in quantum information.

have many accessible transitions with commercially available lasers. For neutral atom physicists, these are the alkali metals (rubidium, cesium, potassium, sodium, lithium). Ion trappers like to use atoms that, when ionized, contain a single valence electron. Some of the most commonly trapped ions in physics labs are beryllium, magnesium, calcium, strontium and barium (more recently, radium! [40]).

Laser cooling was first demonstrated in 1978 [41] in Mg^+ at the. National Institute of Standards and Technology in Boulder, Colorado, and was closely followed in Ba^+ here at UW and Heidleberg [42], and has revolutionizing the field of atomic physics. One of the first species of trapped ions to be studied in depth was barium here at UW, and has been the continued species of choice ever since in our lab. Today, barium continues to be of interest as a qubit in a trapped-ion quantum computer. The partial energy level structure for $^{138}\mathrm{Ba}^+$ is shown in Fig. 3.1.

The mechanism of these transitions can be explained through an understanding of the wavefunction of the atom, and of the form of the external field that is driving the transition. The external field is often a laser, or microwave frequency source. The external field has a certain polarization and amplitude; both are used in calculations relating to atomic transitions.

The external field induces an electric dipole moment (or higher order moment) in the atom, which corresponds to a transition between two energy levels, with energy difference $E = \hbar\omega_0$ (ω_0 is the transition frequency). The transition electric dipole moment between two states $|i\rangle$ and $|j\rangle$ is given by

$$\vec{d_{ij}} = \langle i|\hat{d}|j\rangle\,, \tag{3.1.1}$$

where $\hat{d}$ is the dipole operator, $q\hat{r}$, and . Dividing by the charge q, Eq. 3.1.1 also describes what is known as the matrix element between the states $|i\rangle$ and $|j\rangle$.

The matrix elements describes the likelihood of transition based off of an integral of the overlap of the wavefunctions against the induced dipole moment. A dipole transition corresponding to two energy levels with large overlap is considered a strong transition, meaning that the excited state typically has a short lifetime. The natural linewidth of these transitions Γ is large. This property allows them to be addressed by lasers, which typically have a free-running linewidth less than that of the atomic transitions. Such transitions are ideal for laser cooling, where a high likelihood and short lifetime means an atom can scatter millions of photons per second, and thus experience a large net damping force.

The transition rate is conveniently described by the *Rabi frequency* χ_{ij}

$$\chi_{ij} = \frac{\vec{d_{ij}} \cdot \vec{E_0}}{\hbar}, \tag{3.1.2}$$

where $\vec{E_0}$ is the amplitude of the driving electric field. The quantity χ_{ij} evaluates the energy scale of the induced transition dipole moment in the presence of a resonant driving field. If on resonance in a ideal two-level system with no loss, χ_{ij} describes the frequency in which the population oscillates between the two states, known as the Rabi oscillations [43]. Please note my choice here to use χ instead of the usual Ω for the Rabi frequency, since Ω is already used to describe the RF frequency of the ion trap, and hence micromotion. We begin with the driven two-level system, the starting

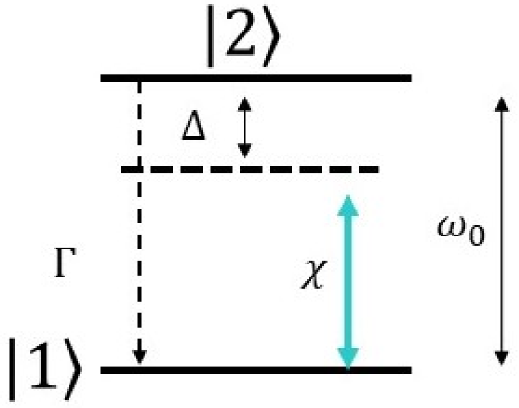

Figure 3.2: A two-level atomic system. The transition between states $|1\rangle \leftrightarrow |2\rangle$ is driven by external field (laser) with frequency detuned by Δ such that $\omega_L = \omega_0 - \Delta$, and Rabi frequency χ. The transition has natural linewidth Γ, causing decay back to the ground state.

point for understanding laser cooling.

3.2 Driven two-level system, steady state solutions

A two-level atomic system is the most simple case. Ions such as cadmium have closed two-level systems where the excited state has no probability of decaying to an outside energy level. This makes Doppler cooling easier, as only a single laser is needed. The excited state in barium ($6P_{1/2}$) actually decays to the $5D_{3/2}$ state approximately one in four times. Therefore, barium is actually a three-level Λ system, requiring a second laser. We will cover three-level systems in the following sections. However, a solid understanding of a two-level system is valuable in understanding atomic systems and Doppler cooling. We begin by looking for solutions to Schrödinger's equation for the wavefunction Ψ,

$$-\frac{i}{\hbar}\frac{\partial}{\partial t}\Psi = H\Psi. \tag{3.2.1}$$

The simplest solutions are steady state. Consider an two-level atom with energy splitting $E = \hbar\omega_0$, subjected to a laser of frequency ω_L and detuned from resonance by Δ, as indicated in Fig. 3.2.

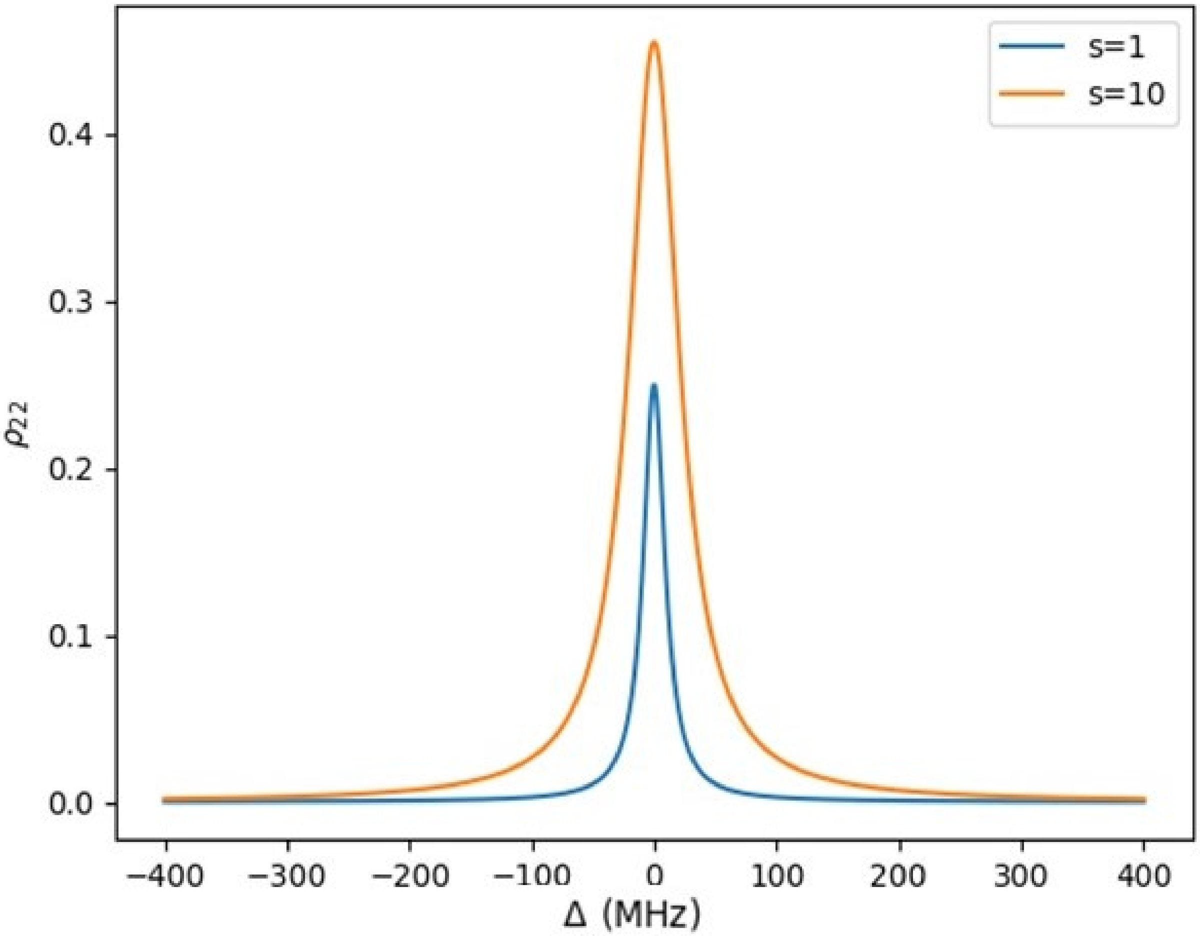

Figure 3.3: Atomic absorption spectrum for a two level system with $\Gamma = 15$ MHz (As with the main cooling transition in Ba$^+$. The two curves are for different values of s of 1 and 10. At higher power, the transition is broadened. The width scales as $\Gamma \to \Gamma\sqrt{1+s}$: This is power broadening.

In the basis of states $|1\rangle$ and $|2\rangle$, we have $H = H_0 + H_1$ with the unperturbed Hamiltonian

$$H_0 = \begin{bmatrix} 0 & 0 \\ 0 & \hbar\omega_0 \end{bmatrix}, \tag{3.2.2}$$

and the driven Hamiltonian, in the rotating wave approximation (see [43])

$$H_1 = \frac{\hbar}{2}\begin{bmatrix} 0 & \chi^* e^{i\omega_L t} \\ \chi e^{-i\omega_L t} & -i\Gamma \end{bmatrix}. \tag{3.2.3}$$

Note that this matrix is non-Hermetian, due to the loss term. Although this can cause issues with solving Schrödinger's equation, since this formalism ignores the time evolution of coherences (see section on density matrix formalism), we are only looking for steady state solutions. Eq. 3.2.1 can then be written

$$\frac{d}{dt}\begin{bmatrix} a_1(t) \\ a_2(t) \end{bmatrix} = -\frac{i}{2}\begin{bmatrix} 0 & \chi^* e^{i\omega_L t} \\ \chi e^{-i\omega_L t} & 2\omega_0 - i\Gamma \end{bmatrix}\begin{bmatrix} a_1(t) \\ a_2(t) \end{bmatrix}, \tag{3.2.4}$$

where $|\Psi\rangle = a_1(t)\,|1\rangle + a_2(t)\,|2\rangle$. The population of each state $|1\rangle$ and $|2\rangle$ is given by $|a_1(t)|^2$ and $|a_2(t)|^2$. Now, if we make the coordinate transformation $\tilde{a}_2 = a_2 e^{i\omega_L t}$ (going into the frame that rotates with the laser frequency ω_L), we get the equation

$$\frac{d}{dt}\begin{bmatrix} a_1(t) \\ \tilde{a}_2(t) \end{bmatrix} = -\frac{i}{2}\begin{bmatrix} 0 & \chi^* \\ \chi & 2\Delta - i\Gamma \end{bmatrix}\begin{bmatrix} a_1(t) \\ \tilde{a}_2(t) \end{bmatrix}. \tag{3.2.5}$$

From here, we look for steady state solutions. That is $\frac{d}{dt}a_2 = 0$ and $|a_1|^2 = 1 - |a_2|^2$. From this we obtain the solution for the excited state population $|a_2|^2$ (or in the density matrix formulation, ρ_{22}–see section 3.4 [43])

$$\rho_{22} = |a_2|^2 = \frac{\chi^2}{4\Delta^2 + 2\chi^2 + \Gamma^2}. \tag{3.2.6}$$

This equation is ubiquitous in atomic physics. The rate at which photons are scattered is simply $\Gamma\rho_{22}$. The population as a function of laser detuning is shown in Fig. 3.3 for $^{138}\text{Ba}^+$ with $\Gamma =$ 15 MHz. In this plot we also showing the the effect of increasing intensity through χ.

The shape of the absorption curve is a Lorentzian centered at zero detuning, with a width Γ. Increasing the power past saturation increases the scattering rate while broadening the line. The linewidth becomes $\Gamma \to \Gamma\sqrt{1+s}$, where s is the saturation parameter $s = I/I_{sat}$, and $I_{sat} = 2\frac{\chi^2}{\Gamma^2}$.

3.3 Laser cooling

We can exploit the atomic transitions to cool atoms and ions. Consider an ion moving at a constant velocity $\vec{v}$ towards the laser beam with wavevector $\vec{k}$, as in Fig. 3.4. Then the laser beam appears to be at a higher frequency in the ion's rest frame–this is the Doppler shift. For a laser positioned precisely at resonance for an ion at rest, a moving ion will experience a reduction in the scattering rate. However, if the laser is red-detuned, that is tuned below resonance, in the ion's rest frame the laser is nearly resonant. When this is the case, the interaction of photons with the ion tends to reduce the velocity of the ion in the direction of the laser, and thus results in cooling. This is known as *Doppler cooling*.

The force due to scattering is given by

$$\vec{F}_{scatt} = \hbar\vec{k}R_{scatt} = \hbar\vec{k}\Gamma\rho_{22}, \tag{3.3.1}$$

where $R_{scatt} = \Gamma\rho_{22}$ is the scattering rate, and $\hbar k$ is the momentum carried by each photon. Now, rewriting in terms of the saturation parameter s, and the rest frame detuning of the ion $\Delta \rightarrow \Delta - \vec{k}\cdot\vec{v}$, we get

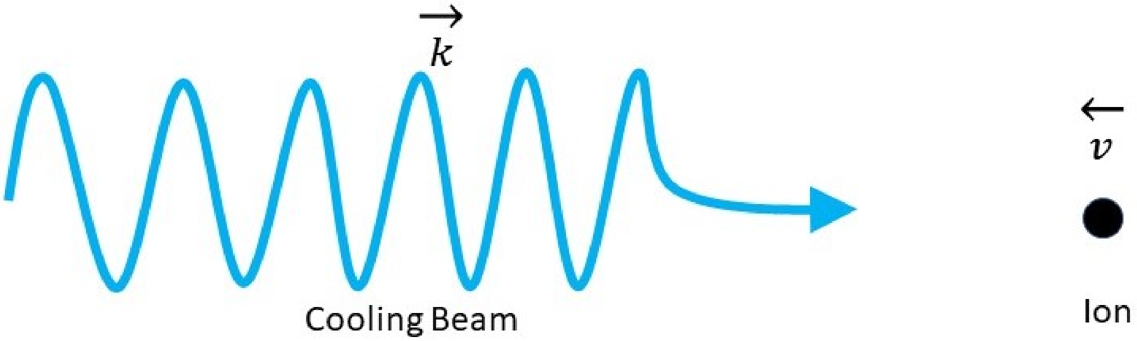

Figure 3.4: A laser beam with wavevector $\vec{k}$ incident on ion with velocity $\vec{v}$ produces a Doppler shift $\vec{k}\cdot\vec{v}$. A laser frequency may be detuned to selectively address ions according to their velocity. If we choose ions with a velocity that directly opposes $\vec{k}$, the ion will receive a momentum kick in the opposite direction to its motion, resulting in a net damping force.

$$\vec{F}_{scatt} = \hbar\vec{k}R_{scatt} = \hbar\vec{k}\frac{\Gamma}{2}\frac{s}{1+s+\left(\frac{2(\Delta-\vec{k}\cdot\vec{v})^2}{\Gamma}\right)^2}. \tag{3.3.2}$$

This expression may be hard to make sense of initially, but we Taylor expand in small v, and after some algebra we get an expression of the form

$$\vec{F}_{scatt} = \vec{F}_c - \gamma\vec{v}. \tag{3.3.3}$$

This means we have a constant force $\vec{F}_c$, and a term that is proportional and directly opposes the direction of the ion's velocity (damping coefficient γ), also known as a damping force. Because of the Taylor expansion, we know that this term must be proportional to the derivative of the scattering rate and hence the excited state population ρ_{22}, with respect to Δ. Therefore, we can get a good sense of where efficient cooling takes place by simply looking at the derivative of ρ_{22} with respect to the detuning Δ, which is plotted in Fig. 3.5 for the parameters used in Fig. 3.3.

Applying the Taylor expansion to Eq. 3.3.2, we obtain [44]

$$\vec{F}_{scatt} = \hbar\vec{k}\frac{s\Gamma}{2}\left(1+\frac{2\Delta(\vec{k}\cdot\vec{v})}{(1+s)(\Delta^2+\frac{\Gamma^2}{4})}\right). \tag{3.3.4}$$

However, the picture is still not complete. Every time a photon is absorbed, a photon must also be emitted. This imparts a momentum change $\hbar k$ in a random direction to the ion, leading to an increase in the root mean squared velocity $\overline{v^2}$. Equating $\frac{1}{2}k_bT = \frac{1}{2}m\overline{v^2}$ we find the minimum temperature that will be reached as a result of laser cooling. The coldest achievable temperature is known as the Doppler temperature (T_D) [43]:

$$T_D = \frac{\hbar\Gamma}{2k_B}. \tag{3.3.5}$$

The Doppler temperature is thus proportional to the linewidth of the transition used for cooling. For Ba$^+$, we get $T_D \simeq 3$ mK. This value is important for evaluating the quality of laser cooling of trapped ions. Although sub-Doppler cooling is possible, and often necessary for quantum information applications, efficient Doppler cooling is typically a prerequisite to even begin these processes. In summary, to gain intuition about the quality of laser cooling, we need only find the excited state population ρ_{22} and its derivative with respect to Δ.

3.4 3 level system, ^{138}Ba^{+}, density matrix formalism, optical Bloch equations

Many ions and atoms, including Ba^{+} have cooling cycles that involve a third energy level. We now generalize the previous sections to include this third level. However, the two-level model still

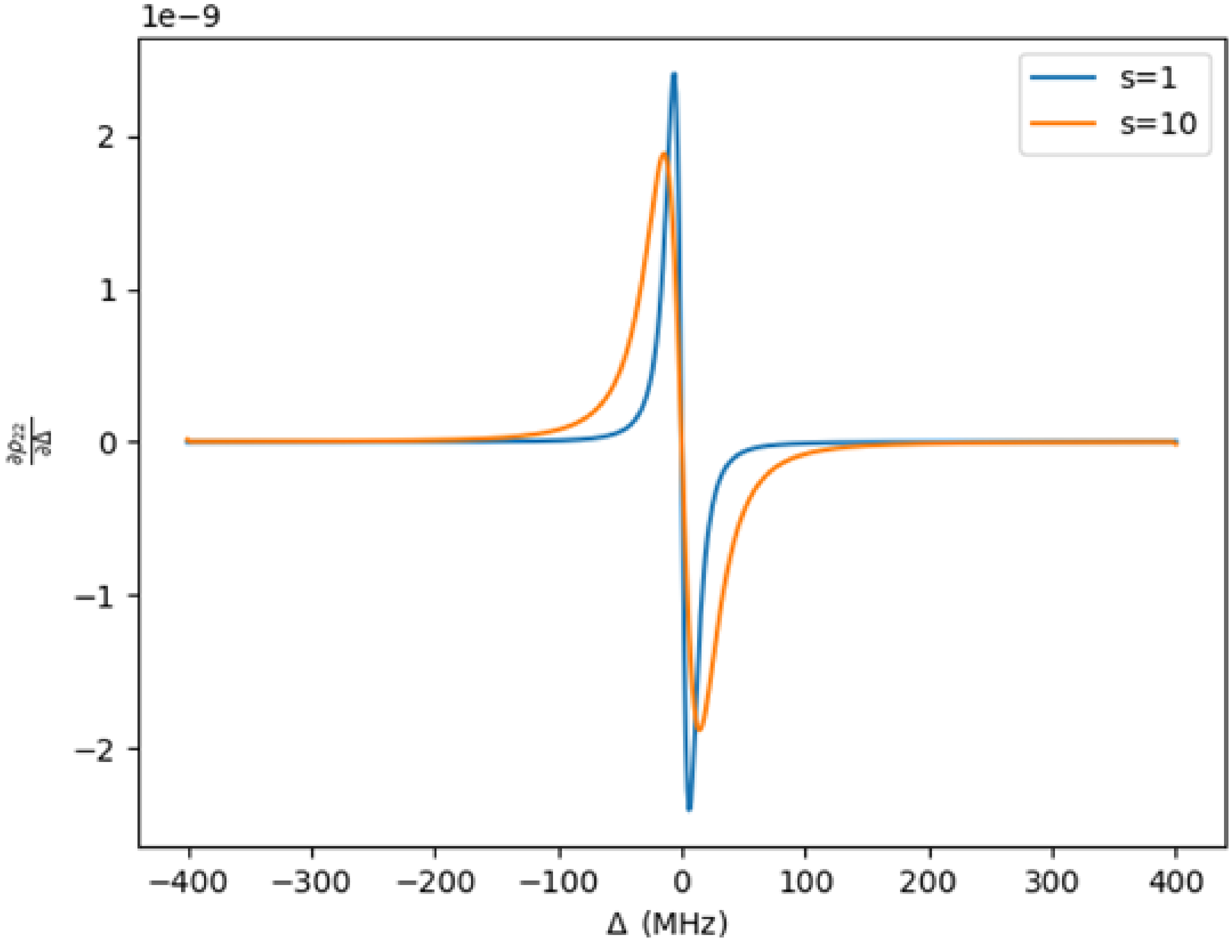

Figure 3.5: Derivative of ρ_{22} with respect to Δ for the two-level system, which is proportional to the rate of Doppler cooling.

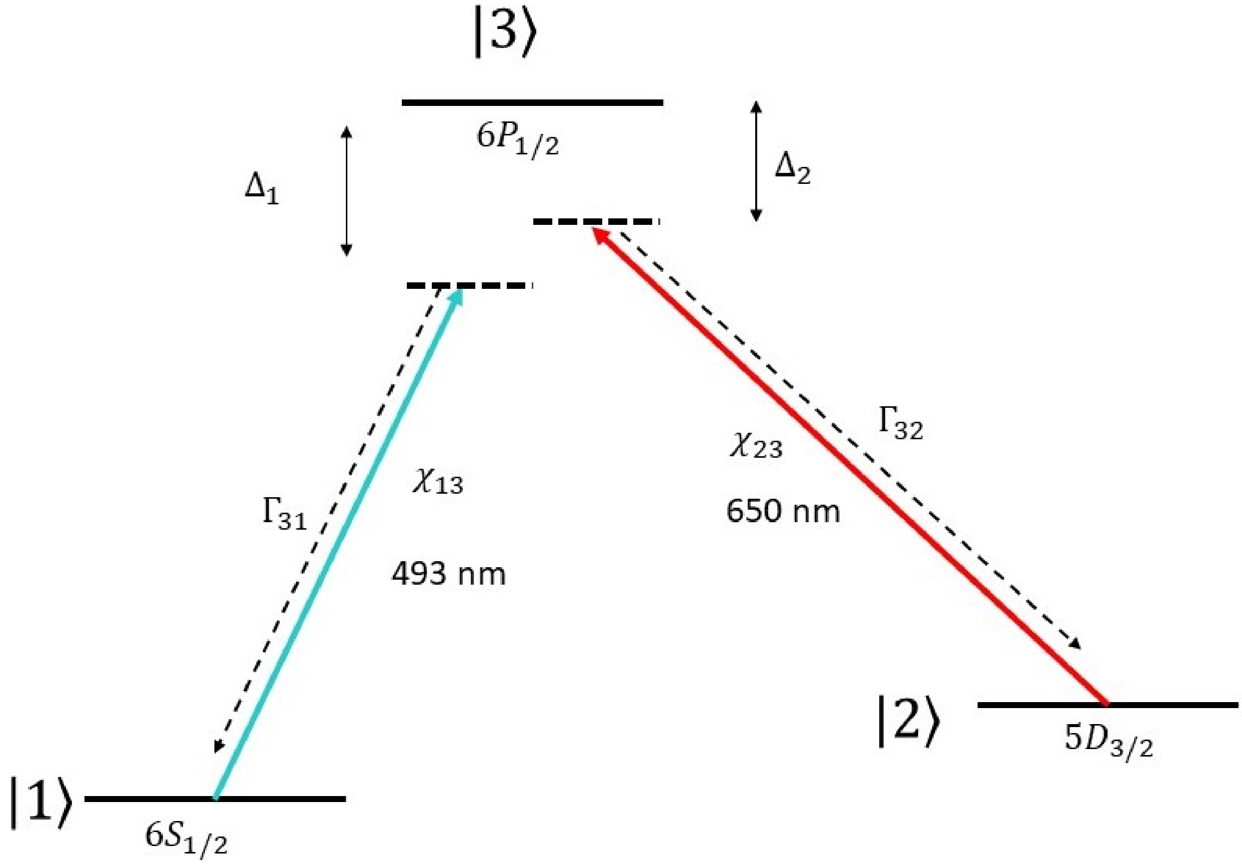

Figure 3.6: Schematic for the three level system that describes Doppler cooling in $^{138}\text{Ba}^+$. The cyan beam at 493 nm drives the $|1\rangle \leftrightarrow |3\rangle$ transition with Rabi frequency χ_{13}, detuning Δ_1, and natural linewidth Γ_{31}. Similarly, the red beam at 650 nm drives the $|2\rangle \leftrightarrow |3\rangle$, detuning Δ_2, and natural linewidth Γ_{32}.

provides many valuable insights and shares many of the same trends as in the three-level case.

One distinct difference when considering a three-level system in the steady state solution is that a coherent superposition of the two lower energy states can occur, with no population in the excited state. Since there can be no spontaneous emission from such a state, it is known as a "*dark state*". This behaviour is not captured using the same approach as in the previous section, since the evolution of the coherences is important.

We begin by writing down the Hamiltonian. Similarly to the two-level system, we use the rotating wave approximation and move to rotating coordinates to obtain (in the basis of states $|1\rangle$, $|2\rangle$, and $|3\rangle$, as depicted in Fig. 3.6)

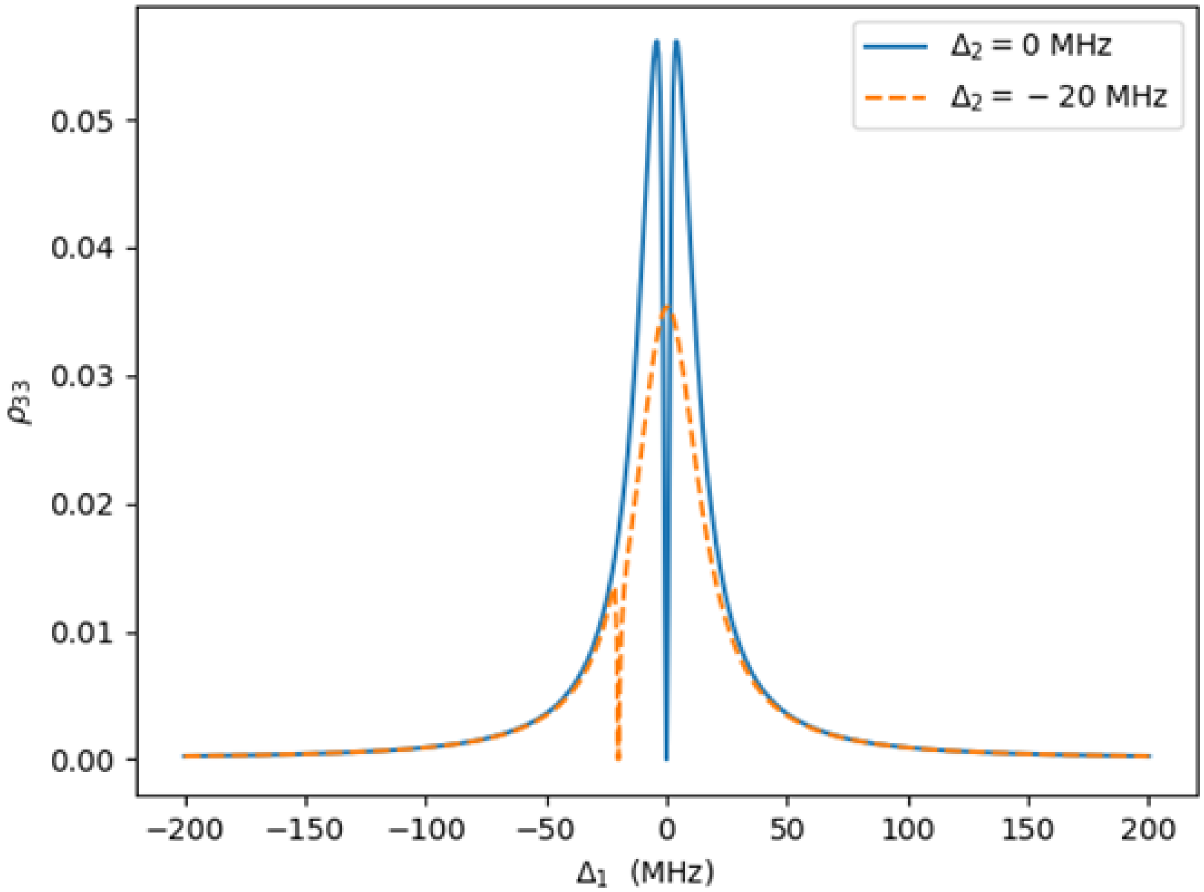

Figure 3.7: Absorption spectrum produced from solving the OBEs. The CPT appears where $\Delta_1 = \Delta_2$. For effective Doppler cooling, experimenters need to detune one of the two beams. Often the repump beam (laser that addresses the $|2\rangle \leftrightarrow |3\rangle$ transition) is detuned by 10s of MHz (dashed line).

$$H = \frac{\hbar}{2}\begin{bmatrix} -\Delta_1 & 0 & \chi_{13}^* \\ 0 & -\Delta_2 & \chi_{23}^* \\ \chi_{13} & \chi_{23} & (\Delta_1+\Delta_2) \end{bmatrix}. \tag{3.4.1}$$

We use the Linblad master equation to find the optical Bloch equations for the density matrix ρ

$$\dot{\rho} = \frac{i}{\hbar}[H,\rho] + \mathscr{L}(\rho), \tag{3.4.2}$$

Where $\mathscr{L}(\rho)$ is the *Louivillian* that describes loss of coherence and radiative decay. We have that

$$\mathscr{L}(\rho) = \sum_n \frac{1}{2}(2C_n\rho C_n^\dagger - \rho C_n^\dagger C_n - C_n^\dagger C_n \rho), \tag{3.4.3}$$

which is found by summing over the collapse operators C_n. We only consider radiative decay; thus, our only loss terms come from Γ_{31} and Γ_{32}. The collapse operators are $\sqrt{\Gamma_{31}}\,|3\rangle\langle 1|$ and $\sqrt{\Gamma_{32}}\,|3\rangle\langle 2|$. Writing down the elements of Eq. 3.4.2 we get the OBEs:

$$\dot{\rho}_{11} = i\frac{\chi_{13}}{2}(\rho_{31} - \rho_{13}) + \Gamma_{31}\rho_{33}, \tag{3.4.4}$$

$$\dot{\rho}_{22} = i\frac{\chi_{23}}{2}(\rho_{23} - \rho_{32}) + \Gamma_{32}\rho_{33}, \tag{3.4.5}$$

$$\dot{\rho}_{33} = -\dot{\rho}_{11} - \dot{\rho}_{22}, \tag{3.4.6}$$

$$\dot{\rho}_{21} = i\left((\Delta_1 - \Delta_2)\rho_{21} + \frac{\chi_{23}}{2}\rho_{31} - \frac{\chi_{13}}{2}\rho_{31}\right), \tag{3.4.7}$$

$$\dot{\rho}_{31} = i\left(\frac{\chi_{23}}{2}\rho_{21} + \Delta_1\rho_{31} + \frac{\chi_{13}}{2}(\rho_{11} - \rho_{33}) - \frac{1}{2}(\Gamma_{31} + \Gamma_{32})\rho_{31}\right), \tag{3.4.8}$$

$$\dot{\rho}_{32} = i\left(\frac{\chi_{13}}{2}\rho_{12} + \Delta_2\rho_{32} + \frac{\chi_{23}}{2}(\rho_{22} - \rho_{33}) - \frac{1}{2}(\Gamma_{31} + \Gamma_{32})\rho_{32}\right). \tag{3.4.9}$$

These equations are useful for studying dynamic situations as well as looking for steady state solutions, and are useful for numerically solving the three-level system.

The absorption spectrum for this system is similar to that of the two-level system, with the exception of the central dip, as seen in Fig. 3.7. This feature is caused by a coherent superposition of the states $|1\rangle$ and $|2\rangle$ that forms when both driving fields are on resonance, pushing the population into the dark state. This phenomenon is known as CPT, and may cause difficulties in cooling near the sharp gradients of ρ_{22} with respect to Δ_1. Therefore, it is necessary for experimenters to increase Δ_2, thereby moving the CPT feature away from resonance so that effective cooling can take place.

For numerically solving the equations, a number of available packages exist. Qutip is easy to

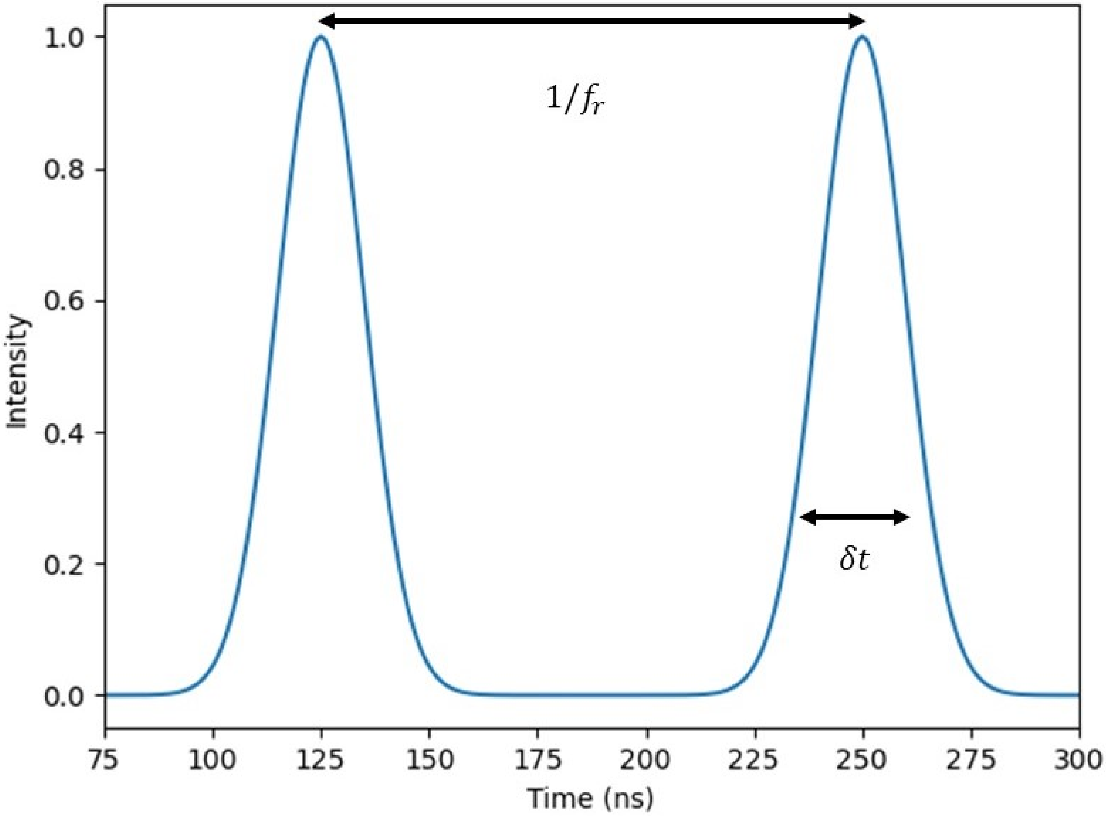

Figure 3.8: Portion of a pulse train of width $\delta t = 10$ ns and repetition rate $f_r = 8$ MHz. The resulting frequency comb is shown in Fig. 3.9.

get up and running to use for steady state solutions. For time dependent simulations, I found it necessary to use other solvers such as those found in SciPy. The steady state solutions to Eqs. 3.4.4-3.4.9 are used in chapter 6, while the time-dependent solutions are used in chapter 7.

The three-level model is still somewhat simplified from the real world picture. In fact, The Doppler cooling of $^{138}\text{Ba}^{+}$ is actually described by an eight-level system. This is because of the *Zeeman effect*–the splitting of energy levels of different spins in the presence of a magnetic field. A state with spin S is split into $2S+1$ sublevels. Therefore the $6S_{1/2}$ and $6P_{1/2}$ states are both split into two separate Zeeman sublevels, and the $5D_{3/2}$ into four. A small magnetic field is typically used to break the degeneracy of these states to prevent the ions from being pumped into a dark state. Zeeman splitting is typically small compared to the fine structure, and therefore the system is still well-approximated by a three-level system. A full treatment of the eight-level system is useful for understanding the full structure of dark resonances, and a good reference can be found in [45, 46].

3.5 Frequency comb

Briefly here, we will discuss the concept of a *frequency comb*, due to its relevance in chapter 7. A frequency comb is the resulting frequency spectrum of train of light pulses. Consider a monochromatic light source being pulsed at frequency f_r, with pulse width δt, as shown in Fig. 3.8. In frequency space, the light no longer monochromatic. The amplitude modulation leads to frequency sidebands, whose height and position depend on the pulse widths and separation. Frequency combs are a very active area of research, with a whole host of applications such as spectroscopy, frequency standards, and laser stabilization.

For example, in Fig. 3.8 we show a pulse train with repetition rate $f_r = 8$ MHz and pulse width $\delta t = 10$ ns, similar to the experiment in chapter 7. In Fig. 3.9, we plot the resulting Fourier transform, showing the position and strength of the comb teeth relative to the carrier. The envelope has width $\delta f = 1/\delta t$ with teeth spacing f_r.

3.6 Doppler cooling under micromotion

The greater the projection of micromotion in the direction $\vec{k}$ of cooling lasers, the worse cooling becomes. This is caused by variable Doppler shifts in the ion's rest frame as it moves back and forth over a period of micromotion. In terms of the OBEs in section 3.4, this means that we introduce a time dependence in Δ_1 and Δ_2. To understand how this affects the absorption spectrum and cooling, there are two approaches.

One approach is to solve for the steady state solution according to the OBEs for each point in the ion's micromotion trajectory, then time average the solutions. That is, to calculate the detunings due to the ions instantaneous velocity at each point, and solve the OBEs for each detuning. Since the absorptions of each beam are not correlated in time, we must average separately over each laser

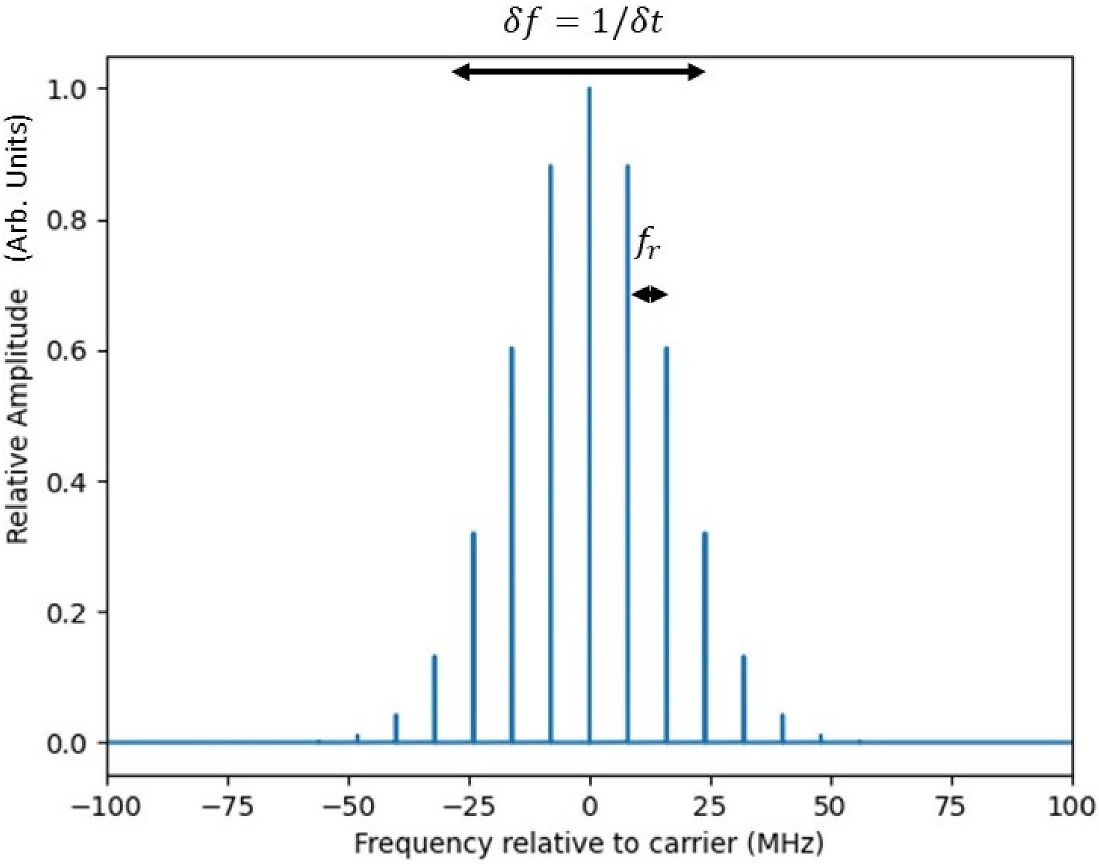

Figure 3.9: Fourier transform of the pulse train in Fig. 3.8. The comb width is given by $\delta f = 1/\delta t$ and the spacing of the teeth is f_r.

detuning. This is the approach taken in chapter 6.

The second approach is to assume that the system is not steady state. This is especially true for chapter 7, where we investigate pulsed laser cooling. Then the Rabi frequencies χ_{13} and χ_{23} are also time dependent, so it would be a poor assumption to look for steady state solutions. However, we are left with the problem of calculating an absorption spectrum. Without a steady state solution, the absorption spectrum is not well defined. Instead, we can find a quasi steady-state solution. Since the amplitude and frequency modulation both occur at fixed frequency Ω, we can time average the excited state population at each detuning over many RF periods. This approach produces an absorption spectrum that we can analyze, and is used in chapter 7.

Chapter 4

2D trapping system

In this section I describe the extensive infrastructure that is actually needed to run an ion trapping experiment. Although many of these components can be purchased, or are often built by a former graduate student in the lab, assembling all of the components is a significant task for a single graduate student. Building these components took me a a long time, so it is my hope that this section will help future graduate students in getting their experiments up and running more quickly.

4.1 Prior work with 2D crystals

After gaining some understanding of 2D crystals in the previous chapters, it is useful to briefly review the literature relating to 2D crystals of ions in RF traps.

2D crystals of ions in RF traps have been studied since some of the first demonstrations using hyperbolic traps in the 1980s [47, 48], with observations of phase transitions into ordered structures [48, 49]. However, after the introduction of the linear trap in the 1990s, 2D crystals were not given much attention. In the 2000s the crystalline structure of 2D crystals was explored [50] and theorists began to consider 2D crystals as a platform for quantum information [16, 51]. Several studies to understand the motional dynamics of ions in 2D crystals were also conducted [36, 52]. In the 2010s several groups began to investigate structural phase transition properties [53, 54]. Af-

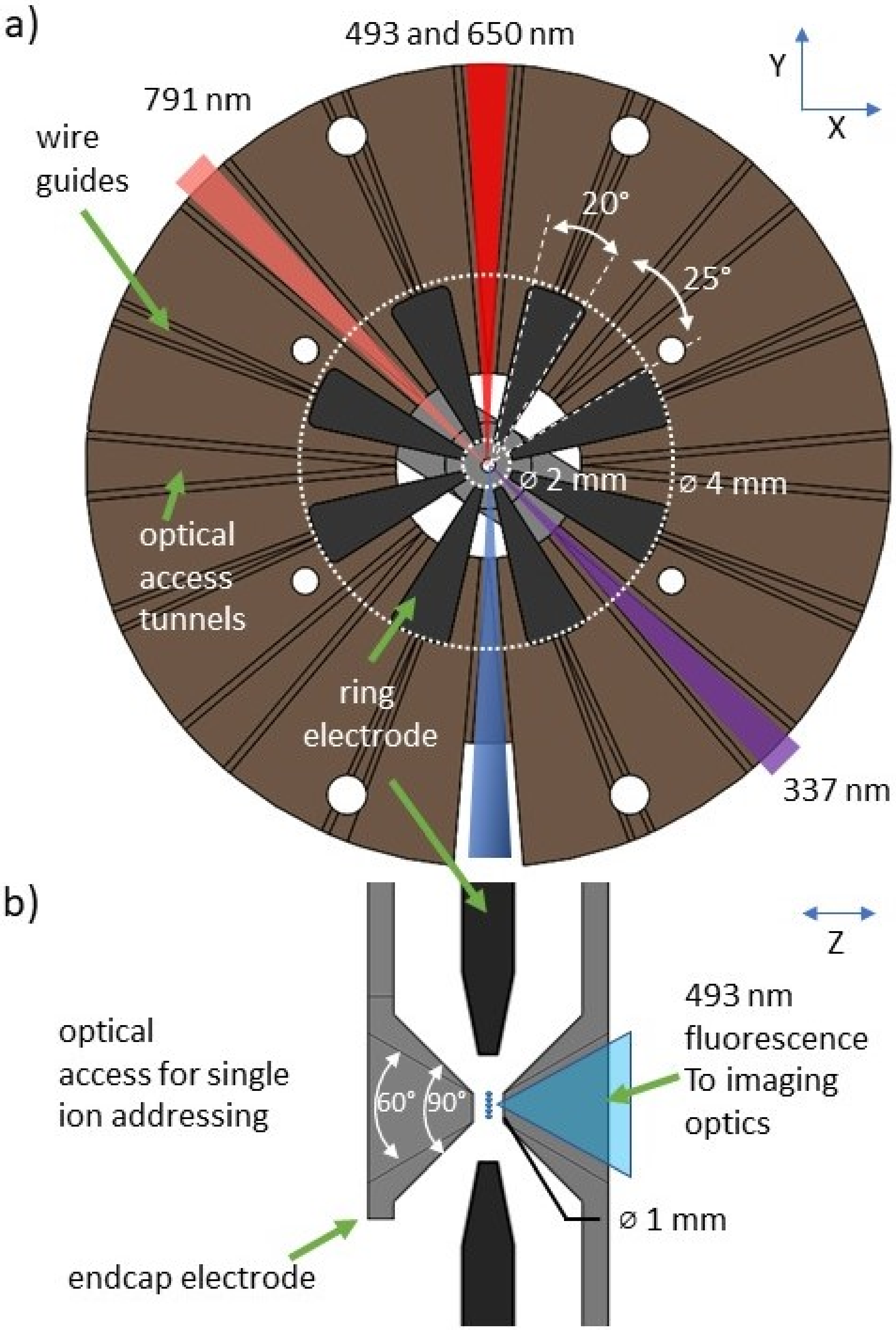

Figure 4.1: a) Cross-sectional view of the *xy* plane. The 8 ring sector electrodes are mounted on a PEEK structure with optical access tunnels and wire guides. b) Cross sectional view of the *xz* plane. The bored endcap electrodes provide strong transverse confinement while allowing high NA optical access for imaging and future single ion addressing.

ter proposals (section 1.4) were introduced to overcome micromotion in 2D crystals for quantum information, more 2D experiments have been introduced around the world that aim to perform quantum simulations. Experiments [55, 56] indicate that axial heating rates are at least two orders of magnitude lower than radial, and thus the transverse modes may be largely unaffected my micromotion and could be used to realize quantum simulations. Several new types of 2D traps were designed with these proposals in mind [25, 26, 57]. Both EIT cooling [56] and polarization gradient cooling [58], sub-Doppler cooling techniques that are useful for preparing a qubit register before performing quantum logic operations, have been demonstrated using 2D crystals. Finally, correlation spectroscopy has been performed on a 91 ion lateral 2D crystal [59] (more on lateral crystals in chapter 6). In our system, we focus on radial 2D crystals, the largest of which is 54 ions (chapter 6).

Although bulk phase transitions in 2D are well described by KTHNY theory [60], melting in finite 2D clusters is not as well understood. 2D crystals of charged particles, including ions, are an interesting platform to probe these transitions. Studies of melting and freezing have been performed numerically (for example [61, 62]), and experiments have been conducted using 2D crystals of charged microspheres (for example [63, 64]). More recently, ion trappers have begun to use 2D crystals to probe orientational melting [65]. Such experiments may be a future application of the trap described in this work.

4.2 The 2D trap

The trap was designed with 2D crystals in mind by Dr. Megan Ivory, a postdoc in our group. The goal was to develop a trap with an aspect ratio α that was natural to the formation of 2D crystals without significant application of static voltages. The design is loosely based off of another trap used to create 2D crystals [26]. This trap was a modification of a hyperbolic trap, containing a ring and two endcaps. In our case, the endcaps are hollow, truncated cones that allow for imaging of the 2D crystals. The ring is split into eight sectors, allowing for the shaping of the in-plane potential.

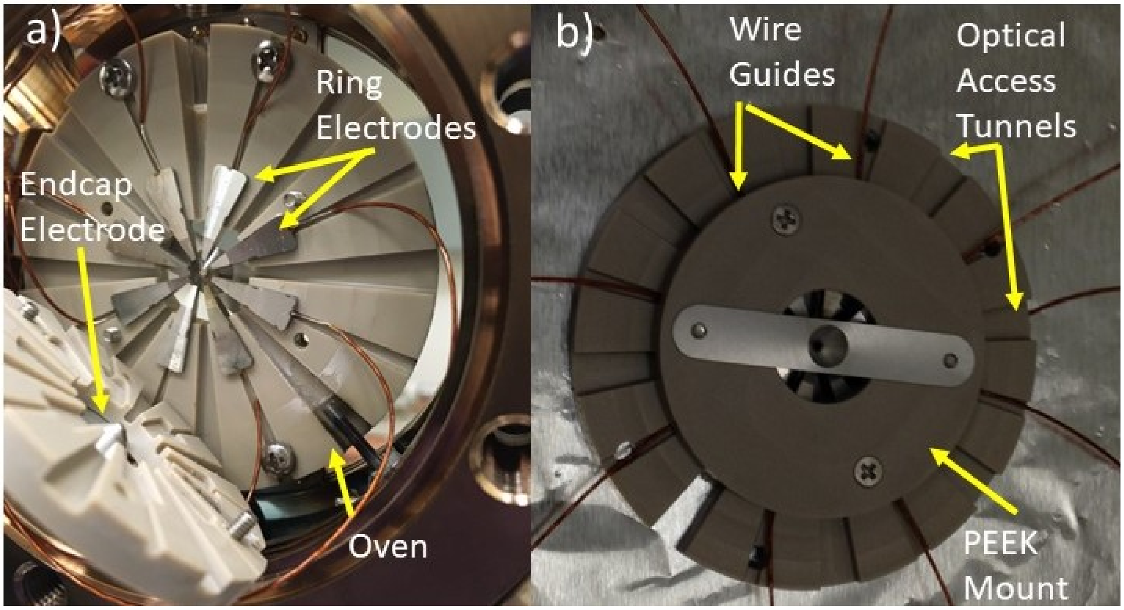

Figure 4.2: Images of the ion trap assembly. a) View of trap segments with half of PEEK structure removed and suspended. The trap electrodes and oven are visible. b) Assembled trap structure in PEEK mount. The mount contains grooves for optical access and provides a pathway for the wiring of the electrodes.

This allows the crystal shape to be adjusted. The trap schematic is shown in Fig. 4.1, with pictures in Fig. 4.2.

The sectored design also allows for optical access of the lasers for photoionization and cooling. In the y-direction, the 493 nm and 650 nm beams are copropagated (or counterpropagated, as in chapter 6). At a 45° angle (90° from the barium oven), the 791 nm laser and 337 nm laser allow for photoionization of neutral barium. The bored endcap electrodes allow for imaging (section 4.8) of the 2D crystals, as well as future optical access for single ion addressing beams.

The trap components were built by the UW Physics Department Instrument Shop. The sectored electrodes were machined out of stainless steel, while the endcap electrodes were electric-discharge machined and electropolished smooth to avoid charge buildup at burrs or edges. The results of this are shown in Fig. 4.3 for the endcap electrodes. Kapton-insulated wires are spot welded to connect each electrode to a 10-pin vacuum feedthrough. The electrodes are housed in an a machined structure composed of PEEK that contains radial tunnels for wire guides, laser access, and atomic beam for ion loading. The trap assembly is mounted in a 4.5” spherical octagon vacuum chamber

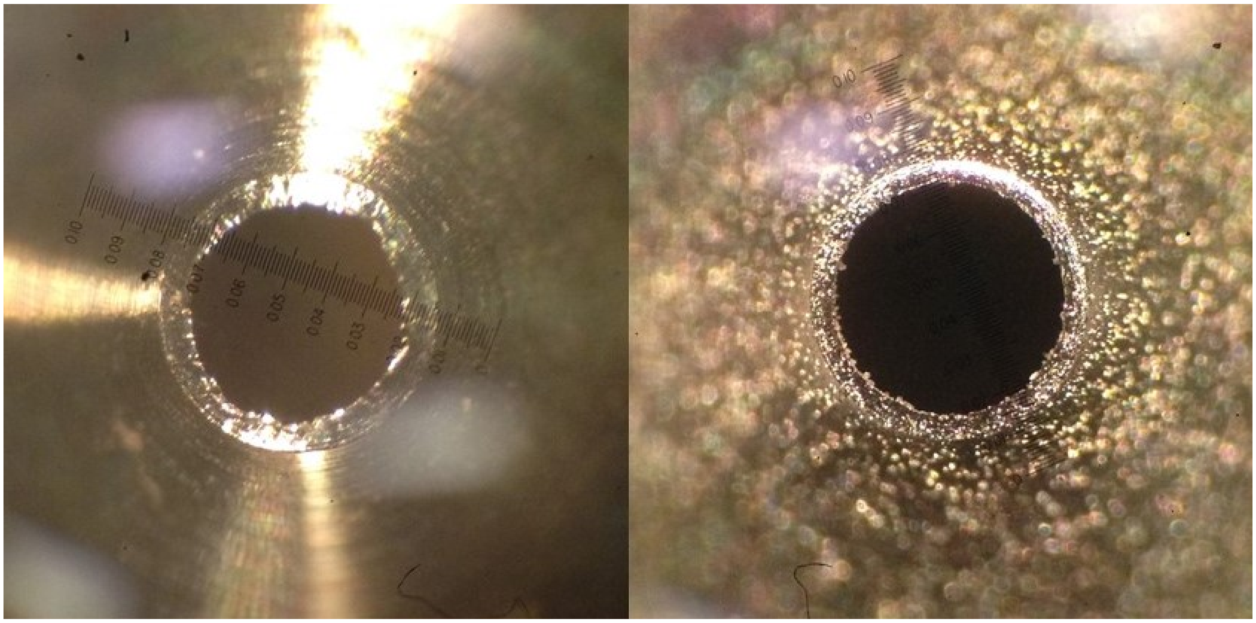

Figure 4.3: Left: unpolished endcap electrode, with scale in inches. Small jagged edges are visible on the inner circle. Right: After electropolishing, many small burrs have been removed. Lots of other material is also removed, however, the portion of the electrode closest to the ions (inner circle) is smoother.

(Kimball Physics part no. MCF450-SphOct-E2A8).

4.3 UHV system

The UHV system is extremely important in all ion trapping experiments. Background gasses will collide with the trapped ions, limiting the lifetime of ions and crystals. UHV pressures below 10^{-10} Torr are maintained using a Varian StarCell 20 L/s ion pump and an Agilent (formerly Varian) TSP-275 titanium sublimation pump. The pressure is read using an Agilent HV-24P Nude Bayard-Alpert Ion Gauge.

However, to reach the desired pressure from atmospheric conditions, $\sim 10^3$ Torr, several steps are required. Firstly, several stages of pumping are necessary to bring the system to a point where the UHV pumping mechanisms can be turned on. First, a roughing pump (diaphragm pump) is used to bring the system from atmosphere to 10^{-1} Torr. The a second stage of mechanical pumping (turbomolecular pump) is used to reach $\sim 10^{-8}$ Torr.

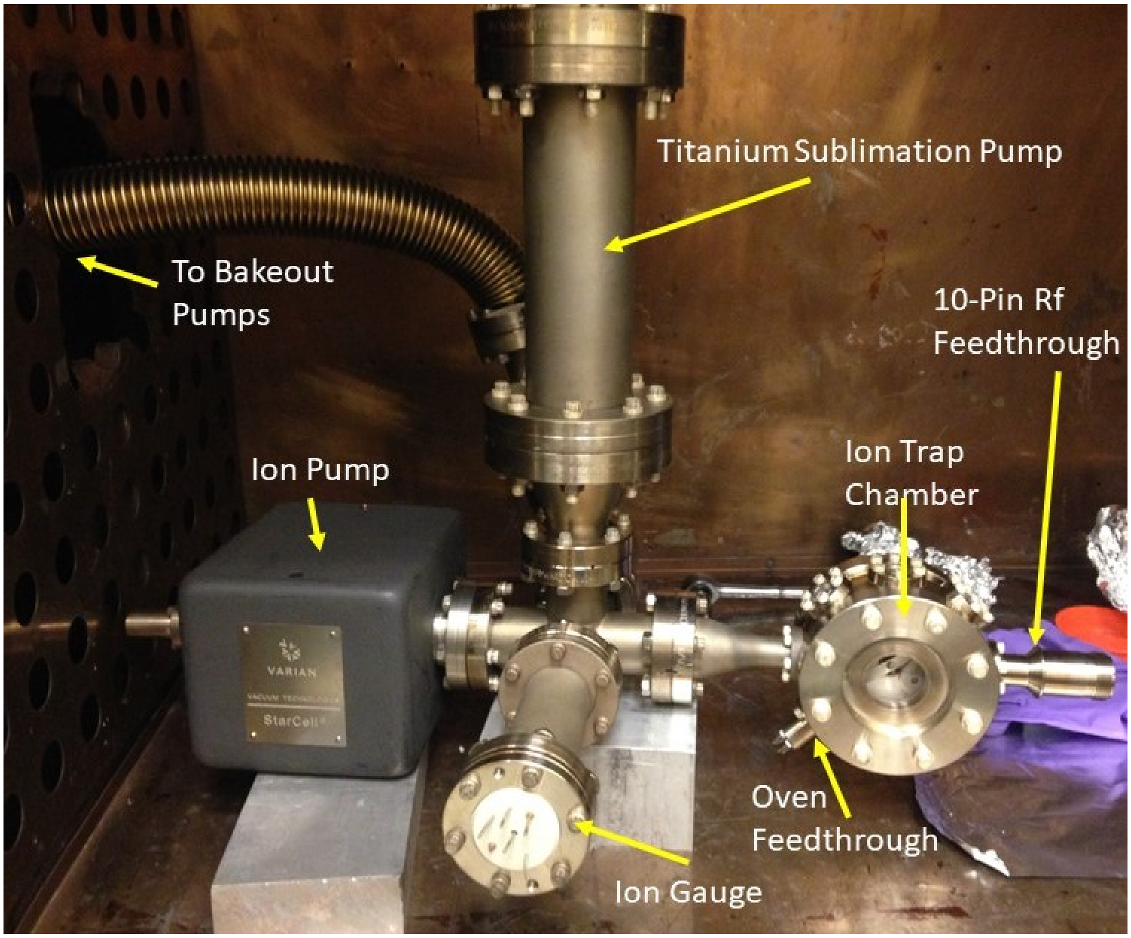

Figure 4.4: The UHV system containing the ion trapping chamber and all pumps necessary to maintain low pressures. This includes and ion pump and titanium sublimation pump, as well as an ion gauge for pressure measurement. The trapping chamber contains two electrical feedthroughs for power the atomic oven and driving the trap RF. The system is attached to the bakeout pumping station via a stainless steel hose.

At atmosphere, all materials are saturated with the water vapor present in air. Once the air is pumped out, the water vapor begins to outgas from the surfaces, limiting the pressure that is obtainable. Over time, the gas slowly escapes and the pressure lowers toward UHV levels.

This process could take many years, hence, another faster method is needed. Typically to reach UHV pressures, thye system is first baked. This simply means to heat up your vacuum system, causing an increased ougassing rate that speeds up the rate at which water vapor leaves the surfaces. The hotter the bakeout, the faster adsorbed gasses are released and a shorter duration of bakeout is needed. However, different components in the system typically have temperature limitations, such as wires, or plastics.

The UHV system attached to the bakeout oven is shown in Fig. 4.4. Our system is baked out around 130° C, chosen to prevent a glass transition in PEEK. The bakeout is performed inside a large isothermal convection oven. The system is attached to the roughing and turbomolecular pumps through a long hose that extends out of the oven. In addition, a large external ion pump is activated during bakeout. After bakeout (2 weeks), a valve on the system is sealed, and the system is removed from the oven and placed on the optics table.

4.4 Barium ovens

Atomic beam sources (ovens) were historically an easily manufactured and implemented part of the experiments in our group. However, since I joined the lab, we have been plagued by oven issues. Here I summarize the issues and the solutions that were uncovered.

Currently, our atomic ovens are formed using stainless steel hypodermic tubing with an OD of 1.8 mm and wall thickness of 0.3 mm, as seen in Fig. 4.5. These tubes can handle up to 15 A of DC current in vacuum before they overheat and burn out. These ovens usually emit barium for the first time at 13-14 A, where the temperature of the oven reaches the melting point of barium. After a first activation, the oven can operate at a much lower current (<7 A) to produce an atomic beam of barium. A sample picture of an oven is shown in Fig. 4.5 (a). The tubing is first cut with a diamond cutting tool on a Dremel, then spot welded to shim stock that makes up the leads that will eventually be connected to the UHV electrical feedthrough. The shim stock should be of similar thickness to the oven, so that it may have the same current carrying capacity. However, it must not be too thick, otherwise forming the leads and spot welding them are difficult.

As a general rule of thumb for spot welding, begin with a small amount of pulse energy and gradually turn it up as needed. If too much energy is applied, the part will explode, or be damaged. Wrap the shim stock around the tube and spot weld so that the spot welded electrodes never actually touch the tube itself. Otherwise you may put a hold in the tube. For the oven bottom, crimp shut and spot weld many times (use low energy so you don't add holes here either). Spot weld a second piece of shim stock here (not pictured), that will be used to connect to the electrical feedthrough. Once finished, clean the oven in an ultrasonic bath using a solvent such as methanol.

Next, spot weld the two shim stock leads to the electrical feedthrough (Fig. 4.6), taking care to keep the oven centered. There is some flexibility in the feedthrough pins, so it may be adjusted afterwards, by bending them with pliers. The oven should then be pre-activated–that is to heat it to its operating temperature so it expels much of the water vapor present. Barium is extremely reactive, so the presence of water vapor absorbed in the oven tube may cause the barium vapor to react before it reaches the trapping area. In addition, operating the oven causes additional outgassing at a higher rate. By ensuring the oven has already surpassed the operating temperature, we can reduce this effect.

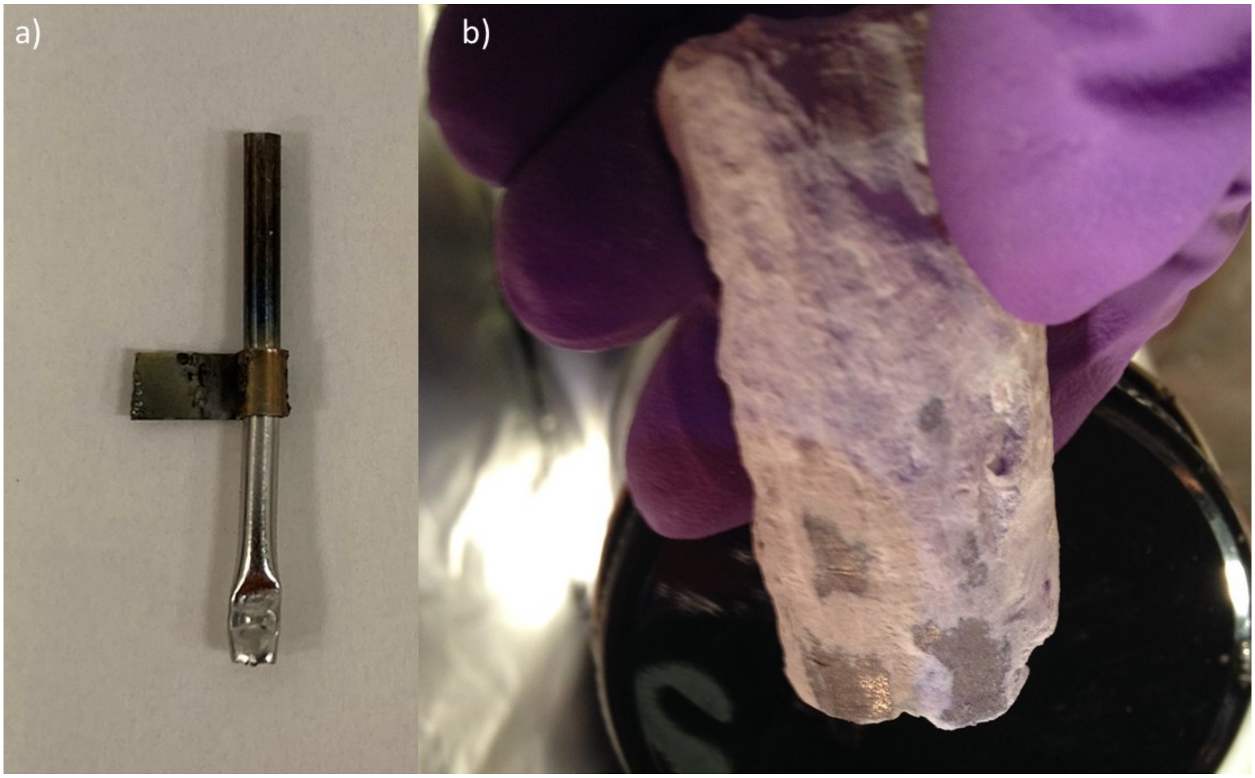

Figure 4.5: a) Atomic oven constructed from stainless steel hypodermic tubing. The leads are spot welded to the oven, and made from shim stock. b) Chunk of barium. The metal quickly grows thick oxide layer in atmosphere so loading must be done in an inert environment. A few small pieces of oxide have been slices off, and they shiny metallic barium is visible underneath.

With one of the large re-entrant viewports removed from the system (as pictured in Fig. 4.2), position the oven feedthough on the main chamber, making sure the oven does not touch any other material, especially PEEK, which will melt. Bolt the feedthrough onto the chamber. Direct the opening of the oven toward the trap center, ensuring there is line-of-sight from the oven. If necessary, install a makeshift shield (using shim stock or other material) that blocks line-of-sight from the opening of he oven to any viewport surfaces or electrical feedthroughs where it is undesirable to have any buildup of metallic film.

Bolt together and pump the system down using the rough pump and turbo pump. Then, incrementally turn the oven current up to 14 A and wait for 10 minutes. Turn the oven off, and allow

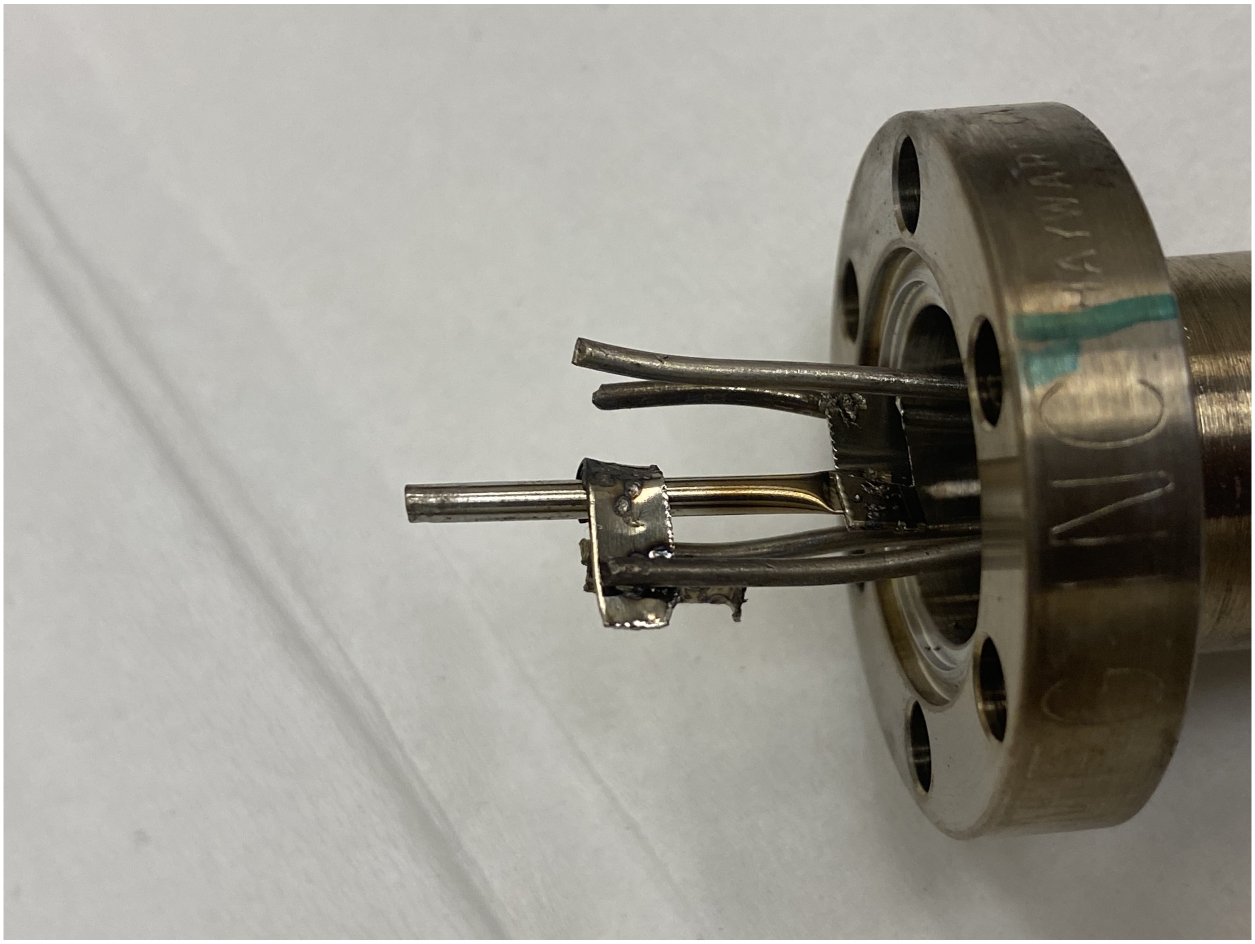

Figure 4.6: Barium oven spot welded to an electrical feedthrough. Make sure to position the leads such that they can be easily spot welded to the feedthrough while keeping the oven centered. Too much bending will cause stress in the oven and may cause it to fail.

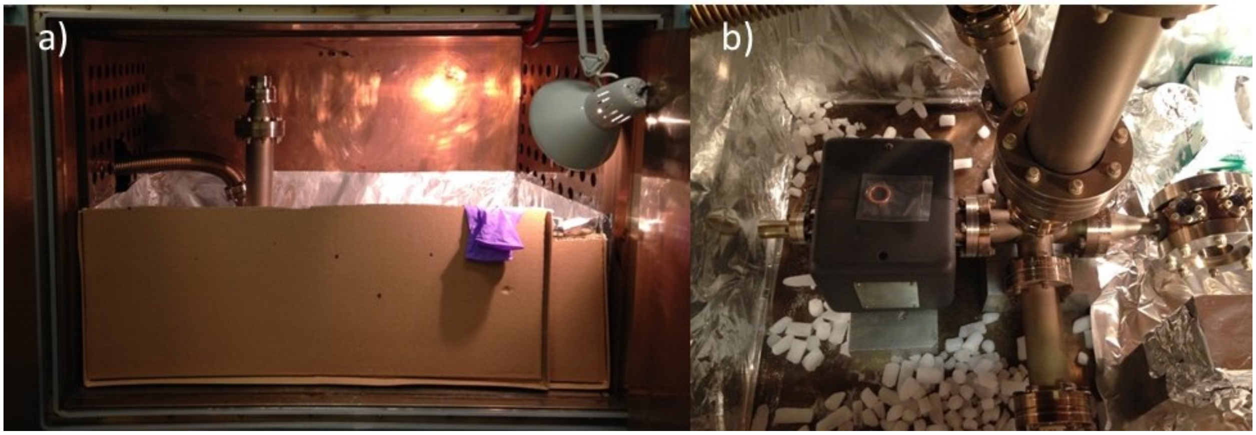

Figure 4.7: a) Bath formed from cardboard and tinfoil constructed inside the bakeout oven. CO_2 is denser than air and forms an inert environment in the working area to prepare the barium source. b) Work area inside the bath, filled with dry ice. Ensure the CO_2 levels reach above the working area.

the system to cool before venting. This accomplishes oven pre-activation.

The next stage is to load the barium into the oven and install it back onto the system. It is essential to do this timely, so that the barium does not have time to completely oxidize before being in vacuum. If the barium is completely oxidized, it will not be an effective oven, since the oxide has a much higher melting point. Therefore, it's good to make sure you have everything you will need ready to go before you begin.

Tools needed are tweezers (fine tipped), knife (use sturdy type that holds a razor blade, since you'll need quite a bit of pressure to cut barium), clean aluminum (or other hard) surface for cutting, and a small drill bit or Alan key that fits inside the tubing. Don't forget the oven feedthrough as well and the barium itself.

The barium oven needs to be loaded in an inert environment to prevent oxidation, such as CO_2 or N_2, or Ar. Any of these methods work, but loading in N_2 (less dense than air) requires sealing off the oven with indium, and later melting it off when activating. I found this to cause issues because the indium often wets into the oven and prevents it from operating. Therefore, I recommend using the CO_2 bath method (or Ar), described below. This method is described in some past theses, however, I feel extra detail is warranted given the amount of difficulties we had. For more information regarding loading in N_2, see Jennifer Lilieholm's dissertation [66].

If loading in CO_2, get 2 Kg (or more) of dry ice. Prepare bath by taping a foil perimeter in the oven and try to have no leaks. An example is shown in Fig 4.7. Pour the dry ice in. Test the CO_2 height by lighting a flame and seeing where it gets extinguished. When you are comfortable this level is high enough, you may begin.

The goal is to put in slivers of barium that are as thick as possible but that can be put in the oven without getting stuck. You want to fill the oven about 1/4 to 1/2 full. Never fill past where the shim stock is spot welded since this area won't get hot and barium above this point may not be properly activated and render the oven useless. First cut off the oxide layer, exposing the shiny, metallic barium as seen in Fig. 4.5. Cut a thick flake of barium. Then slice slivers from the flake, using tweezers to hold the barium in place. Cut off any oxide. Once you are sure the slivers are the right size, put 3-4 of the biggest, shiniest ones in. Make sure they fall down easily. Once all the barium is in gently push down with the drill bit and check the height of barium in the oven.

Pump the system down again. Activate the oven slowly to reduce pressure spikes. Typically, the barium melts in these ovens around 14 A, causing the oxide layer to "blast" off and leave you with metallic barium. When activating, it is important to have the pressure at a level where the mean free path is longer than the distance from the oven to trap or viewports. That is 1 mm for 10^{-3} Torr, 1 cm at 10^{-4} Torr, 10 cm at 10^{-5} Torr, and 1 m 10^{-6}. So you should aim for 10^{-6} Torr or lower. However, local pressures near the oven may be significantly higher and there is no way to be sure of it, so pre-activation is important. We believe that the mean free path issue has been the main cause of oven failures. This mechanism should not actually cause the oven to fail, but makes it difficult to discern whether or not it is functioning correctly.

In a brand-new, clean bakeout system, one may expect to see barium spots appearing when activating (or testing) the oven the first time, as in Fig. 4.8. However, after many years of repeated opening and closing, our bakeout system may not be achieving the same base level pressures, and pumps (especially the large ion pump) may operate at reduced pimping speeds. Since this bakeout system has been used for over 15 years, some pump maintenance and part replacement may be necessary to get the same base pressures, and faster. This does not effect the ultimate

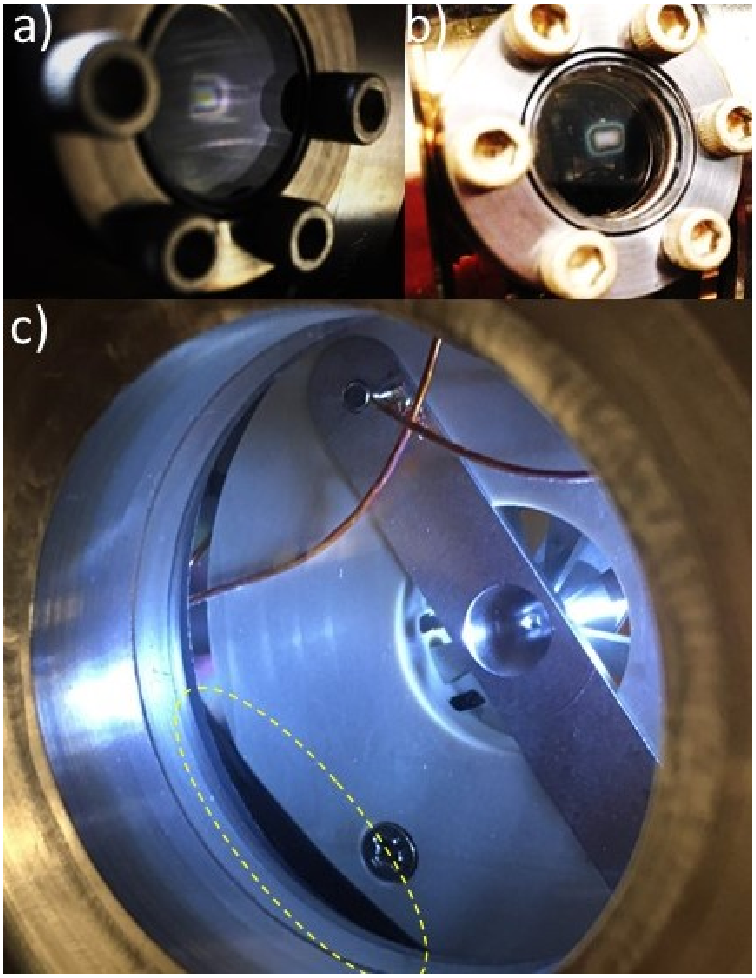

Figure 4.8: Tests for successful oven activation. a) A thin film may appear opposite from the atomic oven or on nearby viewports. a) the rainbow like film is usually first to appear. It is not indicative that the oven has been correctly activated. b) as a confirmation of barium vapor deposition, look for a neutral density appearing at any thin film. c) Thick deposition of barium on the imaging viewport. This is definitely indicative of a functioning oven, yet this amount of film may inhibit imaging optics or laser access of the oven is not well shielded.

pressure of the ion trapping systems once they are fully disconnected from the bakeout system, yet can make the oven tests (Fig. 4.8) appear inconclusive before the bakeout takes place and the background pressure is lower. Therefore, it may be necessary to test the oven for successful operation after bakeout, instead of before. It is a good idea to perform the test before removing the trap system from the bakeout station. Oven testing often also results in the buildup of films on the front viewport, as in Fig. 4.8 (c), where the distance from the oven to the viewport is shorter.

Finally, one should take into account the direction of over spray with respect to ionizing lasers.

Since neutral atoms exiting the oven may be at quite high temperatures, they will be subject to Doppler shifts in ionizing beams. Often different isotopes of the same atom have different transition frequencies, and in many cases, these differences can be bridged by a Doppler shift. This is usually undesirable, so one can mitigate this issue by ensuring the oven makes a 90° angle with respect to ionizing beams. In the 2D trap, we use this strategy.

4.5 Lasers and alignment

Diode lasers are cheap and have become the bread and butter of atomic physics. The accessibility and utility of these lasers has led to great advancements in the field. They can be made to operate with extremely narrow linewidths for precision measurement experiments, and can typically be incorporated in a simple setup that even a motivated undergraduate student can build. The vast majority of the lasers used in our lab are diode lasers.

Early atomic physics experiments necessitated large, expensive laser such as titanium sapphire to access the necessary atomic transitions. The price of these lasers is often in the range of $\$100,000$. In contrast, a typical diode laser setup can be constructed for less than $\$10,000$.

Diode lasers consist of a semiconductor gain medium with an optical bandgap and a small package. Running current across the device terminals causes lasing. These devices are typically developed by the semiconductor industry for a specific application. By circumstance, atomic physicists are now often able to capitalize on convenient laser diode wavelengths to build affordable lasers for their experiments.

A prime example of this is the development of $\sim$ 780 nm laser diodes for CD's, conveniently enabling use for addressing the $5S_{1/2} \leftrightarrow 5P_{3/2}$ transition in rubidium. Before these diode began to become cheap and widespread, Rb was typically addressed with Ti:sapphire lasers but now, Rb is one of the most common species used for atomic physics experiments.

For the trapping of barium ions in this dissertation, four lasers were used. For Doppler cooling, a 493 nm beam is needed, as well as a 650 nm beam for repumping. Before trapping, two lasers

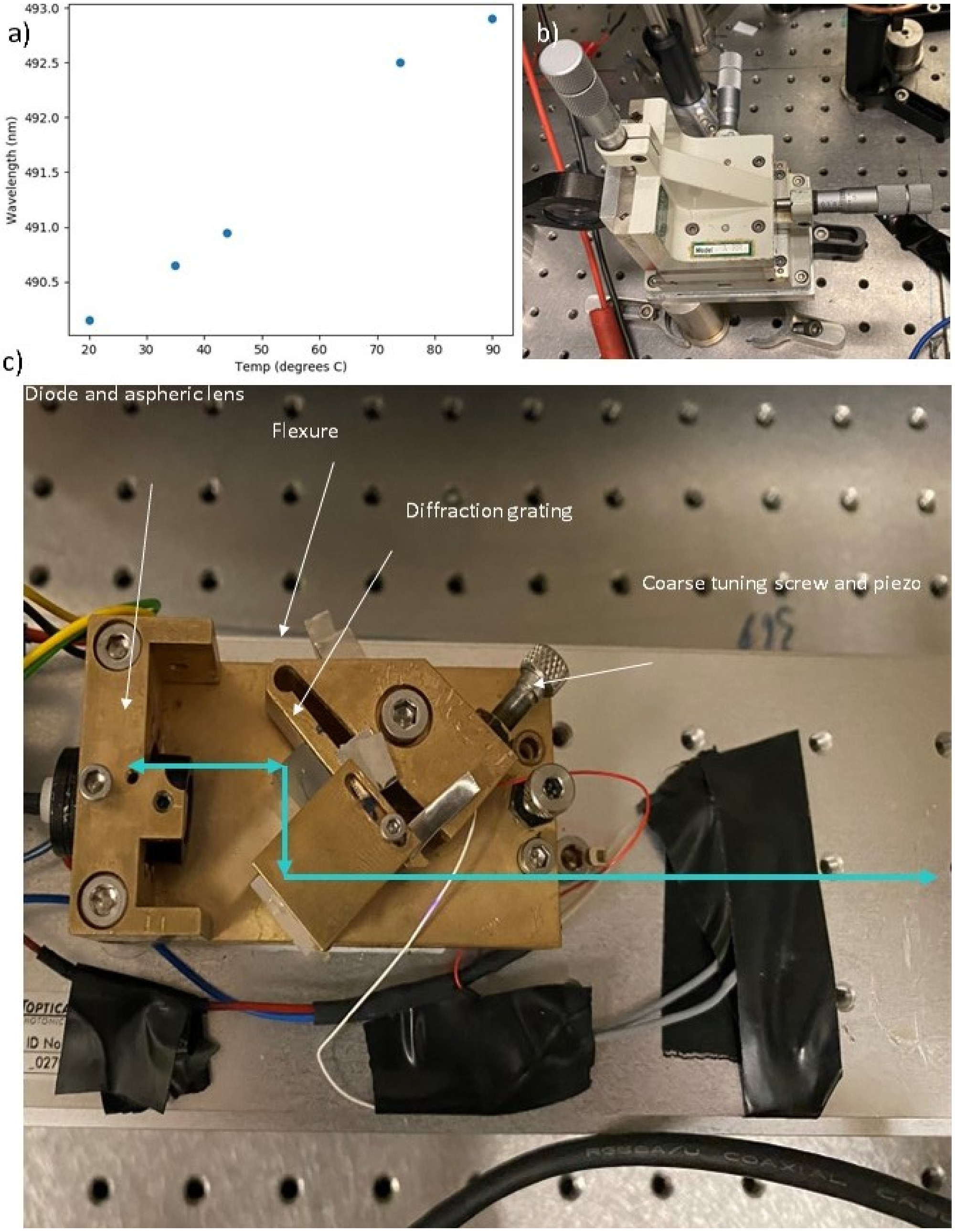

Figure 4.9: a) Plot of wavelength vs. temperature for the a Sharp GH04850B2G laser diode. The central wavelength increases as temperature increases in a roughly linear fashion. The temperature is used as the first stage of tuning to tune the laser to the correct operating wavelength. b) An *xyz* stage for translational alignment as well as adjustment of the focal point of the laser beam, in .001" increments. c) ECDL cavity in the Littrow configuration. The brass flexure mounts allow the cavity to be easily aligned and coarse tuned using a fine-pitched screw. Fine control of the wavelength is achieved by pushing against the flexure with a piezo. The whole brass structure is mounted to a plate with a TEC that regulates the temperature of the diode.

are used to photoionize neutral barium, a diode laser at 791 nm and a pulsed nitrogen laser (SRS NL-100) at 337 nm. Photoionization is not described in detail in this dissertation, but is well documented in past works from our lab [39, 66, 38].

The typical approach is to find a laser diode that is close in wavelength to a desired transition, then build an ECDL to narrow the linewidth and tune the wavelength. Different batches of laser diodes can have different central wavelengths. For example, we use diode prodeced by Sharp (see Fig. 4.9 (a)) diodes to address the $6S_{1/2} \leftrightarrow 6P_{1/2}$ transition in neutral barium as the first step in a two-photon ionization process. Although the range of wavelength operation is quite narrow to be useful for atomic physics, the central wavelength of a laser diode can be adjusted by changing the operating temperature, as well as supplying feedback using a cavity. This direct diode setup is much more simple than the 986 nm frequency doubled setup used previously. Diodes at 986 nm from the medical industry produce light at 493 nm when frequency doubled. An example of the wavelength characteristics of one of these Sharp diodes is shown in Fig. 4.9 (a).

Laser diodes for DVD players were developed near 650 nm, these address the $5D_{3/2} \leftrightarrow 6P_{1/2}$ repump transition. And finally 405 nm laser diodes for Blu-Ray were more recently developed, we have started to use these to address both the 399 nm transition in neutral Yb and the 413 nm transition in neutral barium, both useful in photoionization.

The 493 nm and 650 nm beams are combined in a single-mode optical fiber before being sent to the trap. This ensures a neat, Gaussian profile that focuses predictably. The beams are then focused into the trapping area using a 30 cm lens. For alignment, the lens is mounted on a *xyz* stage (see Fig. 4.9 (b)) with .001" resolution. For initial alignment, the combined beams are purposefully clipped on the side of the trap in each direction. In this way, the coordinates where the beam is clipped are recorded and averaged to find the rough location of the trap center.

The precise wavelength and frequency of laser light is important for addressing atomic transitions, therefore a reference is needed. There are several ways to do this, including atomic references such as vapor cells. Observing fluorescence from a trapped ion is perhaps the best reference to use to tune your laser. However, before trapping, it can be difficult to use an ion as a reference.

We use a High Finesse WS/7 wavelengthmeter to read out the wavelength or frequency of laser light. The wavelengthmeter is read out and controlled via software described in section 4.10.

4.6 AOMs

AOMs are used in most (if not all) atomic physics labs. They serve many purposes. To name a few: shuttering beams, deflecting beams, shifting beam frequencies, and frequency or amplitude modulation of beams. They are essential to the work in chapters 6 and 7, so here a brief description is warranted.

An AOM is a device that diffracts light using sound waves. In a crystal, if the right conditions are met (angle, frequency of sound waves, wavelength), Bragg diffraction occurs. The diffracted orders are shifted in frequency by amounts equal to integer multiples of the sound waves. Typically, one maximizes diffraction into the 1st order to use for experiment, and blocks the other diffracted beams. An example of a beam passing through an AOM is shown in Fig. 4.10.

The first order beam may be shifted in frequency by simply changing the frequency of sound waves (chapter 6), and the diffracted orders can turned on and off quickly, making effective shutters that can be used to create light pulses (chapter 7).

4.7 RF and DC delivery system

High voltage RF used to trap ions is typically delivered by a helical resonator, which served the purpose of transforming a low voltage high current signal to high voltage, low current. It also serves as a narrow band filter, reflecting unwanted frequencies and leaving only a small range of frequencies that make it to the trap. In many cases, one will likely find an unused helical resonator built by a former graduate or undergraduate student, that will easily be incorporated into a new experiment. However, in some cases, a custom design may be needed to achieve the necessary voltages, or frequency range that is needed for a particular experiment. In the following subsections I describe our design. In our case, special care was needed in order to obtain both a

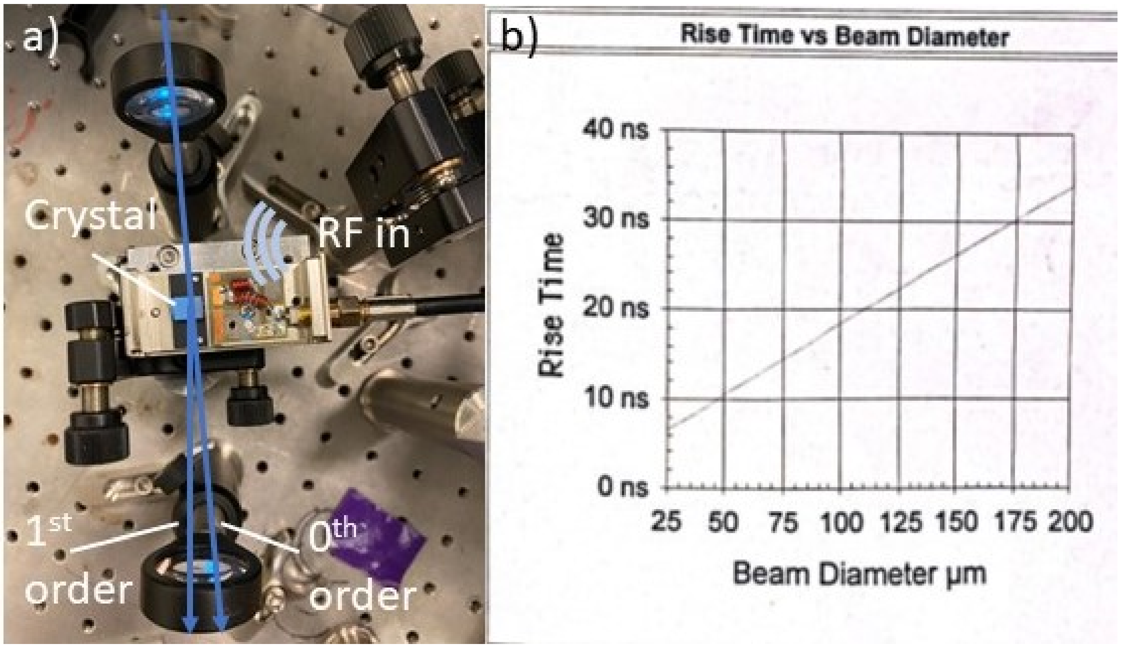

Figure 4.10: a) Laser beam focused through an AOM. RF sound waves in a crystal diffract the light, producing multiple orders separated by the frequency of the sound ($\sim$ 200 MHz). The AOM can be used as a shutter, frequency shifting device, or amplitude modulator, as done throughout this work. b) Typical rise time vs. beam diameter for the AOMs used in this work. The smaller the beam diameter, the faster the rise time. This comes at the expense of diffraction efficiency [67].

relatively low frequency and high operating voltage, requiring a large resonator volume.

A helical resonator is comprised of a shielding canister, containing a primary coil and an antenna coil. RF power is sent into the antenna coil where it is inductively coupled to the primary coil. On resonance, low-voltage, high-current signal is converted to high-voltage, low-current. This high voltage signal drives the trap.

One can calculate the voltages needed for an ion trap based off of simulations (see chapter 5), or by using a formula for simpler trap geometries, such as a linear or hyperbolic trap. Then, it is a good idea to design a resonator that can exceed this voltage by approximately 50%, since typically the actual voltage on the electrodes is somewhat lower than the design voltage. A detailed design guide is given in [68, 69].

The performance of a resonator is often determined by it's quality factor Q, a measure of energy

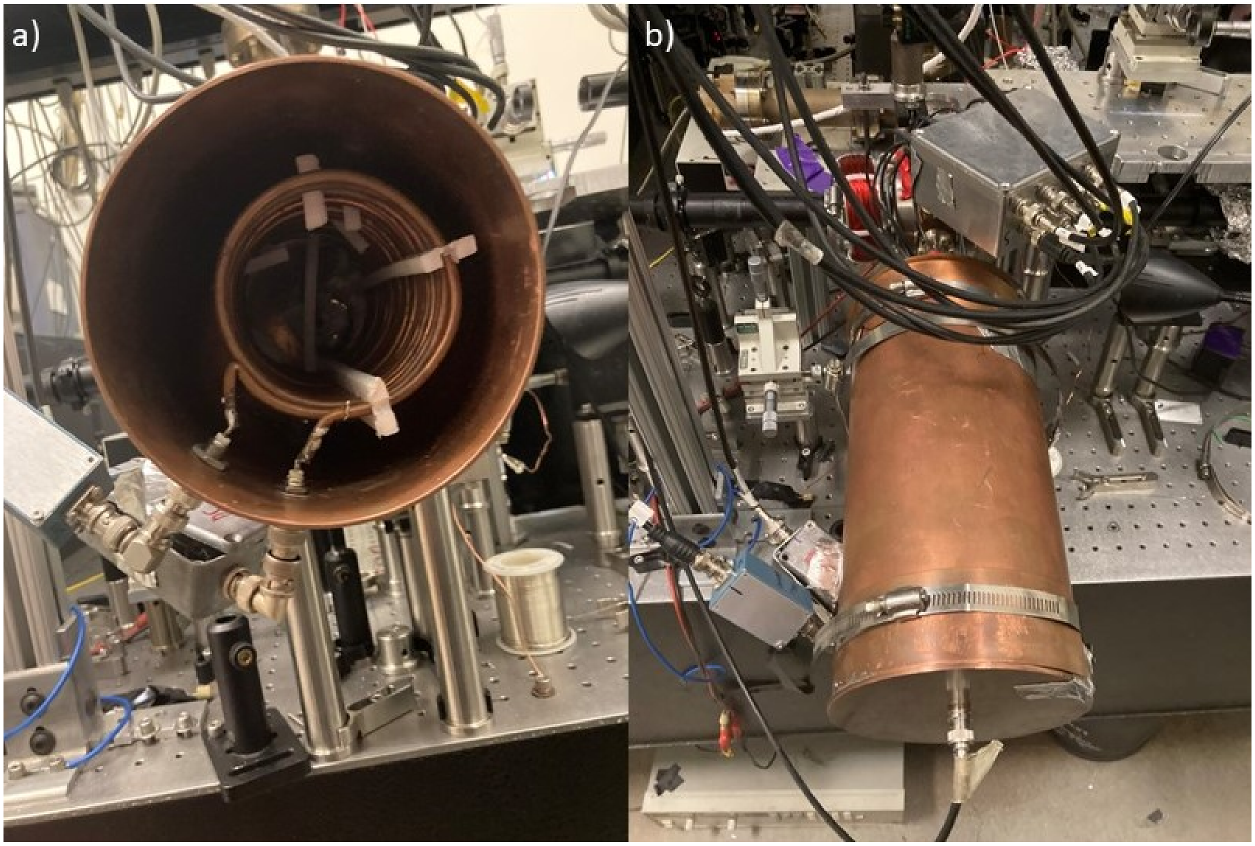

Figure 4.11: a) View of inside of the helical resonator. Two interwound coils generate the RF needed to drive the trap. The coils are kept isolated with the help of Teflon spacers. b) View of the RF resonator attached to the trapping system. A box containing the RF filters is visible just above the resonator.

stored to power lost per cycle. Q can be expressed as

$$Q = \frac{\omega_0}{\Delta_\omega} = \omega_0 \frac{L}{R}, \tag{4.7.1}$$

where ω_0 is the resonant frequency, Δ_ω is the half power bandwidth, L is the total inductance of the resonant system, and R the resistance. Here we should note that when the trap is being driven by the resonator, we have that $\omega_0 = \Omega$. The resonant frequency ω_0 can also be written as

$$\omega_0 = \frac{1}{\sqrt{LC}}, \tag{4.7.2}$$

where C is the capacitance.

The voltage across the trap load delivered by the resonator is given by [68]

$$V_{out} = \kappa\sqrt{PQ}, \tag{4.7.3}$$

where P is the input power and

$$\kappa = \left(\frac{L}{C}\right)^{\frac{1}{4}}. \tag{4.7.4}$$

This equation helps us choose resonator parameters to built a system capable of meeting our experimental needs. Firstly, one should do some calculations as in chapter 2, taking into account the trap geometry through simulations such as those in chapter 5, to estimate a trapping frequency and voltage, before setting out to design a resonator.

Many labs use standard copper pipe (from the plumbing section of the hardware store) and thick gauge conductor from the electrical section. It is often not necessary to spend much time thinking about the theory and design of the resonator, simply winding a coil often results in a resonator that generates a high enough output voltage to trap. However, we tried several resonators of this size on our trap, and did not observe any ions crystallizing, and had difficulties trapping at all. Therefore, we went back to rethink the resonator design.

In our case, we have a heavy element in a relatively large trap, and therefore need a fairly low frequency and high output voltage to achieve the necessary trap depth and frequency. To accomplish this, we seek a high Q while also maintaining a low ω_0. Jumping ahead to chapter 5, we need a voltage of at least ~ 800 V, therefore we should aim about 50% higher for 1200 V at a frequency of ~ 10 MHz. To achieve a higher voltage, one seeks to maximize Q, while maintaining the highest possible κ. Since Q scales with volume, this typically means that a larger resonator with the best possible ratio of L to C will have the highest voltage output. A larger diameter coil with more turns increases L, while having a small winding pitch or having a coil diameter that is too close to the shield diameter increases C. The addition of the ion trap load, including the feedthough to the vacuum system, typically increases C drastically. Finally, one typically minimizes R by using thicker conductors, in order to avoid unnecessary drops in Q.

Based on the project needs and available materials, a resonator was designed with the following parameters: a winding pitch of 1.5 cm, a coil diameter of 9.5 cm, a coil length of 20.3 cm, a shield height of 30.5 cm, an shield OD of 14 cm, and a conductor diameter 0.6 cm (0.25"). The antenna coil is wound from standard copper wire from the lab, approximately 1 mm in diameter.

For our resonator, we use two interwound coils, so that the two endcap electrodes may be DC biased individually. The coils were wound around a thick metal rod of the above diameter, and made from refrigerator tubing. Because of the skin effect, it is not important for the conductor to have a solid core, and more important to have large outer surface area, so refrigerator tubing works well due to easier bending and manipulation than a solid copper conductor of the same thickness. To control the winding pitch, the coils can be stretched or compressed after winding. The coils were wound through Teflon frames with pre-drilled holes to set the final pitch and keep the two coils from touching.

The shield was chosen due to its availability in the physics machine shop materials section. Caps for the shield were formed from circular copper plates and thick copper shim stock. The

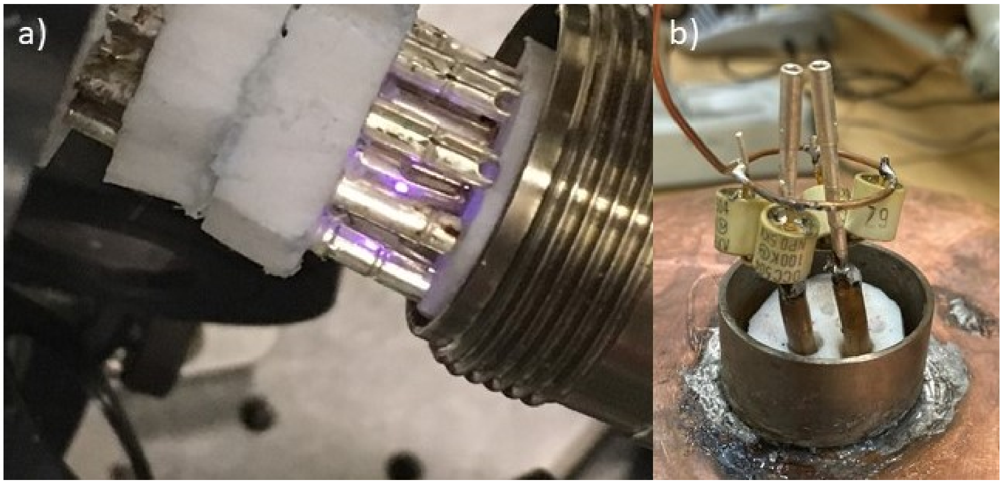

Figure 4.12: a) Arcing between the HV wires leading to the endcap electrodes and ground wires leading to the ring sectors. The ground and HV leads must be kept well isolated, and spacers or receptacles need to be made from low loss material such as Teflon. The wires need to be well shielded so avoid RF interference in nearby lab electronics. b) Adding HV capacitors in parallel lowers the RF frequency.

copper shim stock was bent around the circumference of the plates and soldered with solder and a blow torch. A small gap in the circumferential shim stock was left to allow for a large hose clamp to be installed that serves to lock the caps in place once positioned as desired.

The resonator is interfaced to the ion trapping system through an HV vacuum feedthrough (Solid Sealing FA14259). The coils are terminated with gold plated pins that connect to the feedthrough. The leads are well shielded from the environment using thick copper shim stock. One must take care to avoid the touching of any of the 10 conductors here, as if they get to close, arcing may occur, as seen in Fig. 4.12 (a). Any spacers need to be made of low loss material–Teflon is usually the best option.

One can monitor the resonator performance using a SWR meter, a simple passive device that allows one to monitor forward and reflected power. This allows us to determine two things: that the transmission is maximized when $\omega = \omega_0$ indicating that we are on resonance, and when the RF source is well impedance matched to the load. For maximum transmission of power and highest voltage across the trap, the load impedance looks like that of the source (typically 50 Ohms). This may be accomplished by impedance matching.

The typical procedure is to slowly sweep the frequency of the source, until a small dip in the reflected signal is observed on the SWR meter occurring at $\omega = \omega_0$. Then, keeping the frequency on resonance. To perform impedance matching, one alters the antenna coil by either adding turns, or changing the winding pitch. Additionally, one can control the distance from the antenna coil to the primary coil, dynamically adjusting mutual inductance, and coupling capacitance. Without qualitatively analyzing the impedance matching circuit you have created, one typically is able to achieve $\leq 5\%$ reflected signal when on resonance. Once resonance and matching has been established, the system is ready to be used for trapping.

The resonator was first tested unloaded. We find that $\omega_0 = 20$ MHz and $Q \sim 400$. RF discharge may be observed with enough drive voltage, indicating that the voltage is well above 1 kV. After attaching to the vacuum feedthrough, I find that $\omega_0 = 12.47$ MHz and $Q = 225$. Eventually, the loaded operating voltage is limited by arcing in the vacuum feedthrough, or sometimes outside the

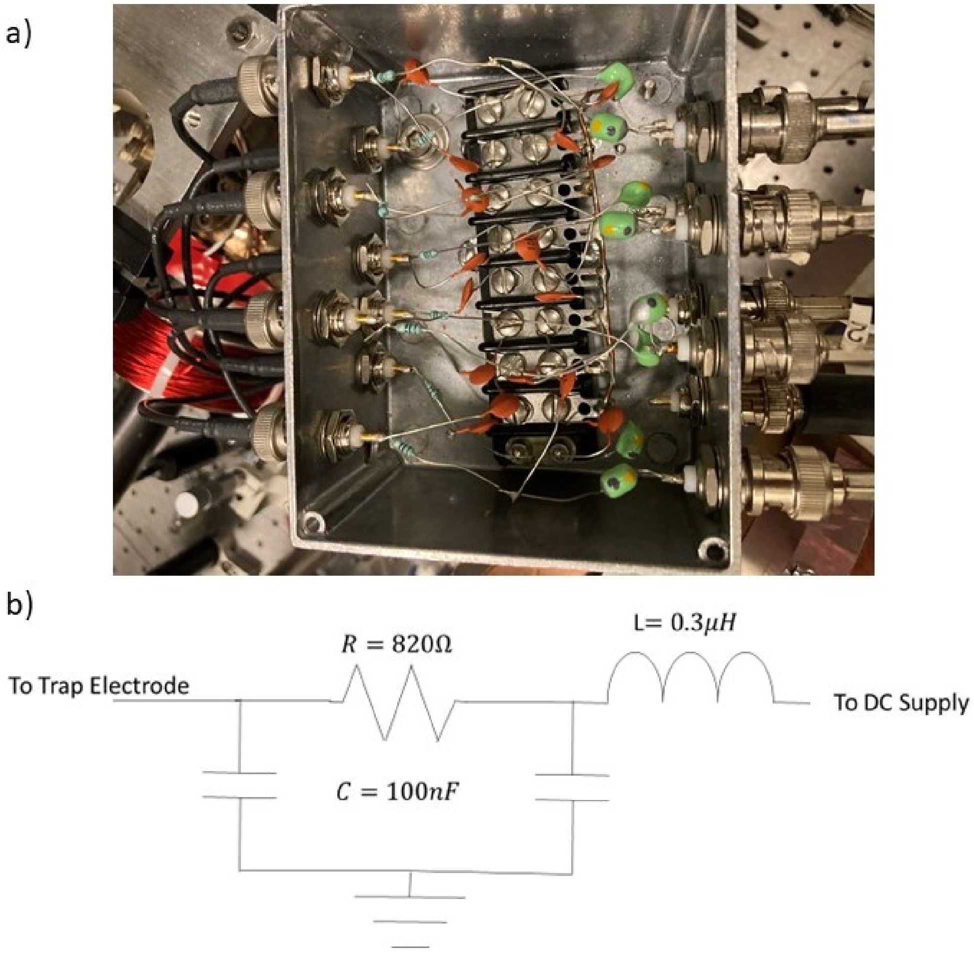

Figure 4.13: Filtering and biasing circuits to allow DC voltages to be applied to the electrodes. a) View into the shielded filtering box. Each electrode has its own filter to prevent RF from travelling to the DC supply and maintain ground potential. b) Schematic of the low-pass filtering circuits.

chamber (Fig. 4.12).

For the experiments in chapter 6, two HV capacitors with 25 pF were installed on each HV line (Fig. 4.12 (b)) to increase RF confinement and reduce radiation effects on laboratory equipment, dropping the resonant frequency to 10.24 MHz and Q to 180. For the experiments in chapter 7, the frequency was further dropped using a total of 4 HV capacitors on each coil, to achieve $\Omega = 8.24$ MHz with $Q = 150$.

In addition to RF voltages, DC voltages are needed to produce the desired trapping potential. Incorporating DC voltages on ion traps must be done with at least some RF filter circuit, to prevent RF pickup from occurring on ground electrodes. RF pickup can greatly alter the trap potential and introduce out of phase components. The filtering circuit is shown in Fig. 4.13. We use a simple low pass filter with a cutoff frequency of ~ 3 MHz. For the endcaps, where RF is delivered, the DC must be introduced at the low voltage ends of the coils.

There are 10 independent DC voltages that are used for tuning the trapping potential as well as compensating for stray fields. The potentials are all controlled from a single HV supply that is adjusted on each channel separately using a 50 kOhm 10-turn potentiometer. Thanks to Gabriel Moureau for building the "box of potentials".

Having a proper ground reference is essential to a well functioning ion trap. It is easy to have insufficient or improperly referenced ground and may lead to many frustrating hours with no results. Typically, the optics table on which the ion trapping system rests is an ideal ground, so solidly grounding both the ion trapping chamber and the RF resonator is important. RF travels through the surface of conductors and avoids the core due to the skin effect, so thick or stranded copper conductors are recommended.

4.8 Imaging

As we learned in chapter 3, ions scatter photons at a rate $\Gamma\rho_{33}$, determined by the parameters of the laser cooling. The scattered photons can then be collected, and imaged onto a device. Imaging is important as its tells us many things about how ions are behaving in the trap. Firstly, the presence of fluorescence tells us that ions in fact have been trapped. The relative brightness can tell us how well we are laser cooling, and also serves as a frequency reference to tune the lasers. Secondly, if the device is position sensitive, it can provide us with images of crystals.

We image the fluorescence from the trap through the endcap electrodes, using either a PMT (Hammamatsu) or EMCCD camera (Andor iXon). Light is collected using a long working distance 0.28 NA Mitutoyu objective, and spatially filtered using a ~ 200 μm pinhole before being refocused and imaged using a 25 mm aspheric doublet. The imaging setup is shown in Fig. 4.14. The magnification of the imaging system can be found using $M = \frac{d_i}{d_o}$, which can be written in terms

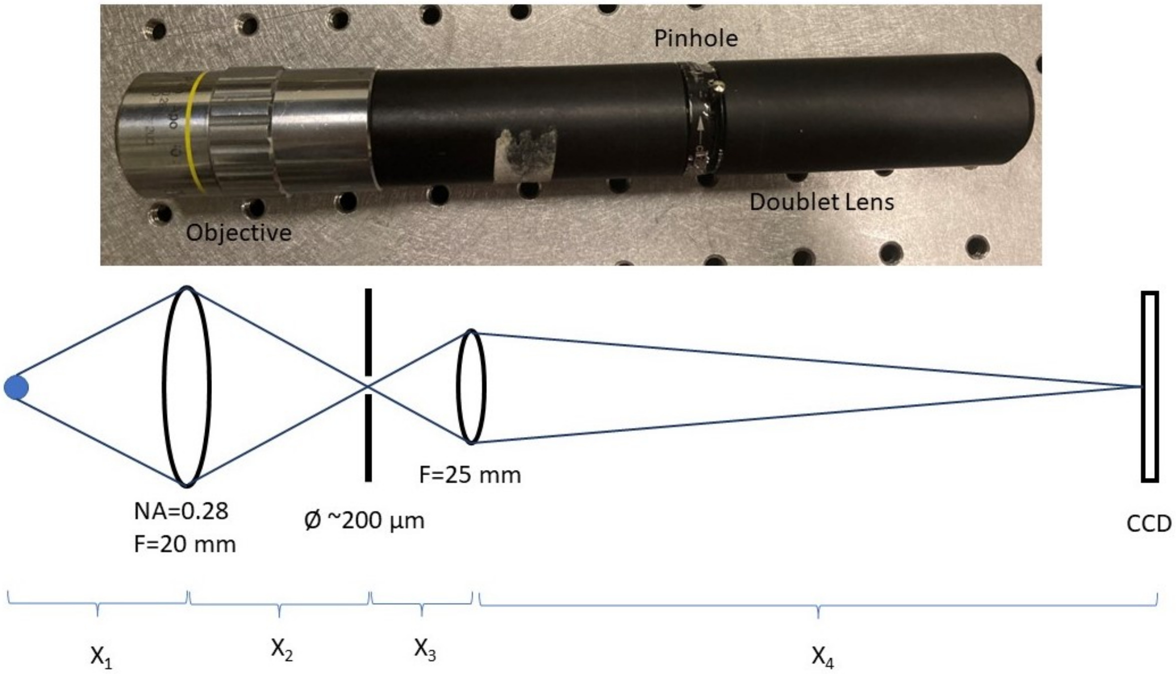

Figure 4.14: Imaging system used to collect fluorescence from the 2D crystals. A long working distance objective collects $\sim 3\%$ of scattered photons. A spatial filter blocks off-axis scatter. The fluorescence is then refocused onto a EMCCD camera or PMT.

of the distances X_i labelled in Fig. 4.14

$$M = M_1 M_2 = \frac{X_2}{X_1}\frac{X_4}{X_3}. \tag{4.8.1}$$

For the images in this chapter, the $M = 78$. In chapters 6 and 7, $M = 98$.

The PMT and camera are both mounted on an aluminum box containing a motorized flip mirror so that ion images may be directed towards either instrument as desired. The box is sealed off with black masking tape to prevent room light from reaching the imaging devices. In front of the box, a 493 nm bandpass filter is installed, blocking stray scatter from room lights and other lasers (337 nm, 791 nm, 650 nm).

4.9 Tpx3 Camera

Much of the research in this dissertation was made possible thanks to our collaborators at Brookhaven National Labs. I owe much to Andrei Nomerotski for continued support with the use of the camera, and Peter Svihra for help with understanding the data structure and processing software. The Tpx3 Cam (Amsterdam Scientific Instruments) is a CMOS device that has the ability to timestamp incoming photons, and was central to the data collection in chapters 6 and 7. Additional applications of the camera in our group's work are presented in [39]. The same camera has been used before for studies of ion crystals [70], single photon counting [71, 72] and quantum optics experiments where simultaneous imaging and time-stamping of multiple single photons is required [73, 74].

The Tpx3 camera is composed of an high QE optical sensor [75] bump bonded [76] to a readout chip, the Timepix3. The chip is 256×256 pixels (each pixel is 55×55 μm). The ions are imaged with the same optics as section 4.7. The image is intensified with an intensifier (Photonis

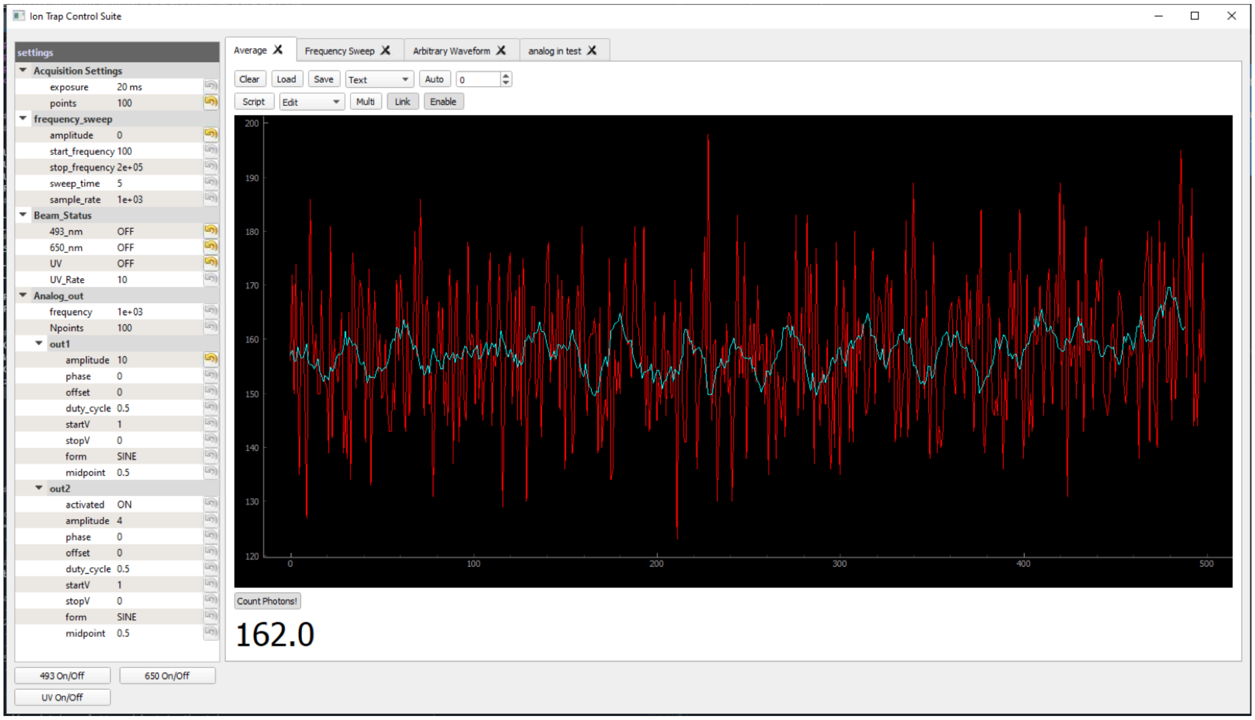

settings
- Acquisition Settings
  - exposure 20 ms
  - points 100
- frequency_sweep
  - amplitude 0
  - start_frequency 100
  - stop_frequency 2e+05
  - sweep_time 5
  - sample_rate 1e+03
- Beam_Status
  - 493_nm OFF
  - 650_nm OFF
  - UV OFF
  - UV_Rate 10
- Analog_out
  - frequency 1e+03
  - Npoints 100
  - out1
    - amplitude 10
    - phase 0
    - offset 0
    - duty_cycle 0.5
    - startV 1
    - stopV 0
    - form SINE
    - midpoint 0.5
  - out2
    - activated ON
    - amplitude 4
    - phase 0
    - offset 0
    - duty_cycle 0.5
    - startV 1
    - stopV 0
    - form SINE
    - midpoint 0.5

162.0

Figure 4.15: Reading the PMT signal through the DAQ card using the GUI installed on the lab computers. The GUI allows the user to easily adjust the PMT exposure and read out data, with the option to save acquired data. In addition, the user can control individual digital outputs that can be used to turn AOMs on and off easily.

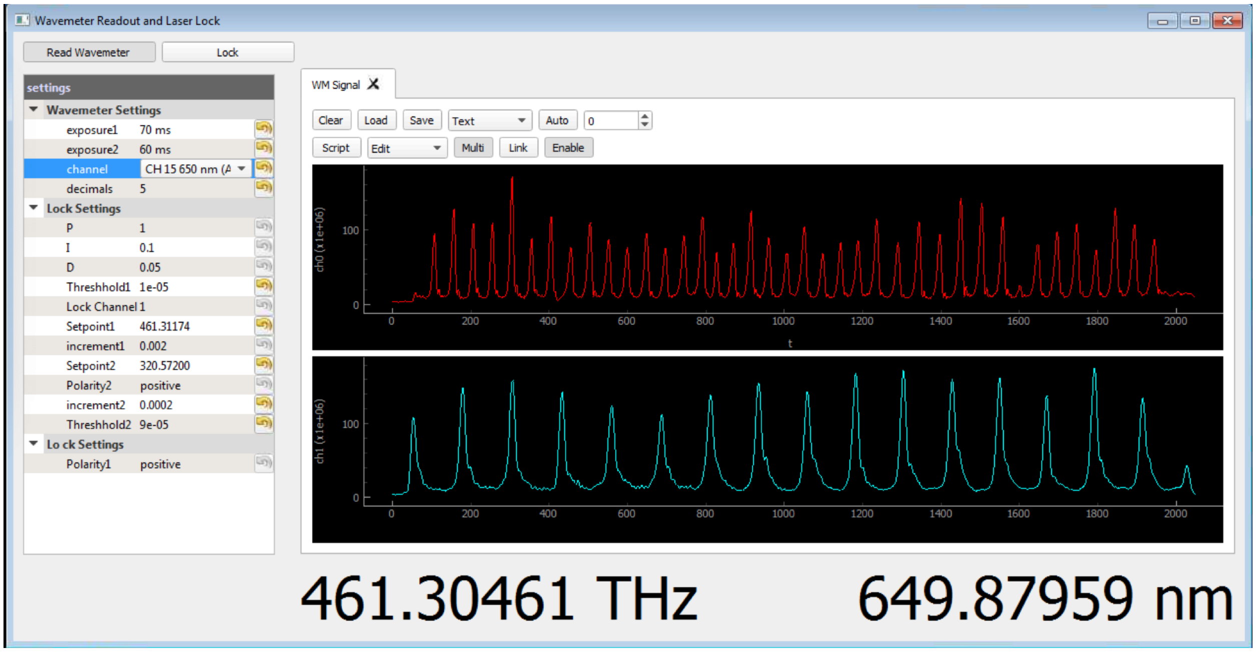

settings

Wavemeter Settings	
exposure1	70 ms
exposure2	60 ms
channel	CH 15 650 nm (A
decimals	5
Lock Settings	
P	1
I	0.1
D	0.05
Threshhold1	1e-05
Lock Channel	1
Setpoint1	461.31174
increment1	0.002
Setpoint2	320.57200
Polarity2	positive
increment2	0.0002
Threshhold2	9e-05
Lo ck Settings	
Polarity1	positive

461.30461 THz 649.87959 nm

Figure 4.16: The wavelengthmeter control software. In addition to reading wavelength and frequency, the user can use this software to change the channel to which laser is being transmitted to the wavelengthmeter, or lock a particular laser to a chosen frequency value.

Cricket$^{\mathrm{TM}}$) with high-QE-green photocathode and captured using the Tpx3 Cam. The intensified camera is single-photon sensitive and provides time-stamping functionality in each pixel with precision of 1.6 ns, allowing for spatial and temporal resolution of images [77, 78]. A TDC with 260 ps time resolution allows us to time-stamp pulses that are synchronized with Ω in order to observe micromotion [79]. ToT is also recorded, and a threshold may be set so that unwanted events are not recorded. Each pixel has dead time of 475 ns+ToT so that multi-hit functionality, independent from other pixels, is possible. The system is read-out using a fast, 80 Mpixel/s bandwidth system called the Speedy PIxel Detector Readout (SPIDR) [80].

4.10 Control system, GUI

Much of the experimental control is done through our Python-based GUI. The GUI is designed to interface with our National Instrument DAQ cards. This initial design of the software is based upon previous students' LabVIEW modules, and makes use of the Spinmob [81] Easy GUI Generator package (thanks Jack Sankey-still using it!), with many add-ons using PyQt5. The software is installed on most of the lab computers, and is available on the lab Google Drive.

The two main modules used for these experiments are the *Wavemeter Readout and Laser Lock* and *Ion Trap Control Suite*. The wavelengthmeter module communicates with the wavelengthmeter to allow the user to read wavelength, change channels through an optical cross connect switch, or use an analog output to feed back to a laser to servo its wavelength. The Ion Trap Control Suite is used to read off data collected from the PMT, to control analog outputs for arbitrary waveform generation to control external instruments such as a frequency synthesizer for frequency sweeps, and for digital logic.

The current pulses from the PMT are collected for a set exposure time, typically around 20 ms. Then, the pulses are stored in a buffer and eventually read out, as shown in Fig. 4.15. The unfiltered signal is inherently random due to the Poissonian nature of photon statistics, and it can be difficult to discern weak signals from noise without some kind of signal filtering. To accomplish this, a moving average is applied to smooth out the signal.

4.11 Trap operation

After initially setting up the full system in the fall of 2018, no ions were trapped for quite some time. Before attempting to trap, almost all of the components described in this chapter needed to be independently verified and improved. Finally, after approximately four months, we started observing a fluorescence signal on the PMT. At first, only weak clouds of fluorescence were observed (Fig. 4.17 (a)), and ions would not crystallize. Eventually, parameters such laser frequency, and compensation voltage were better optimized, leading to crystalline structures. For a few ions, we would see structures such as the one seen in Fig. 4.18 (a). For more ions, the crystals would form rings, such as those seen in Fig. 4.17 (b), and would not fully crystallize.

From here, DC compensation voltages and laser positioning were slowly optimized to move the crystals towards the RF null. An easy way to accomplish this is to turn the RF voltage up and down. As the RF is turned up, the ions are more strongly confined and move towards the center, as observed on the camera. Then, one turns the RF back down, and instead uses DC voltages to move the crystal in the same direction. When turning the RF up no longer moves the crystal, it is near the RF null. Once trapping had been established, the trap was operated as follows.

^{138}Ba^{+} ions are loaded into the trap at a rate of approximately 1 ion/s using two-step resonant photoionization with a 791 nm ECDL and a 337 nm nitrogen laser. We observed 2D crystal geometries that agree with predicted shell structure [52, 61]. For example, in Fig. 4.19, a 28-ion crystal is shown. For the trapping potential used to produce such crystal we measure single ion in-plane secular frequencies of 203 kHz and 221 kHz through application of a tickle voltage (section 4.11) delivered to one of the ring sectors. From Eq. 2.4.1, we infer that the transverse trap frequency is $\sim$600 kHz with the parameters given in Fig. 4.20. Laser-cooled crystal lifetimes of several hours have been observed, with background collisions occasionally (approximately once every 10 minutes) leading to dark ions appearing in the crystal structure or reordering of ions. At maximum, the 2D crystals are not larger than 3 shells, or $\sim$ 30 ions, though larger numbers of ions

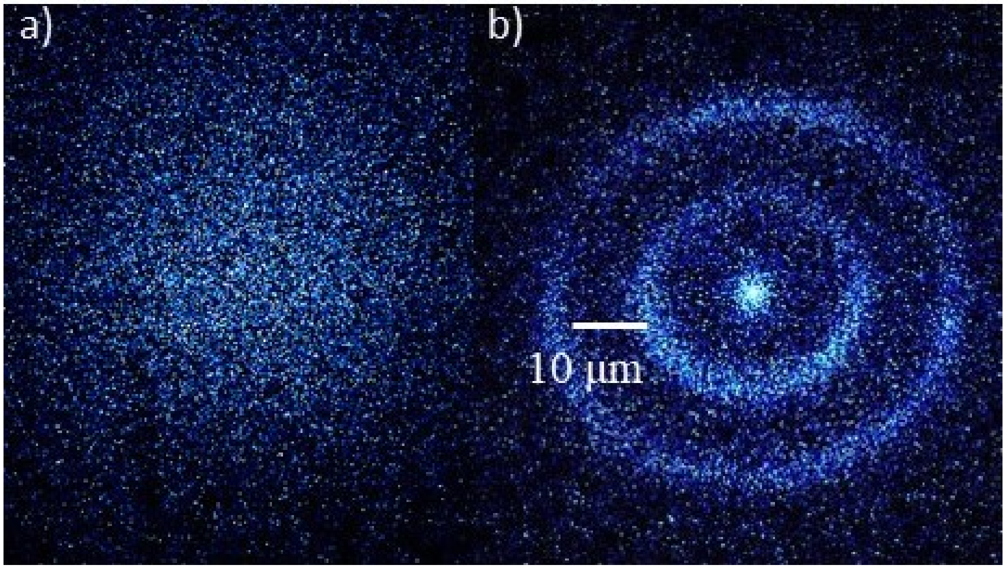

Figure 4.17: Preliminary configurations before crystallization was achieved. a) a large cloud of weakly fluorescing Ba ions. Parameters such as laser detuning and power, stray field compensation, and RF power level can help improve cooling of a cloud in order to encourage ions to crystallize. b) Ion crystal containing 3 shells. The ions are not cold enough to crystallize, so they rotate freely.

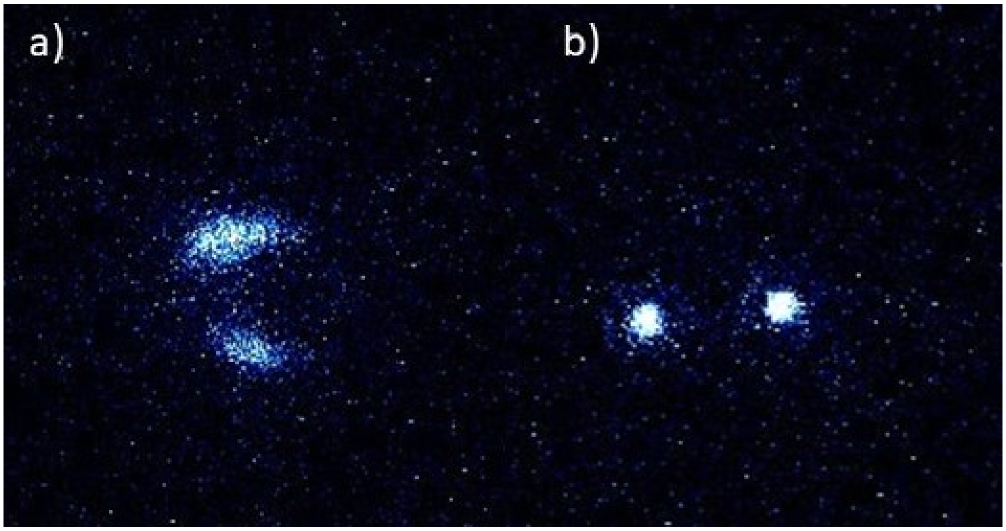

Figure 4.18: 2 ions being displaced around the trap. When close to the center, cooling is improved drastically. Ion spacings are approximately 10 μm. a) Two ions $\sim$ 40 μm from the trap center. b) Two ions near the trap center.

were observed to crystallize in 3D structures.

In Fig. 4.20 we also demonstrate the tunability of our trap aspect ratios. In (a) through (f), we increase the voltage on two opposing segments of the ring by a total of 15 V in steps of 3 V. The shape of the ion crystal changes from a nearly circular in (a) to a linear crystal with in- and out-of-plane zig-zag in (e) and (f). The effect of increasing the endcap bias voltage by 5 V in steps of 2.5 V is shown in Fig. 4.20 (h-j). The ion spacing in the plane of the crystal increases as the endcap voltage (radial confinement) is increased (decreased).

The amplitude of the excess in-plane micromotion is given by $q_r d/2$, where q_r is the radial Matthieu parameter, and d is the distance from the ion to the trap center [82]. Based on the trap voltages, we estimate the scale of the planar micromotion to be 0.051 μm for every 1 μm of displacement from the trap center. In Fig. 4.20 (d), the distance between ions on each end of the crystal is approximately 54 μm. This yields an estimate of a $\sim$2.8 μm of additional excess micromotion between these ions, which is in good agreement with a measured increase in ion image size of about 2.6 μm (1/e^2 brightness) between the ions.

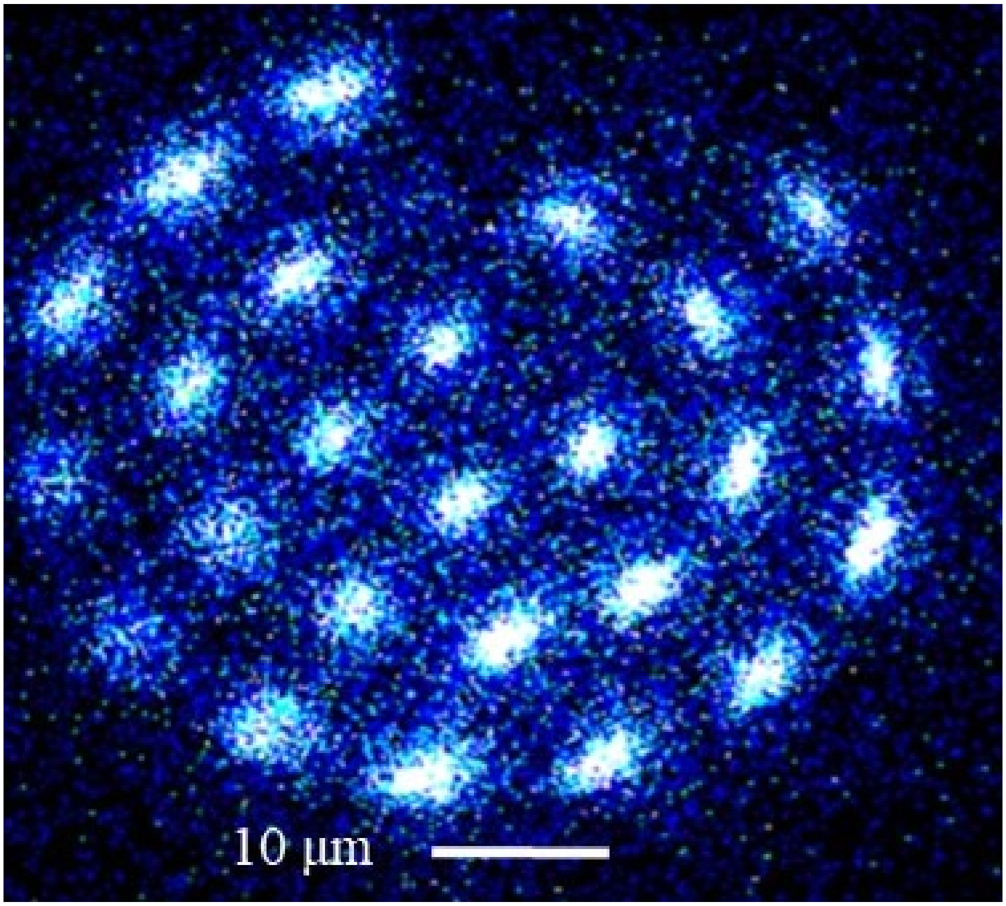

Figure 4.19: 28 ion crystal. Using the experimental parameters in this chapter, we found it was difficult to trap crystals much larger than ~ 30 ions.

4.12 Measuring trap frequencies

Measuring secular frequencies can be done by exciting using a small voltage on the trap electrodes, sometimes referred to as a *tickle voltage*. If the voltage is applied at the trap frequency, an ion will be excited. By sweeping the frequency of the applied voltage, all of the trap frequencies can be measured.

One way to apply the AC voltages is simply to modulate the trap RF. This can be done by using a modulation input on a function generator or synthesizer. When the modulation nears the secular frequency, the ion is excited in the direction of motion corresponding to the motional resonance. For more information on normal modes, see chapter 5. This causes a dip in fluorescence as the ion's motion brings it out of resonance with the laser beam, that can be observed using a PMT as

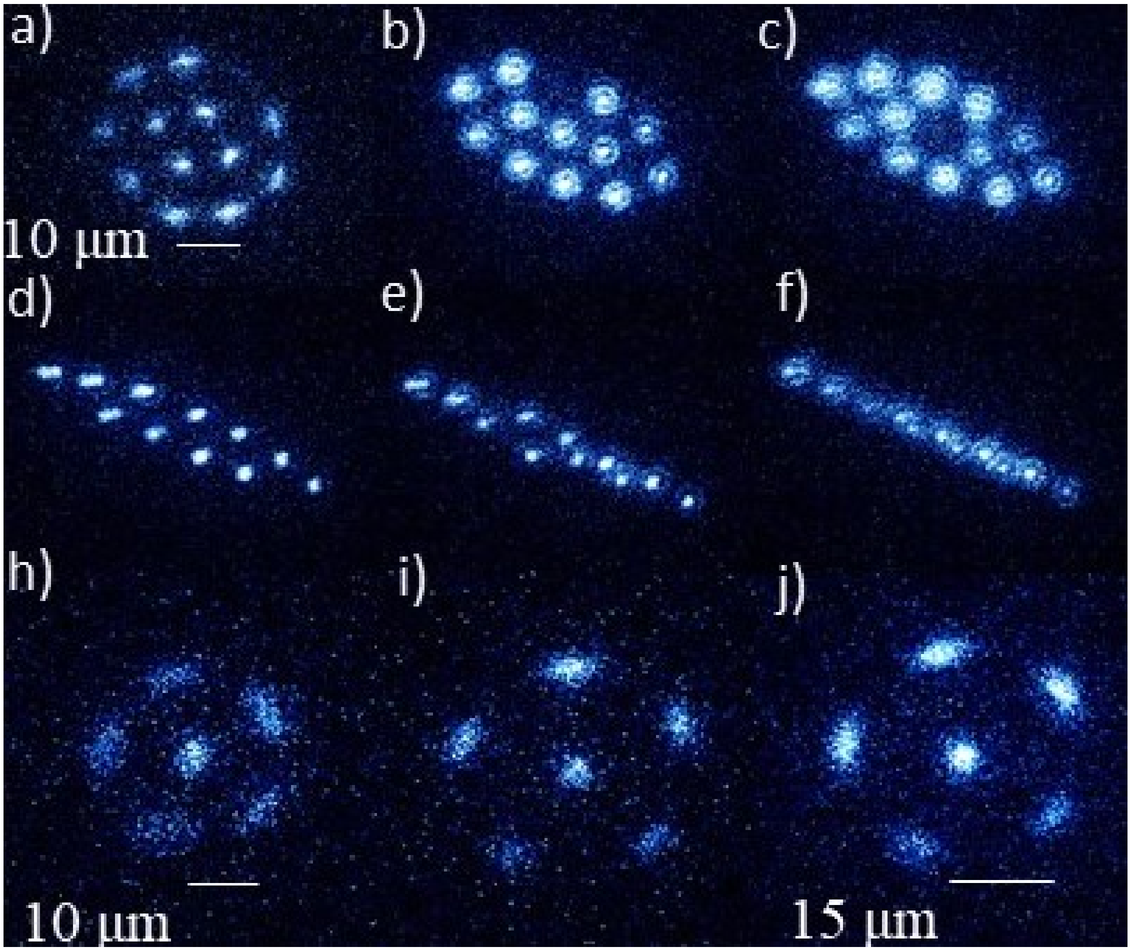

Figure 4.20: Trapped ion crystals produced at different trapping potentials. (a),(b),(h) begin with ∼1000 V of RF at 12.47 MHz. (a) A 29-ion crystal. All ring sector electrodes are at -152 V with endcaps at -145 V and -150 V, a configuration found to compensate stray DC electric fields and allow crystallization near the center of the trap. (b-g) 13 ion crystal with a voltage increase on two opposing sector electrodes, changing the shape of the potential and crystal shape. In (f) and (g) the ions begin to zig-zag out of plane. Two opposing sector electrodes are each increased by 15 V in 3V increments. (h-j) 6 ion crystal with increasing voltage on each endcap electrode by 5V in 2.5V increments. (k) 20 ion crystal with reduced asymmetry. Non-fluorescing ions are other isotopes of barium that are not addressed by the cooling laser. Image scales are consistent in frames (b-g) and in (h-j).

in 4.21 (a). Alternatively, the ion's extent on a CCD image becomes elongated (Fig. 4.21 (b)), and can be easily identified.

The trap frequencies are excited by different amplitudes of tickle voltage, since some are more easily excited than others. Lower frequency normal modes are more easily excited, and normal modes with a component in the direction of cooling laser propagation produce greater fluorescence

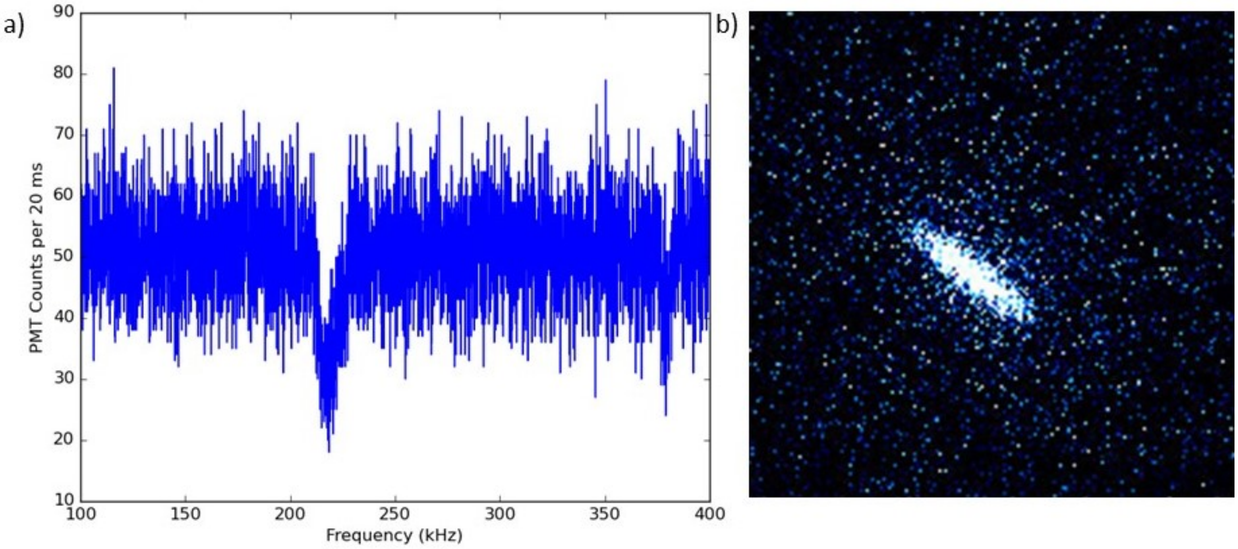

Figure 4.21: Measuring the trap frequency using a tickle voltage. a) Frequency sweep recorded using the data acquisition GUI. A dip in fluorescence appears when the applied voltage reaches a frequency that is equal to a secular frequency. b) Single ion excited by a resonant tickle voltage.

shifts and are more easily observable. Therefore, it is difficult to measure all frequencies with a single sweep. A good practice is to look for radial trap frequencies in the range 180-400 kHz and transverse frequencies in the range 700-900 kHz. The range searched should first be estimated, to make a successful measurement more likely.

Chapter 5

Trap simulations

To understand the dynamics of ions within a trap, it is necessary to have a solid understanding of the forces that drive their motion. These forces arise from the electric field generated by applying potentials to the trap electrodes. If you know the electric fields, it is possible to calculate all of the forces each ion experiences and track their positions and velocities. This information can be used to predict crystal structures and stability, and when combined with actual data take from the ion trap, can be used to extract useful properties such as crystal temperature.

In this chapter I present two separate simulations that when combined, provide a realistic picture of the dynamics of ions in the trap. The first type of simulation is an FDM simulation of the trapping potential that arises due to voltages on the trap electrodes. This simulation tells us what the field structure looks like and gives us a guideline for voltages that promote the formation of 2D crystals.

The second type of simulation is an MD simulation. This simulation builds on the previous simulations, using the electric field from the simulation to calculate a trap force. In addition, each ion feels Coulomb repulsion, and damping (cooling) to remove energy from the system, leading to crystallization. Other forces such as stray fields may be introduced as well. This type of simulation tracks a particle's trajectory is referred to as an MD simulation.

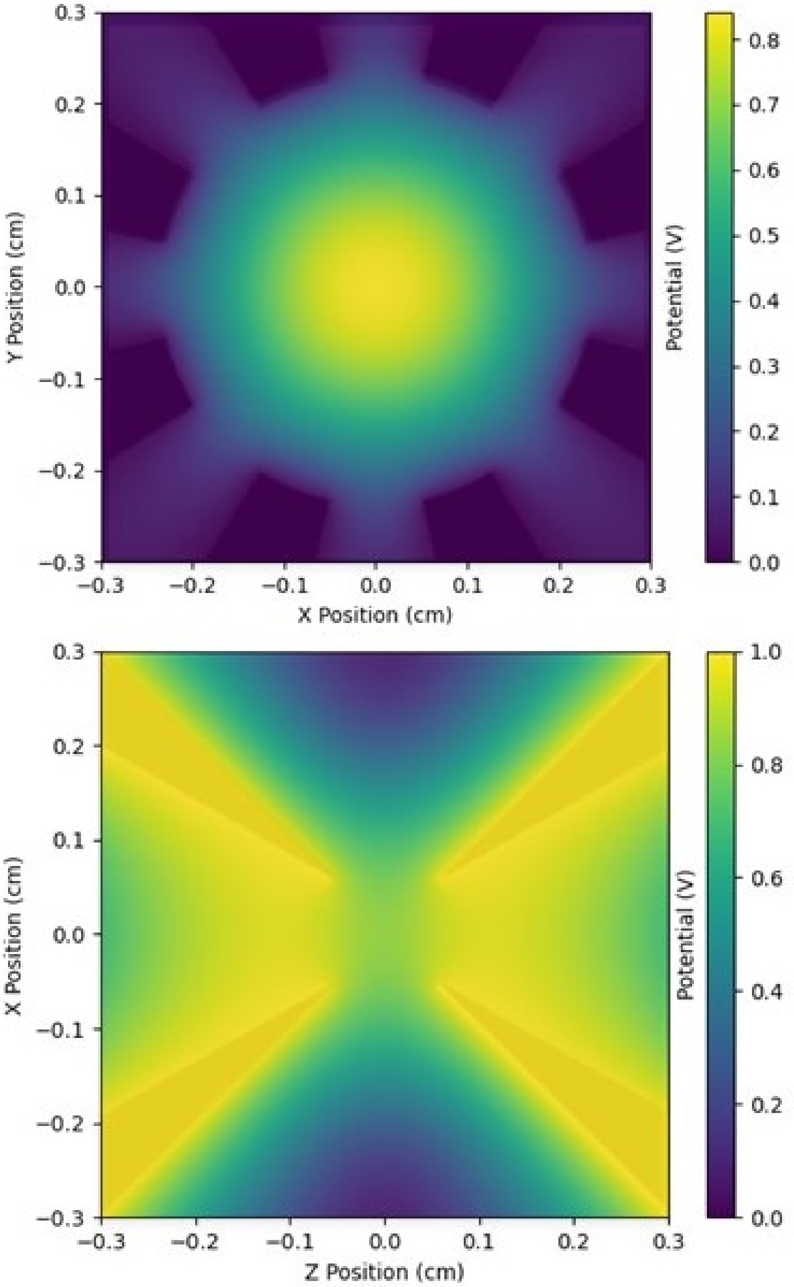

Figure 5.1: Simulated electric potentials for the 2D trap. Each endcap is brought to a potential of 1 V, and the resulting potential everywhere is simulated using the technique described in section 5.1. Top: color plot of the potential in the xy plane for $z = 0$. Bottom: color plot of the potential in the xz plane for $y = 0$. The electrodes are partially shaded to aid the eye.

5.1 FDM simulations of trapping potentials

We first simulate the potential in the trapping area by defining the electrode structure and solving for the potential using the FDM [83]. Near the trap center, a functional form of the potential is obtained from performing a least squares fit of the numerical values [26] to be used in the MD simulations.

Our goal is to numerically solve Laplace's equation for the trap,

$$\nabla^2 V(x,y,z) = 0. \tag{5.1.1}$$

We divide our trap electrodes and trapping area into an equally spaced $N \times N \times N$ grid (we use $N = 400$), where each grid point has length $\delta x = \delta y = \delta z$. Using the symmetric difference approximation, we can then write the second derivative of V as

$$\frac{\partial^2 V(x,y,z)}{\partial x^2} = \frac{V(x+\delta x,y,z) + -2V(x,y,z) + V(x-\delta x,y,z)}{(\delta x)^2}, \tag{5.1.2}$$

with a similar expression for derivatives with respect to y and z. Hence, we can write down the Laplacian. Rearranging terms, we get

$$\begin{aligned} V(x,y,z) = \frac{1}{6}[V(x+\delta x,y,z) + V(x-\delta x,y,z) \\ +V(x,y+\delta y,z) + V(x,y-\delta y,z) + V(x,y,z+\delta z) + V(x,y,z-\delta z)]. \end{aligned} \tag{5.1.3}$$

We can then solve for V by defining the boundary conditions, and iteratively updating the grid until the potential converges to a constant value everywhere.

In order to implement this solution we must first define the electrodes on the grid. To find the trap geometry one should refer to the Solidworks drawings and assembly, where the exact dimensions of all parts can be found. These files, along with the mathematical definition of the trap electrode structure, can be found on the Blinov lab Google drive. The simulations are found in *"fieldfunc.py"* (contains the functions used in the FDM process) and *"field.py"* (the overall simula-

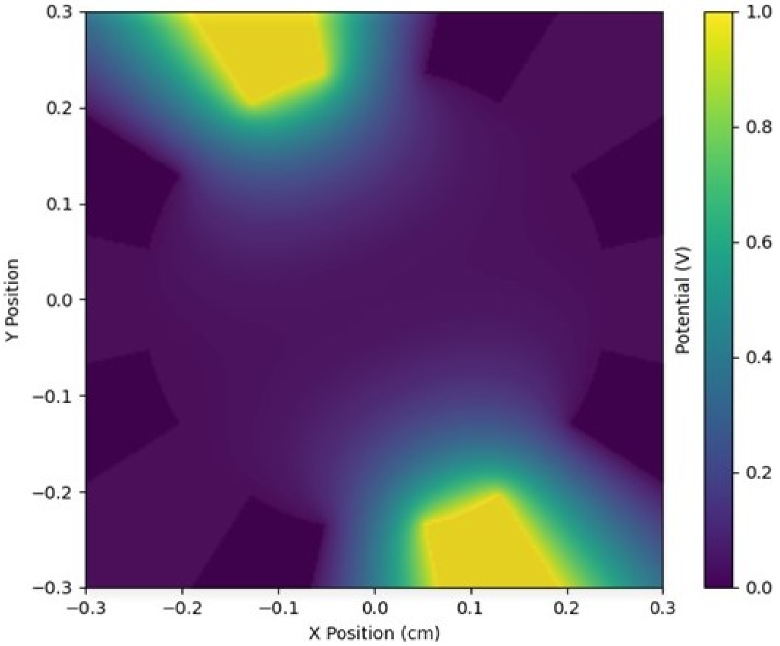

Figure 5.2: Color plot of the simulated electric potentials for the 2D trap in the xy plane for $z = 0$. Two opposing ring sector electrodes are placed at 1 V, and the resulting potential is simulated using the technique described in section 5.1.

tion of the potential).

I find that the solution is most quickly found by beginning with a large step size and using successively smaller spatial steps. To begin, I use steps of $4\delta x$, then $2\delta x$, then $1\delta x$. I find the solution converges well in a reasonable amount of time for 300, 150, and 150 iterations respectively. More iterations, and smaller grid spacings may be used for increased accuracy at the expense of longer computation times. To speed up the computation, we make use of the Numba package in Python, which has been found to allow for substantial speed ups in Python-based programming [84]. The simulated potential for 1 V on each endcap is shown in Fig. 5.1 , and the potential for 1 V on two opposing ring sectors in Fig. 5.2.

Before having the trap parts manufactured, and attempting trapping, it is useful to examine the shape of the pseudopotential as calculated in Eq. 2.1.3. To calculate it, we first need the electric field,

$$\vec{E} = -\vec{\nabla} V. \tag{5.1.4}$$

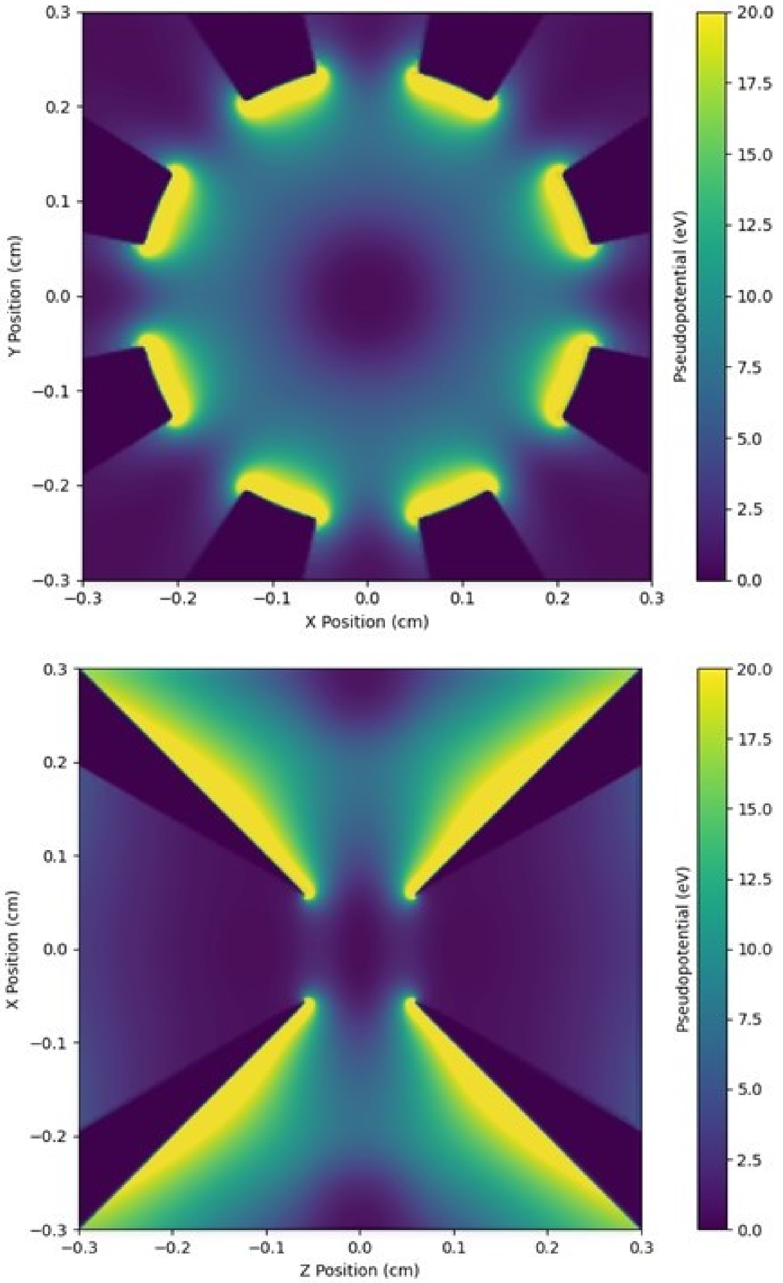

Figure 5.3: Color plot of the simulated pseudopotential for the 2D trap with 1 kV applied to the endcap electrodes. Top: color plot of the xy plane for $z = 0$. Bottom: color plot of the xz plane for $y = 0$. The pseudopotential can be used to calculate the trap depth and trap frequencies.

The pseudopotential Φ is extremely useful because it gives as an approximate, time-averaged potential energy that is felt by a particle of charge q and mass m over an RF cycle at frequency Ω. We can use the information to tell us the trap depth, the trap strength, and the shape of the trapping potential. For $^{138}\text{Ba}^{+}$, with an amplitude of RF voltage of 1000 V applied to the endcaps and $\Omega = 2\pi \times 10$ MHz, Φ is shown in Fig. 5.3.

The trap depth tells us the height of the potential energy barrier to charged particles leaving the trap. This is useful in the design phase when deciding if a trap will have adequate depth to keep ions confined, especially as they are loaded. The neutral atoms originate from an atomic oven, which spews out atoms with a Maxwellian velocity distribution corresponding to the temperature of the oven. These hot atoms are ionized, and depending on the scheme used, may have kinetic energy added if the photons from the ionising beams are more energetic than the ionization threshold. The total average kinetic energy can then be computed and compared against the trap depth in the direction of the atomic beam to estimate the effectiveness of confining the hot ions. Once they are cooled, ions need a much smaller trap depth to remain confined.

For example, consider an oven at 600 °C (realistic for Ba, evidenced by the orange glow of the oven), corresponding to a kinetic energy of approximately 0.1 eV, or 400 m/s. Therefore, having a depth of at least 0.1 eV would be desirable. It is an easy quantity to calculate, and can simply be read off of the pseudopotential plot. For example, in Fig. 5.3 we can see that in the radial direction (xy plane), the trap depth is approximately 10 eV, while in the axial direction, it is approximately 5 eV. Therefore, lack of trap depth should not be an issue for us.

The trap strength refers to the trap secular frequencies ω_i. These tells us the strength of the harmonic confining potential in each direction. The frequency of harmonic motion is related a spring constant $k_i = m\omega_i^2$. The stronger the trap, the stiffer the spring. To find the trap secular frequencies, one fits the pseudopotential near the trap center, using the model described later in this section. The effect of the static potential may be added to evaluate the effect of DC on the trap frequency. Using the simulations in "field.py", one can estimate the trap secular frequency based on applied voltages to the electrodes, and RF amplitude.

Finally, we can look at the overall shape of the pseudopotential, or compare the ratios of trap strengths. If the trap is stronger in one direction than others, the spatial extent of an ion's thermal motion in that direction will be smaller. For a 2D trap, we are looking for a trap shape that is strongly confined in one direction, while more weakly confined in the other two. Essentially, we can use the description from Eq. 2.4.1 to evaluate if 2D crystals will be formed, and if not, what kind of DC voltages we might need to do so.

Although the plots in this chapter are useful for design and initial trapping, a different approach is needed when considering the dynamics of charged particles in the MD simulation. The $400 \times 400 \times 400$ grid would need to be searched through each time to find the corresponding electric field and force that each ion experiences, and this is a vastly inefficient process. Moreover, the granularity of the grid is not as small as the ion spacing ($1\ \text{cm}/400 = 25\ \mu\text{m}$). Therefore it will not give us accurate results.

Instead, a functional form is much more convenient and orders of magnitude faster, and solves the problem of granularity. Moreover, we are not interested in what happens outside of the region near the center of the trap, where the potential is anharmonic. Instead, we concentrate only on the trapping regions where the displacement from the center of the trap is much smaller than the trap size. Here, we can approximate the potential as harmonic. We fit the potential from Fig. 2.1 to a three-dimensional function with form

$$V(x,y,z) = c_1x^2 + c_2y^2 + c_3z^2 + c_4xy + c_5xz + c_6yz + c_7. \tag{5.1.5}$$

The potential is fit at 1 V, but scales linearly with the endcap voltage. In the case of finding the DC potential, we can also use this functional form, but with different coefficients. The coefficients for each desired configuration of applied voltages should be stored in a file that may be opened when running the MD simulation, and can be scaled for arbitrary voltages. An example of the fit along the z-axis of the trap for the parameters of Fig. 5.1 is shown in Fig. 5.4.

One should note that by choosing a functional form, we might be losing information about higher order polynomial contribution to the potential. We justify this by considering the trapping

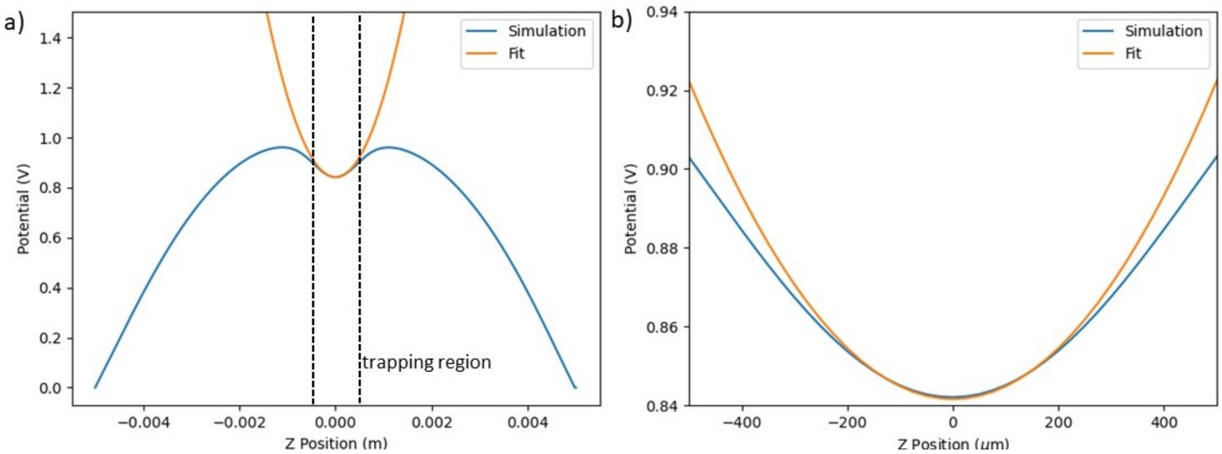

Figure 5.4: Demonstration of the process to find a functional form for the electric potential for parameters in Fig. 5.1. a) Plot of electric potential vs position on the z-axis. b) the potential is approximately harmonic near the trap center, while not elsewhere. The coefficients can be used to estimate the trap frequencies.

area (typically $\sim 100\ \mu$m across), which is very small compared to the actual trap size (electrode-electrode distance is 4 mm in the radial plane). Near the trap center, the potential is approximately harmonic.

If the potentials applied to the electrodes are symmetric (i.e. the same voltage on the endcaps, and the same voltage on opposing ring sector electrodes), we can use the coefficients from the fit of Eq. 5.1.6 to calculate a functional form of the total energy

$$U = \Phi + eV_{DC}, \tag{5.1.6}$$

where V_{DC} is the DC potential. This involves one simulation and fit for Φ, and a separate one for V_{DC}.

The strategy I used experimentally was to use the endcaps to provide additional axial confinement and two opposing ring sectors to adjust the in-plane trapping potential, as described in chapter 4. Therefore, for the MD simulations in this chapter, I only really need to simulate two configurations: 1 V on each endcap, and 1 V on two ring electrodes. All else can be accomplished by simply scaling the coefficients from each fit of Eq. 5.1.6 according to the desired voltage applied.

5.2 Estimating trap frequencies

Estimating the trap frequency based off a chosen configuration of electrode voltage is a useful tool when attempting to create a crystal of desired size and number of ions. For example, to form a 2D crystal, we are looking to achieve the condition from Eq. 2.4.1 of trap secular frequency ratios.

We first consider a trap with no static voltages, and potential determined by Eq. 5.1.6. Then, we calculate

$$|\vec{E}|^2 = |-\vec{\nabla}V|^2 = V_{RF}^2(4c_1x^2 + c_4y^2 + c_5^2z^2 + 4c_1c_4xy + 4c_1c_5xz + 2c_4c_5yz + 4c_2^2y^2 + c_4^2x^2 + c_6^2z^2 + 4c_2c_4xy + 4c_2c_6yz + 2c_4c_6xz + 4c_3^2z^2 + c_5^2x^2 + c_6^2y^2 + 4c_3c_5xz + 4c_3c_6yz + 2c_5c_6xy), \tag{5.2.1}$$

and can easily calculate Φ from Eq. 2.1.3. Equating $\Phi = 1/2m\omega_i^2x_i^2$, we obtain an expression for each trap frequency. For example, we look along the x-axis with $y = z = 0$ to obtain

$$\omega_x = V_{RF}\frac{e}{\sqrt{2}m\Omega}\sqrt{4c_1^2 + c_2^2 + c_5^2}. \tag{5.2.2}$$

Similarly, we get $\omega_z = \frac{eV_{RF}}{\sqrt{2}m\Omega}\sqrt{4c_3^2 + c_6^2 + c_5^2}$. Due to symmetry we get $c_1 = c_2 \rightarrow \omega_y = \omega_x$.

Now, for the case of additional static voltages, we can use a similar strategy. Consider a trap with DC potential V_{ring} applied to two opposing ring sector electrodes, and V_{end} applied to the two endcap electrodes. This is a common configuration when trying to trap 2D crystals. The coefficients from the fit for the two opposing ring electrodes according to Eq. 5.1.6 are given by $c_1'.......c_7'$. Consider a rotated coordinate system so that the two opposing electrodes align with the y-axis. One must first perform a coordinate transformation to the variables $c_1'.......c_7'$.

This time, equating $\Phi + eV_{DC} = 1/2m\omega^2x_i^2$, we obtain

$$\omega_x = \sqrt{\frac{e^2V_{RF}^2(4c_1^2 + c_4^2 + c_5^2)}{2m^2\Omega^2} + \frac{2e(V_{end}c_1 + V_{ring}c_1')}{m}}, \tag{5.2.3}$$

$$\omega_y = \sqrt{\frac{e^2 V_{RF}^2 (4c_1^2 + c_4^2 + c_5^2)}{2m^2\Omega^2} + \frac{2e(V_{end}c_2 + V_{ring}c_2')}{m}}, \tag{5.2.4}$$

and

$$\omega_z = \sqrt{\frac{e^2 V_{RF}^2 (4c_3^2 + c_6^2 + c_5^2)}{2m^2\Omega^2} + \frac{2e(V_{end}c_3 + V_{ring}c_3')}{m}}. \tag{5.2.5}$$

Different trap frequencies for arbitrary combinations of electrode voltages can be calculated in this way, so long as the configuration is symmetric. Keep in mind, the crystals will form along the radial direction that is strongest, so the coordinate system needs to be rotated accordingly before calculating the trap frequencies. The calculation, along with rotations, can be found in *Field.py*.

5.3 MD simulations

A valuable tool for studying the dynamics of ions in a trap are realistic simulations of their trajectories. Building on the functional form for the force due to the trap in the previous section, we can add in the Coulomb potential. Finally, a method of dissipating energy is needed to damp the motion of ions, so that they relax into their equilibrium positions (crystal formation). Additional forces that arise from other trap effects, such as stray fields, can then be added on as desired.

We can describe the force on the ions using Newton's second law:

$$\vec{F}_{net} = \vec{F}_{trap} + \vec{F}_{Coulomb} + \vec{F}_{laser} + \vec{F}_{stray}. \tag{5.3.1}$$

From here we can calculate the equations of motion according to

$$\ddot{\vec{x}} = \dot{\vec{v}} = \frac{\vec{F}_{net}}{m}; \vec{v} = \dot{\vec{x}}. \tag{5.3.2}$$

Given the form of the trap potential from Eq. 5.1.5 we differentiate it to find the electric field and force

$$\vec{F}_{trap} = e\vec{E}_{trap} = -e\vec{\nabla}V(x,y,z) = -e\left[(2c_1x + c_4y + c_5z)\hat{x} + (2c_2y + c_4x + c_6z)\hat{y} + (2c_3z + c_5x + c_6y)\hat{z}\right]. \tag{5.3.3}$$

This can be applied for each voltage configuration and voltage level required. For the RF voltage, we can easily add in the time dependence by multiplying by $\cos(\Omega t)$.

The laser force is implemented via a damping term of the form from Eq. 3.3.3 with damping coefficient γ. This can be calculated as in chapter 3, or set higher to achieve equilibrium results more quickly.

A stray field works to displace ions through a constant electric field $\vec{E}_{stray}$:

$$\vec{F}_{stray} = e\vec{E}_{stray}. \tag{5.3.4}$$

And finally, the Coulomb force has form

$$\vec{F}_{Coulomb} = \frac{e^2}{4\pi\varepsilon_0}\sum_{i\neq j}\frac{\vec{x}_i - \vec{x}_j}{\left\|\vec{x}_i - \vec{x}_j\right\|^3}, \tag{5.3.5}$$

as introduced in Eq. 2.3.1. The Coulomb force is the toughest to implement, since it involves knowing the position of all ions and calculating the displacement vector between each possible combination. Hence, it is the most time consuming and ultimately the limit to the run-time of the MD simulation.

5.4 Implementation

The simulations are written in Python for simplicity, and are based off of several previous studies of trapped ions using MD simulations [85, 54, 86]. Special thanks to all who worked on the simulations over the years: Zeyu Ye, Apurva Goel, and Samip Karki. However, the simulations start to take unreasonably long once many ions are added into the trap. Python is inherently inefficient, so

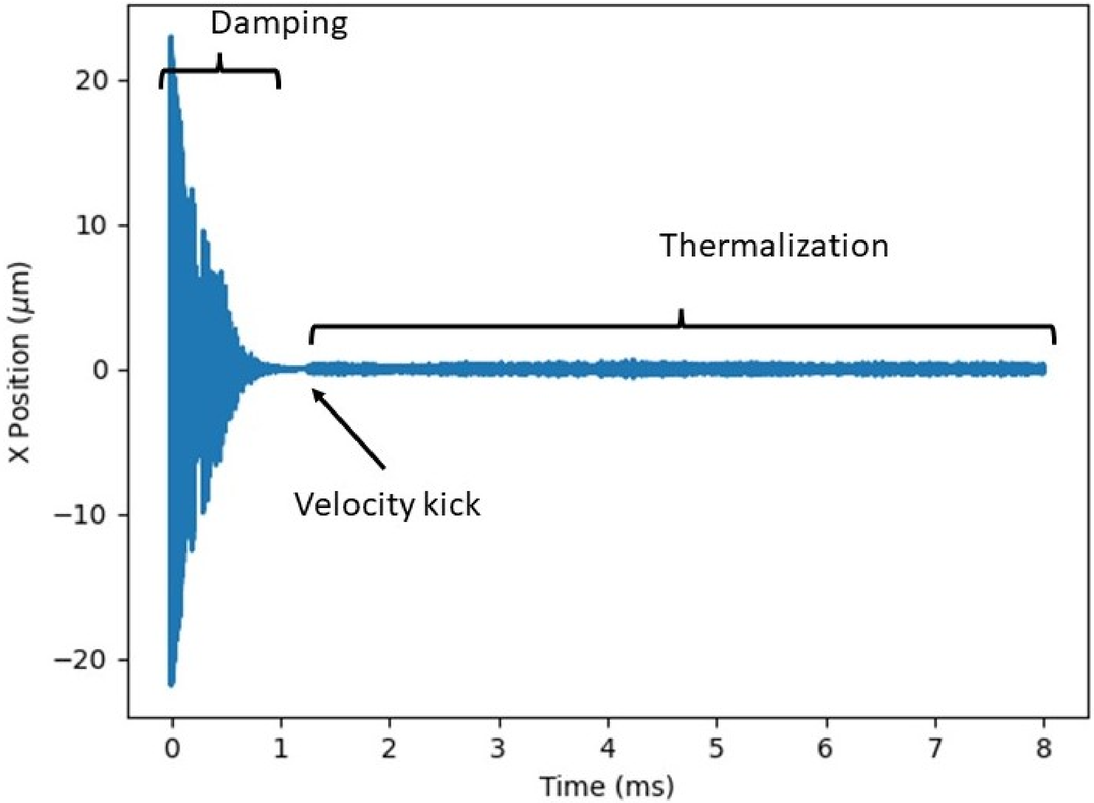

Figure 5.5: Displacement of the x coordinate of an ion as it cools and settles into equilibrium. At $t \simeq 1.2$ ms, the crystal is given a kick and velocities are assigned to each ion at a temperature of 16 mK. The crystal is then allowed to thermalize.

the code should eventually be written in C or another language that is more efficient.

However, the readability is better in Python, which is more conducive to multiple users. We chose to use the previously mentioned package Numba. This led to an order of magnitude decrease in runtime, so that simulations of many ions only takes a few minutes, instead of tens of minutes.

The main high-level simulation is contained in the file *simmain.py*, and the functions that run under the hood are contained in *simfunc.py*. We use the *Velocity Verlet* algorithm, which is simple to implement and relatively fast. Firstly, we are given initial conditions at time t_0, $\vec{x}(t_0)$ and $\vec{v}(t_0)$. Knowing the form of the forces that are felt, we calculate $\ddot{\vec{x}}(t_0)$ through Newton's second law. We then calculate the evolution of $\vec{x}(t+\Delta t)$,

$$\vec{x}(t_0+\Delta t) = \vec{x}(t_0) + \vec{v}(t_0)\Delta t + \frac{1}{2}\ddot{\vec{x}}(t_0)\Delta t^2. \tag{5.4.1}$$

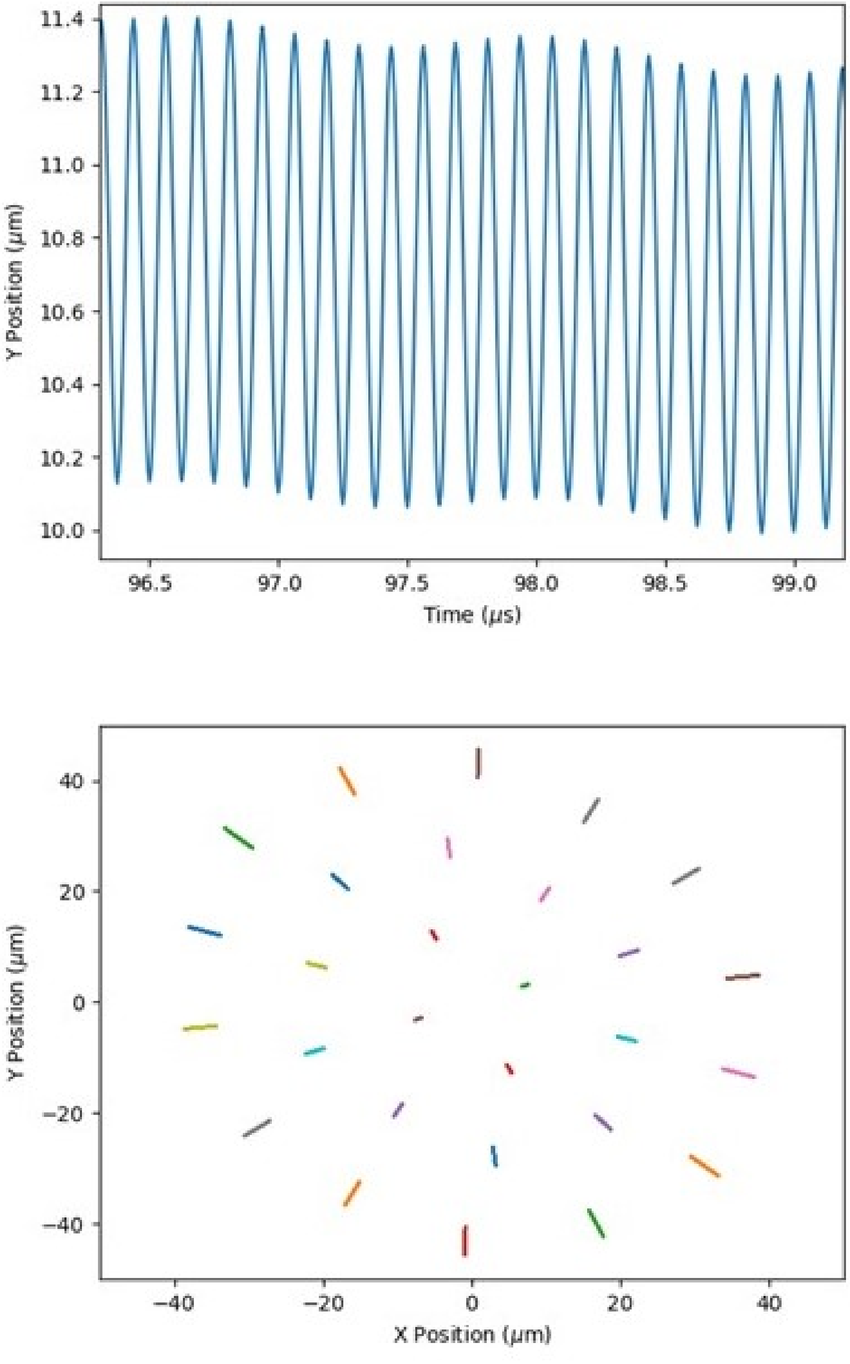

Figure 5.6: Visualization of the trajectories of a 28 ion crystal undergoing micromotion. Top: the *y* position vs time for a single ions within the crystal. The fast oscillations are micromotion while the slow "drift" is the secular motion of the ion. Bottom: the *xy* trajectory for each ion in the crystal, showing the relative amplitude and direction of micromotion for each ion.

Then, we calculate $\vec{\ddot{x}}(t_0+\Delta t)$ and use the result to find the velocity $\vec{v}(t_0+\Delta t)$

$$\vec{v}(t_0+\Delta t) = \vec{v}(t_0) + \frac{\vec{\ddot{x}}(t_0) + \vec{\ddot{x}}(t_0+\Delta t)}{2}\Delta t. \tag{5.4.2}$$

The process is repeated until the desired number of time step have been completed.

One limitation of the Velocity Verlet algorithm is that it only truly represents a conservative system. Since our system is time dependent, and driven by the RF field, this isn't true. To account for this, we make the timestep small compared to the RF period [86, 87].

The data managed using NumPy arrays for easy and fast manipulation, allowing them to be easily vectorized and used with Numba. The simulation trajectories are saves as .npy files (native Numpy file extension) and can be easily loaded using the *np.load()* command. The data arrays are organized as follows. In each data file, four arrays are contained: *"N", "Y", "t"*, and *"accf"*. *"N"* contains the number of ions in the simulation, which is essential if this is not know a priori for data analysis. "*Y*" contains the trajectory information for each ion. The index of this array determines if it is an x, y, or z position or velocity. The Cartesian coordinates of a given ion j are given by $(x,y,z) = (Y[3j], Y[3j+1], Y[3j+2])$ and its velocity by $(v_x, v_y, v_z) = (Y[6j], Y[6j+1], Y[6j+2])$. "t" contains the time for each point in all ions trajectories, and "*accf*" contains the final acceleration for each ion, which is useful if one simulation's trajectories are to be used as the initial conditions for another simulation.

5.5 Cooling, equilibration

We introduce damping into the system in order to allow for ions to become cool enough to crystallize and relax to equilibrium trajectories. This is done in practice using cooling lasers, yet the equilibration time for a large 2D crystal may be 100s of ms. Due to the short timescale of $T = 2\pi/\Omega \simeq 100$ ns, this means about 10^7 time steps would be needed. This would amount to keeping track of $6N \times 10^7$ floats, which leads to prohibitively large data files and RAM consumption on a regular computer.

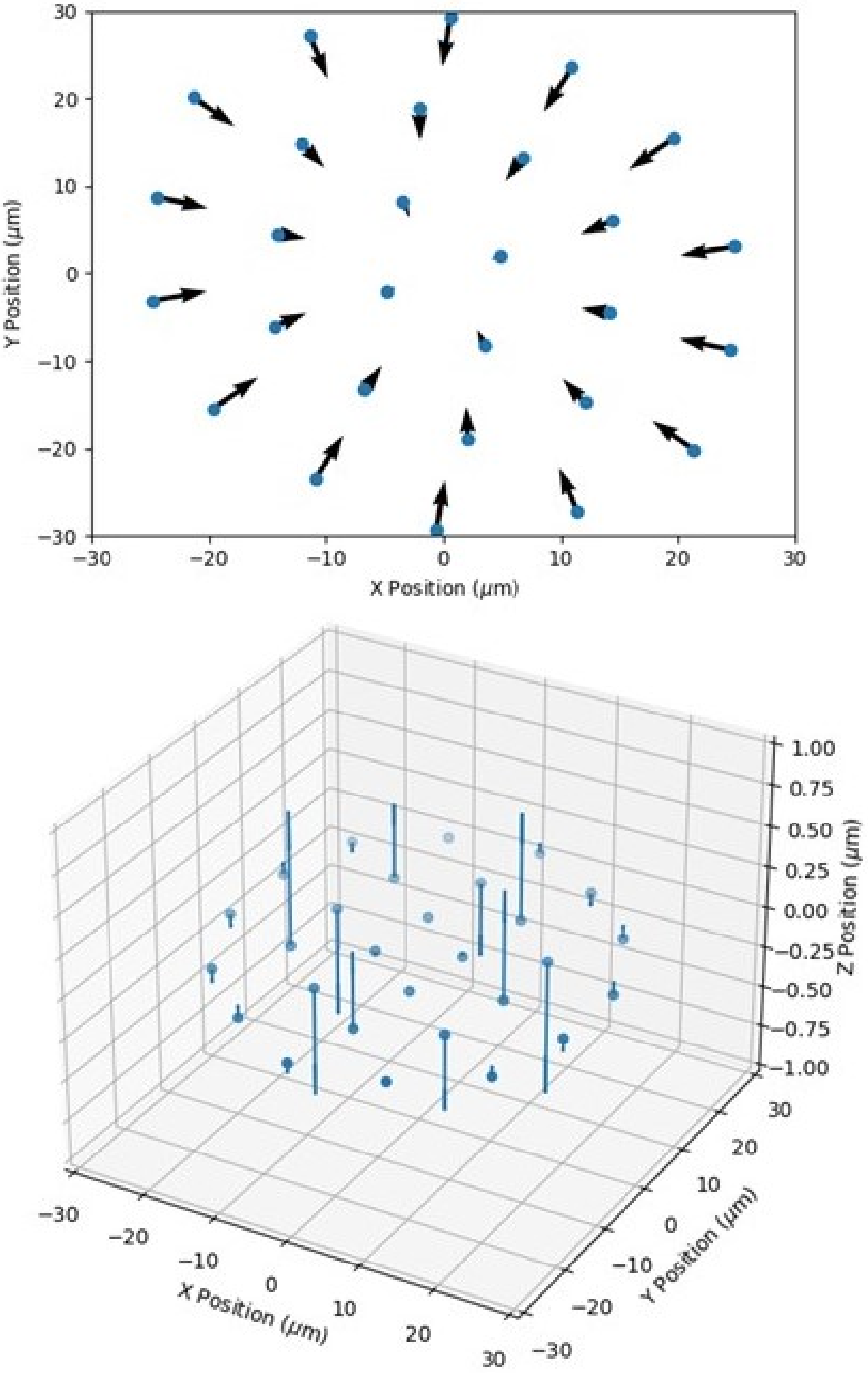

Figure 5.7: Radial and axial normal modes in a 2D crystal. Top: the breathing mode coincides with the driven motion due to the trap RF. Bottom: axial modes are much higher in frequency than radial modes. They are more easily cooled, and have lower heating rates, making them ideal for quantum information applications.

As previously mentioned, to make sure that the time dependent driving force from the trap at frequency Ω does no lead to errors in the simulation, we require that $\Delta t << T$. We choose time steps $\Delta t = T/20$. Ions are given random initial positions within the trapping area, and velocities are sampled from a Boltzmann distribution at an initial temperature of 100 K. Although the neutral barium atoms are initially at a higher temperature when they are ionized in the trapping area, we find that initializing the simulation at these higher temperatures does not yield different results, and thus beginning at a lower temperature saves computation time because the equilibrium configuration can be reached in fewer time steps.

We introduce a rapid cooling that is adiabatically turned off over the course of the simulation [87]. Depending on the trap parameters used, it is convenient to set the damping coefficient to be 1-2 orders of magnitude higher than is physically possible, allowing the equilibrium positions of ions to be found more quickly. This damping is not physical, and will cool the crystal down towards absolute zero. The result is clear micromotion oscillations around an equilibrium position for each ion. The temperature can then later be set (section 5.6) to a more realistic value. An example of this process is shown in Fig. 5.5, and the result of the cooled crystal with micromotion in Fig. 5.6.

5.6 Ion crystallization and small oscillations, melting

If enough energy can be removed from the system due to processes such as laser cooling (chapter 3), the ions eventually reach equilibrium positions. If the ions become localized to a smaller extent than the spacing between neighbouring ions, we refer to the formation as a crystal. To understand the behaviour of ions in a crystal, it is convenient to describe the motion in terms of small oscillations about equilibrium positions, or normal modes of oscillations.

As we learned in chapter 2, ion motion is composed of secular motion and micromotion. Secular motion is harmonic oscillator motion. A single ion is a 3D harmonic oscillator, and N ions are N coupled 3D harmonic oscillators. For each ion, there are three normal modes. The normal

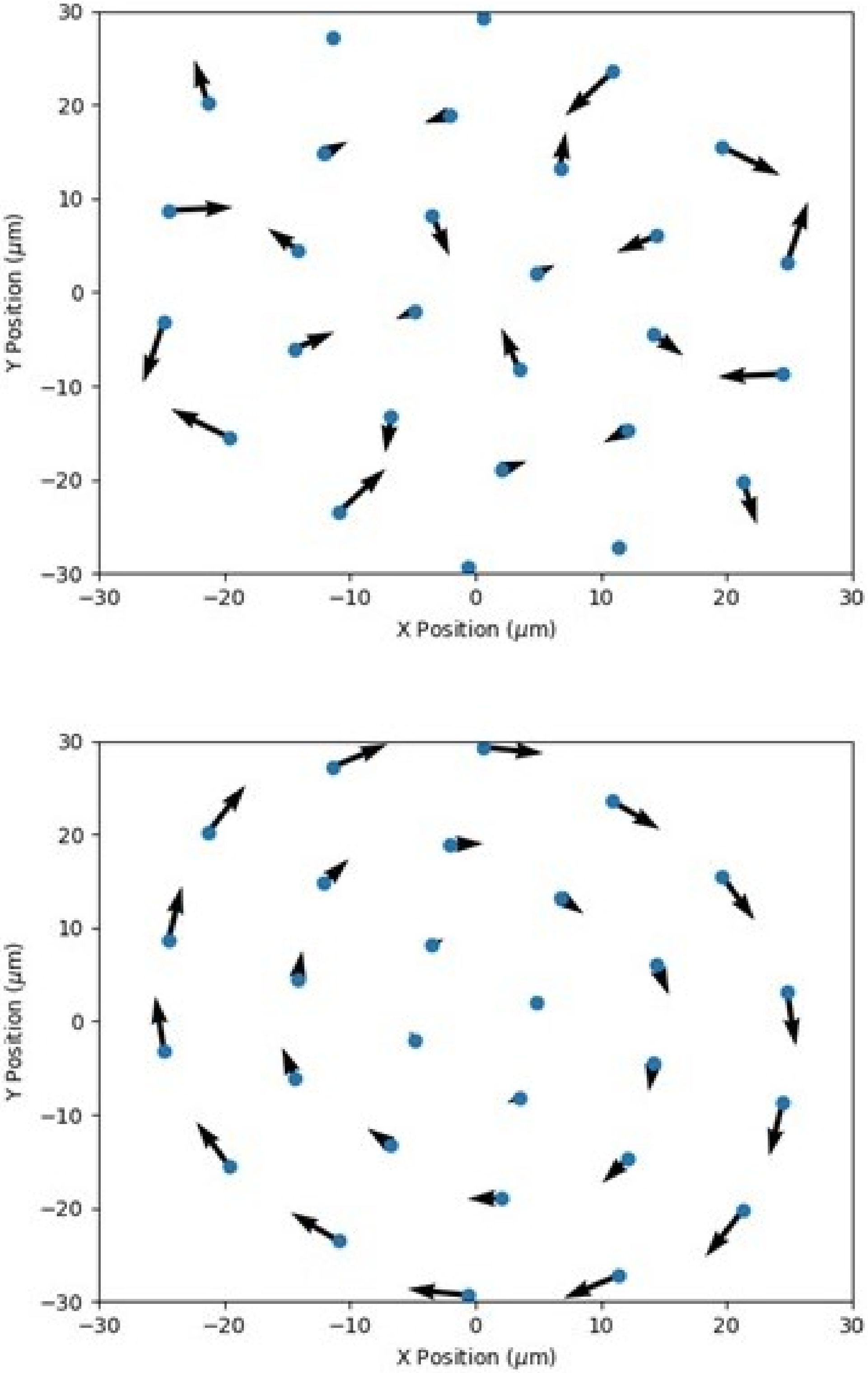

Figure 5.8: Radial normal modes of oscillation of a 28 ion 2D crystal. Top: example of an intrashell mode. Bottom: a rotational mode.

modes can be divided up into two categories according to the symmetry of the trapping potential: radial and axial. The radial modes are weaker and more easily excited, while the axial modes are strong. The strong modes are useful for quantum logic operations due to easier accessibility and lower heating rates, and are the bases of several proposals to use 2D crystals for quantum simulations and computing (see section 1.3). The breathing mode is composed of motion of all ions simultaneously towards and away from the trap center. This mode is continuously driven by the trap RF, and its displacement vector coincides with micromotion. An example of an axial mode and breathing mode can be seen in Fig. 5.7.

To understand the temperature that must be reached for a given crystal to form, one needs to know the ion spacing for ions that participate in the lowest frequency rotational modes. Then the temperature can be estimated by $\frac{1}{2}k_bT = \frac{1}{2}m\omega^2x^2$.

Radial modes include the breathing mode, many modes that include intrashell motion (between shells), and rotational modes (Fig. 5.8). When a crystal is in thermal equilibrium, the temperature of each mode is equal. Weaker modes will be excited to larger displacements. Eventually, the displacement can exceed the spacing between ions, at this point the crystal melts. If the crystal melts due to an intrashell mode, it is referred to as intrashell melting, or radial melting. If it melts by a rotational mode, it is referred to as rotational melting, or orientational melting. Typically, the lowest frequency modes are rotational (Fig. 5.8) in a hyperbolic trap, and orientational melting occurs first, followed by intrashell melting. In fact, many numerical and experimental studies have been conducted to gain insight into the process using dust traps [64, 88, 61]. Using the 2D trap to further understand the onset of melting may be another interesting application.

However, it is a non-trivial problem to calculate the exact frequency of each normal mode. In the pseudopotential approximation, one can calculate normal modes by knowing the equilibrium configuration and expanding $\Phi(x,y,x)$ to quadratic order, and solving the resulting eigenvalue equation. Yet the solutions are much more complicated by micromotion. In this case, one needs to use the periodic crystal solution [89]. A good practical implementation is shown in [87].

This periodic crystal approach involves solving for the periodic motion of each ion in the crystal around it's equilibrium point. Our MD simulations are useful in obtaining equilibrium trajectories to do this, as in Fig. 5.6. The difference from the pseudopotential case is a reduction in frequency of all modes [27]. This can drastically effect predictions of the lowest frequency mode, which incidentally, is the most important for estimating the melting temperature. Instead, I find it more simple to use the velocity kick method (section 5.6) to perform temperature estimations.

5.7 Temperature estimation

Measuring the temperature of an ion crystal in the simulation is difficult, since it requires extracting the kinetic energy of the ions. Because micromotion is significant, the kinetic energy of the ions is typically dominated by these fast oscillations, but the thermal temperature is determined by the secular velocities. Averaging over several periods of micromotion is possible in principal, yet we found this difficult. Instead, we find it more simple to set the temperature of a crystal, and simulate a CCD image to examine the extent of trajectories of ions within the crystal.

Simulating a CCD image of ion crystals is a useful way to compare experimental data with simulations. It is difficult to extract information about the dynamics of the crystal since camera speeds are typically much slower then the timescale of both secular and micro motion. In the past, simulated CCD images have been used extensively to gain understanding about crystal dynamics, such as temperature [54, 86].

After the equilibrium configurations are found, the crystals are given velocity kicks [86]. All ions are assigned a random velocity selected from the Boltzmann distribution at a chosen temperature. Then the crystals thermalize over 10,000 RF periods. Finally, an image is generated by tracking the ions position over an array of pixels that represent the physical pixels the imaging device that was used. This approach is used in chapters 6 and 7. A demonstration is shown in Fig. 5.9 for a 28 ion crystal formed using the same parameters as in chapter 4. The velocity kicks are applied in *userconfig.py* and the CCD images generated in "create_image.py.

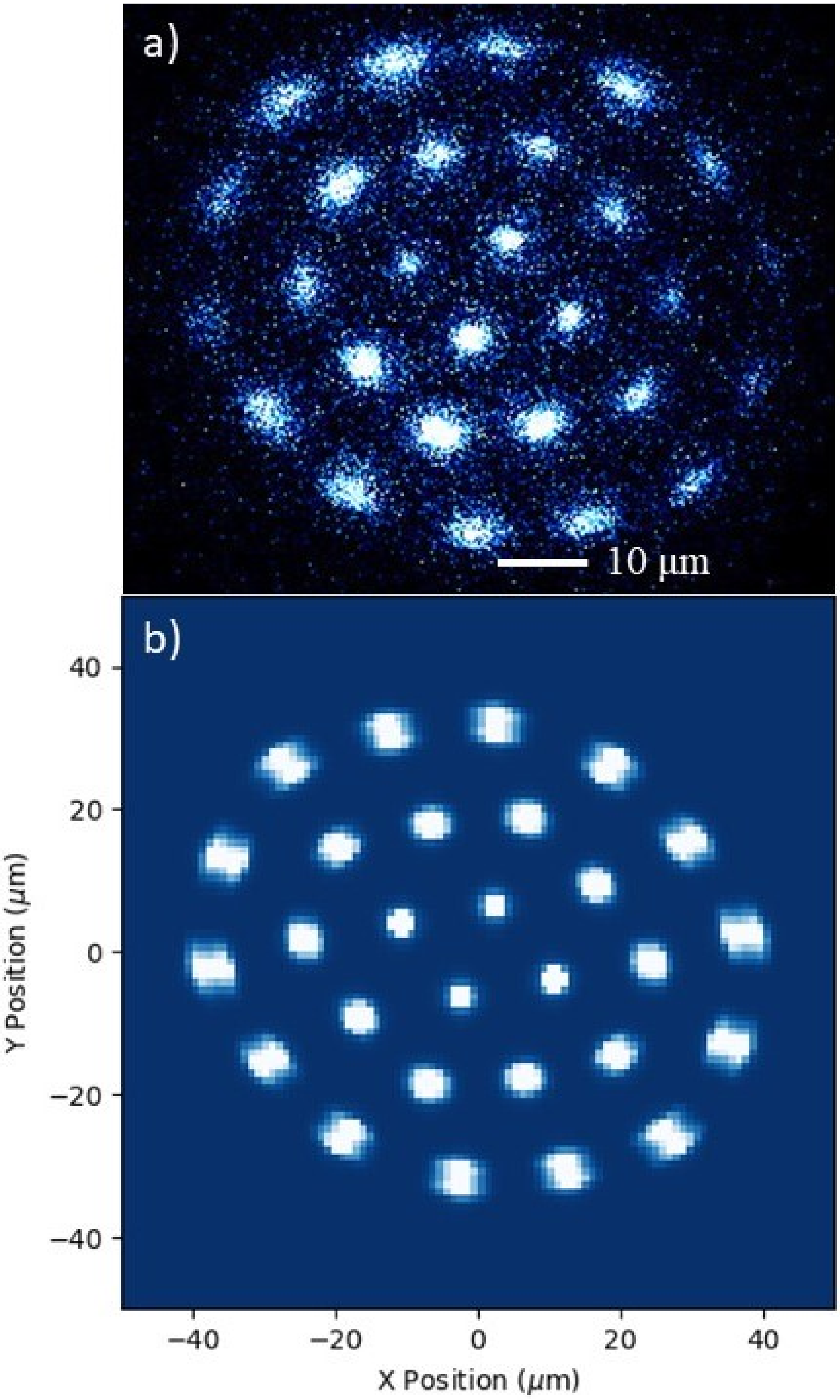

Figure 5.9: a) An EMCCD image of 28 ions in a 2D crystal. b) MD simulation depicting the 28 ion crystal. The temperature is set to 16 mK using the velocity kicks method.

5.8 Going farther

Realizing a simulation that fully represents the dynamics of the ions in the trap is certainly possible, yet computationally expensive. One could use the Velocity Verlet algorithm (or other) to track positions and velocities as done in this chapter, while solving the time-dependent OBEs for each ion. In addition, one would need to keep track of photon absorption and emission events, which occur randomly. Additionally, with real experimental values for damping, a much longer time scale may be necessary, and time steps would need to be small with respect to τ, T. Putting all of this together, one could develop a more realistic simulation that may capture some additional insights into the laser cooling dynamics. Progress towards this goal has begun, but is not yet complete.

Chapter 6

Two-tone cooling

6.1 2D crystals, quantum information, and micromotion

Proposed schemes to use 2D crystals of trapped ions in RF traps for quantum information applications exploit symmetry in the transverse direction, where micromotion can be compensated and minimized for every ion in the crystal [26]. Lasers addressing ions in this direction are not Doppler-shifted in the ion's rest frame, and high fidelity one- and two-qubit operations can theoretically be achieved [17]. However, these operations require that the crystal can be effectively cooled and stabilized.

The presence of large, position-dependent micromotion in the plane of the crystal makes the regular monochromatic Doppler cooling inefficient for large 2D crystals. This concept is illustrated in Fig. 6.1. A 28-ion crystal with individual instantaneous velocities ($\vec{v}$) due to the micromotion are shown in Fig. 6.1 (a), along with the direction of the Doppler-cooling laser. Ions that have small velocity component along the laser k-vector ($\vec{k}$) interact more efficiently with the laser and scatter more photons, which leads to better cooling of those ions. This can be seen in Fig. 6.1 (b), where the ions that scatter the Doppler-cooling light more efficiently appear as brighter spots.

2D crystals in RF traps can be produced in radial [83, 55] or lateral geometries [25, 53]. In the radial geometry, the RF electric field electric field has cylindrical symmetry. 2D crystals can

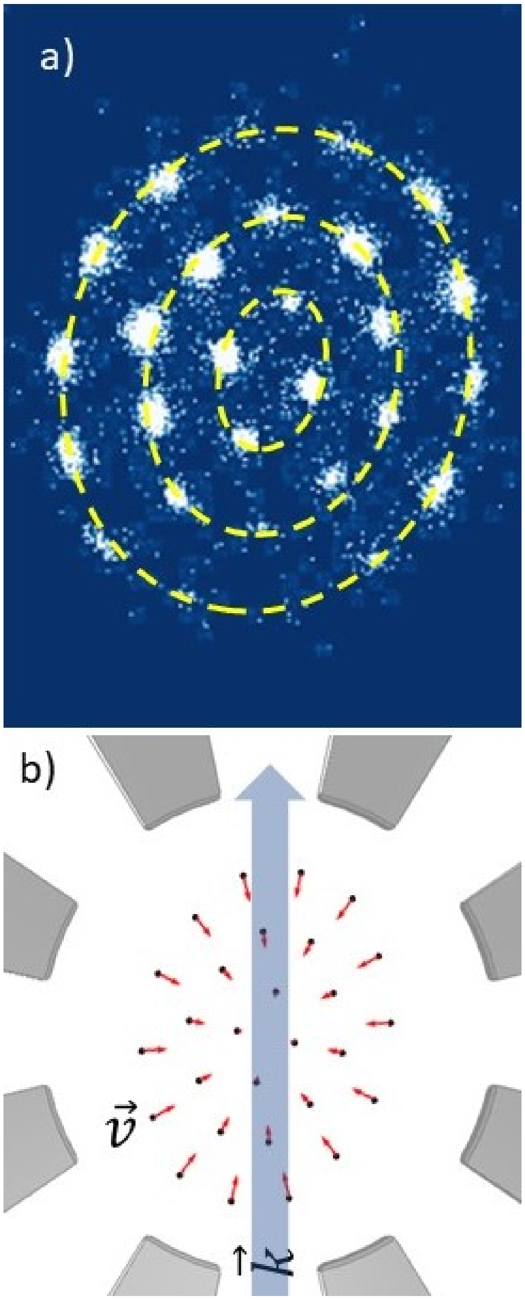

Figure 6.1: Two-dimensional radial ion crystal in a sectored-ring ion trap. a) EMCCD image of the 28 ion crystal depicted in (b). Doppler shifts $\vec{k} \cdot \vec{v}$ lead to uneven fluorescence profile over the ion crystal. Note that the ions in 2D Coulomb crystals form "shells", with three shells indicated in this particular crystal by the dashed yellow (white) lines. b) Schematic of laser cooling of a 28-ion 2D crystal undergoing "breathing" oscillations due to the micromotion. The ions' positions are indicated by the black dots, while the instantaneous micromotion velocity vectors $\vec{v}$ are shown with the arrows. The large transparent light-blue (grey) arrow indicates $\vec{k}$ for the Doppler-cooling laser beam.

be formed in the plane where the transverse electric field has a node, and micromotion in the transverse direction can be minimized for all ions in the crystal. Radial 2D crystals were first explored over 30 years ago for up to 15 ions [90], and more recently up to ~ 30 ions [83, 57]. The planar and transverse normal modes have been shown to be well decoupled, and low heating rates have been demonstrated [55].

Lateral 2D crystals have been studied since the introduction of the linear Paul trap [9], leading to investigations of normal mode structure [91] and demonstrations of sub-Doppler cooling techniques [58]. Recent improvements in microfabricated ion trap capabilities have led to the formation of 2D crystals that can be cooled near the motional ground state [56]. An advantage of lateral 2D crystals is the ability to cool ions along the trap axis where micromotion is largely non-existent, and larger 2D crystals have been reported using this method [92, 59]. Both types of geometries continue to be studied as the potential platforms for scaling up 2D ion crystals for quantum information applications.

To avoid the adverse effects on laser cooling due to micromotion, one can cool largely along an axis where no micromotion is present [25, 92], such as with lateral 2D crystals. However, at least some of the cooling beam's k-vector must point in a direction where micromotion is present, since otherwise thermal motion in all directions is not cooled. As the size of crystals scales up, this effect may become significant. For radial 2D crystals [55, 57, 93], and for 3D crystals, it is generally not possible to isolate a direction in space with no excess micromotion.

As an ion travels back and forth over a period of micromotion, laser light is Doppler-shifted by a different amount at each point in the ion's trajectory. This can be seen as the frequency-modulation of the laser light in the ion rest frame, with a modulation depth proportional to the micromotion amplitude. As the micromotion amplitude is increased, ions may be heated where cooling may be expected, or the laser may be completely off resonance [29, 24]. This is likely the reason that radial 2D crystals so far have been limited to sizes of no more than $\sim$30 ions [57, 54, 83].

In this dissertation, we study radial 2D crystals, where the influence of micromotion on Doppler cooling cannot be neglected. Micromotion causes a time-dependent Doppler shift of cooling lasers in the ion's rest frame. For a 3-level atom such as Ba^+ (Fig. 3.1), this causes the laser detunings Δ_1 (Δ_2) of the 493 nm (650 nm) to vary according to the instantaneous velocity of the ion. Consider an ion oscillating in an RF trap at $\Omega = 2\pi \times 10$ MHz, with amplitude of 1 μm. Then the maximum velocity of the ion is approximately 60 m/s leading to an instantaneous Doppler shift of 125 MHz of the 493 nm beam.

In this chapter, we first discuss the impact of micromotion on the interaction of a single ion with Doppler cooling lasers, extending previous models to include the Λ-system. We use the model to estimate the frequency of a second tone in the Doppler cooling lasers to address ions with differing amounts of micromotion. We then demonstrate the ability to Doppler-cool radial 2D crystals of up to four shells and over 50 ions using this two-tone scheme–an increase of a full shell or approximately 160% increase in ion number. The crystals are analysed, extracting individual micromotion amplitudes for all ions. This information is used to find the trap center, as well as to directly measure the Matthieu parameters q_x and q_y.

6.2 Doppler cooling under micromotion; two-tone cooling

Consider a single ion in an RF Paul trap displaced at a time-averaged equilibrium position r_0 from the center in the crystal plane. Then the equation of motion (Eq. 2.2.15), assuming that micromotion dominates, is

$$r(t) = r_0 \left[1 + \frac{q}{2} \cos(\Omega t) \right], \tag{6.2.1}$$

where q is the Matthieu parameter. The amplitude of excess micromotion is therefore $A = \frac{q r_s}{2}$.

For a true Paul trap with hyperbolic electrodes,

$$q_r = q_z/2 = \frac{8eV}{mR^2\Omega^2} \tag{6.2.2}$$

where e is the elementary charge, V is the amplitude of voltage applied to the RF electrodes, m is the mass of the ion, and R the radius of the hyperbolic ring electrode. Therefore, for a fixed r_0,

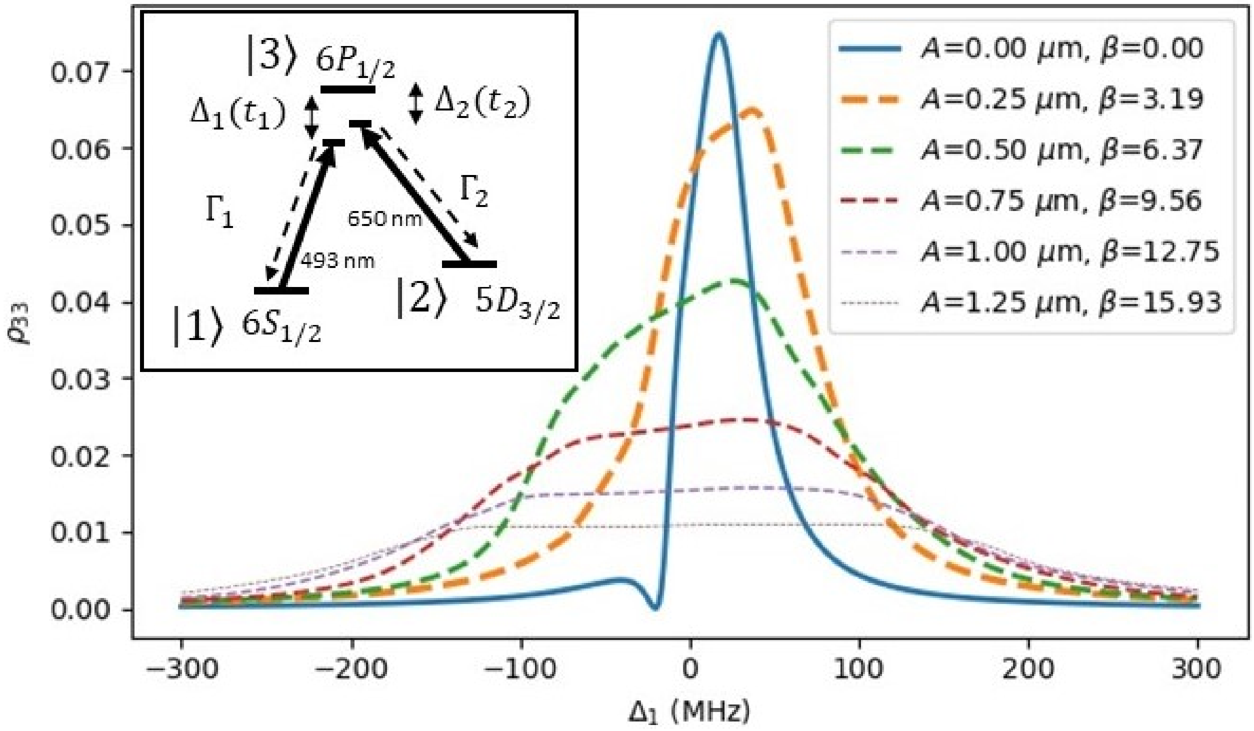

Figure 6.2: Calculated population of the $6P_{1/2}$ state ρ_{33} as a function of detuning Δ_1 of the 493 nm laser from the $6S_{1/2} \leftrightarrow 6P_{1/2}$ transition frequency is plotted for six different micromotion amplitudes A, indicated in the box in the upper-right, along with the corresponding modulation indices β. Δ_2 is set to -20×2π MHz in the lab frame. The scale of the solid line is 1:3, while all of the dashed lines are 1:1.The CPT feature is visible at $\Delta_2 = -20 \times 2\pi$ MHz in the $A = 0.00$ μm curve. For non-zero values of A, the spectrum is distorted by Doppler shifts due to micromotion, obscuring the CPT feature. This CPT feature is shifted by different amounts over a period of micromotion, causing ripple features to occur. The inset in the upper-left shows the relevant energy levels, transition wavelength, decay rates and detunings in ^{138}Ba$^+$.

increasing the trap voltage or decreasing Ω lead to a larger A. One can also adjust A by ion species selection or through a change in the size of the trap.

Since $A \propto r_s$, then for a symmetric crystal A is the same for all ion in each concentric shell. This means there will be two identical regions in each crystal where the projection of micromotion amplitude in the direction of $\vec{k}$ for a particular cooling beam is the same, but with opposite phase. If the crystal is displaced from the origin, the micromotion pattern will no longer be symmetric about the crystal center.

When a laser with wavevector $\vec{k}$ is incident on the ion undergoing micromotion of amplitude A about $\vec{r}_s$, the frequency of laser light is modulated at RF drive frequency Ω. The frequency deviation due to the micromotion-induced Doppler shift is $\vec{k} \cdot \vec{v}$, where the ion velocity $\vec{v} = \dot{\vec{r}}(t)$. Thus, the frequency modulation index is given by

$$\beta = \frac{\vec{k} \cdot \vec{v}_{max}}{\Omega} = \frac{\vec{k} \cdot \vec{r}_s q}{2}, \tag{6.2.3}$$

where $\vec{v}_{max}$ is the is the maximum velocity of the ion due to the micromotion. When the laser beam is parallel to the direction of the ion displacement $\vec{r}_0$, $\beta = kA$.

To understand the influence of micromotion on laser cooling, one can solve the OBEs for the Λ-system and study the behaviour of the excited state population ρ_{33}, as demonstrated in chapter 3. For a single two-level ion undergoing micromotion, an analytic solution exists [29]. However, at higher laser intensities, and in the case of a three-level atom, the solution must be found numerically. For the two-level system, this can be done by finding the steady state solution for each detuning over a period of micromotion, then time averaging the results [29]. We extend this model to study a three-level Λ-system, which is applicable to the cooling of $^{138}\text{Ba}^+$ that we trap and laser-cool. In the three-level case, the numerical approach must be extended to also time-average over each repump laser detuning $\Delta_2(t_2)$ in addition to the main cooling transition detuning $\Delta_1(t_1)$, since there is no guarantee that photons from each beam will be absorbed at the same point in the RF period. Although the spectrum of the laser is different than in the two-level case, we find similar trends.

In Fig. 6.2, the population of the excited state $|3\rangle$ in a three-level Λ-system is plotted as a function of lab frame detuning Δ_1 of the laser from the atomic resonance frequency for different micromotion amplitudes. We consider a single trapped $^{138}\text{Ba}^+$ ion Doppler-cooled on the $6S_{1/2} \leftrightarrow 6P_{1/2}$ transition near 493 nm ($|1\rangle \leftrightarrow |3\rangle$ transition) with a natural linewidth of $\Gamma_{31} = 2\pi \times 15$ MHz and repump transition $5D_{3/2} \leftrightarrow 6P_{1/2}$ near 650 nm ($|2\rangle \leftrightarrow |3\rangle$ transition) with a natural linewidth of $\Gamma_{32} = 2\pi \times 5$ MHz undergoing micromotion at $\Omega = 2\pi \times 10$ MHz, and a saturation parameter for both lasers of $s = 10$, similar to our experimental parameters. To avoid the effects of CPT that can reduce cooling efficiency or cause ions to go into a dark state, the 650 nm laser is typically red-detuned by 10s of MHz. We numerically calculate the steady-state population ρ_{33} as a function

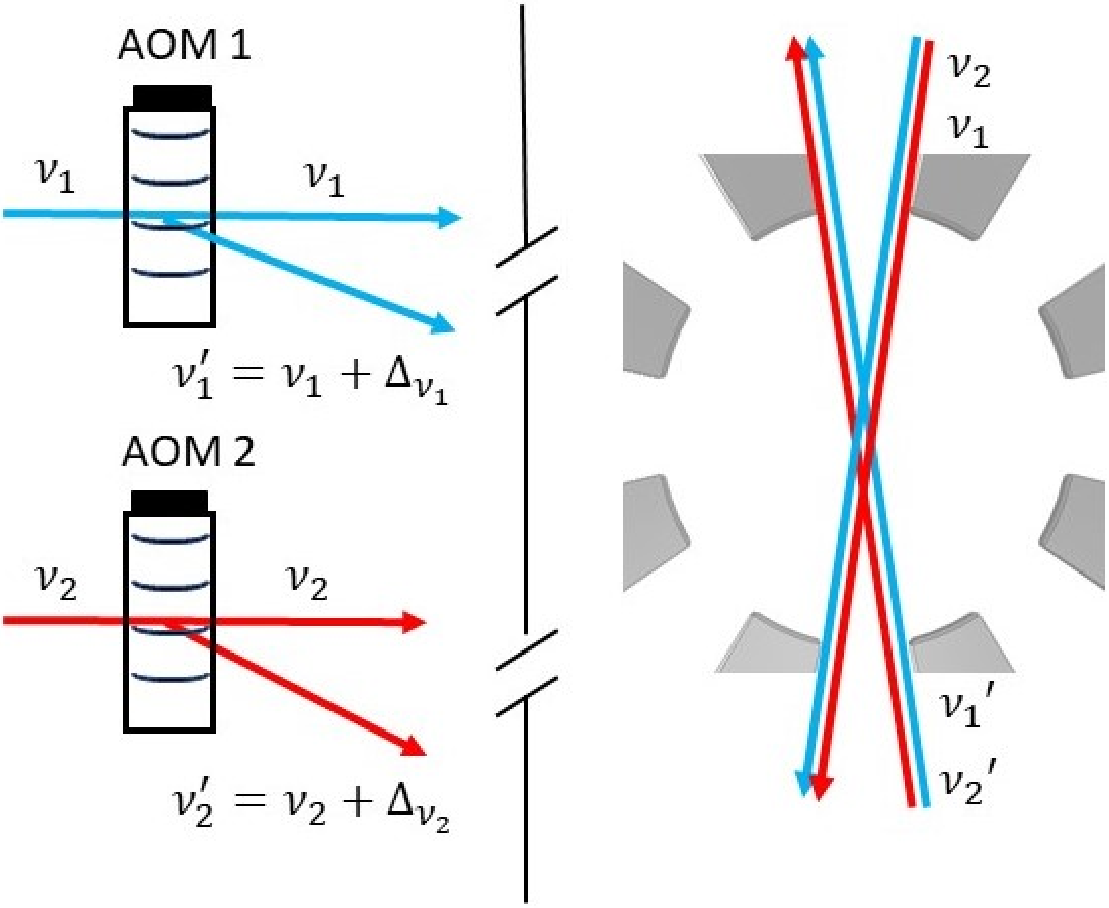

Figure 6.3: Schematic of the two tone laser cooling configuration. The 493 nm and 650 nm beams are split into two distinct frequency tones by AOMs. The unshifted beams (ν_1 and ν_2) and blue-shifted beams (ν_1' and ν_2') are combined separately, then counter-propagated through the trap.

of Δ_1 for different amplitudes of micromotion A fixing the lab frame repump laser detuning Δ_2 at -20 MHz. Assuming that the natural linewidths Γ_{31} and Γ_{32} of the $|1\rangle \leftrightarrow |3\rangle$ and $|2\rangle \leftrightarrow |3\rangle$ transitions, respectively, obey $\Gamma_{31} >> \Gamma_{32}$, the sign of the derivative $\frac{\partial \rho_{33}}{\partial \Delta_1}$ determines whether heating or cooling will occur, while its magnitude is proportional to the heating or cooling rate.

Distortions to the atomic resonance become pronounced when the Doppler shift due to micromotion is of the order of the power-broadened linewidth of a transition $\Gamma\sqrt{1+s} = \Gamma'$. In terms of the modulation index β this condition can be written as $\beta\Omega \simeq \Gamma'$. As one can see in Fig. 6.2, for $\beta > 3$ the absorption line shape starts to deviate significantly from the Lorentzian by becoming lower and broader. The detuning Δ_1 that correspond to the largest value $\frac{\partial \rho_{33}}{\partial \Delta_1}$, and thus the most efficient cooling, shifts to the red. The cooling rate decreases quickly, by a factor of $\simeq 10$ (Fig.

6.7) for an ion with $A = 0.25$ μm as compared to an ion with no micromotion.

As a result, the cooling beam must be farther red-detuned away from resonance for at least some of the ions in order to cool the ensemble enough to promote crystallization. Since the photon scattering rate is proportional to ρ_{33}, the off-resonant ions also appear brighter or dimmer in a time-integrated image [57] such as Fig. 6.1 (b). Yet ions with micromotion that is perpendicular to $\vec{k}$ do not vary in brightness. When the efficiency of Doppler cooling is lowered due to the distortions of the absorption line shape, the ions may not fully crystallize and appear as rings without fully localizing, or may fail to crystallize at all. When the amplitude of thermal oscillations exceeds the inter-ion spacing, we refer to the crystal as melted.

To address the distortions and cool large crystals, it has been proposed to implement multi-tone laser cooling, or to power broaden the transition and detune the cooling laser [29]. Power broadening may be limited by available laser power as the size of the crystal grows. For example, in our system, we can achieve a maximum saturation parameter of approximately $s = 20$ for a beam waist of 50 μm. The spectrum in this case is still quite distorted when $\beta = 15$, which occurs at $A \simeq 1.2$ μm. In addition, cooling rates are reduced and the Doppler-limited temperature is increased at higher saturation parameter values. This may lead to the onset of melting of the crystal due to low frequency (soft) normal modes of oscillation, where the amplitude of oscillations can exceed the ion spacing even at temperatures of 10s of mK. We note that over the last 15 years, additional red detuned cooling beams have been used by a rising number of groups to cool ions after large heating events based on empirical evidence of their utility. To the best of our knowledge, this work has not yet been published, and nobody has explored using a second cooling tone to improve cooling of ion crystals where ions experience differing amounts of micromotion.

We should point out that one may wish to operate in the regime $\Omega >> \Gamma$; in this case the spectrum is divided into micromotion sidebands separated by $n\Omega$ [24]. While this case may be useful, it is experimentally difficult to study since multiple cooling tones would be needed to cool even small 2D crystals, yet it may be easier to manage for larger ion crystals where the laser tones can be evenly spaced. Increasing Ω may also be impractical for some trap geometries where very high RF voltages would be needed, such as the present experiment. However, this strategy may be suitable for trap geometries with a small spatial size, such as a surface trap [25]. For our trap, a factor of two reduction in β by increasing Ω while maintaining reasonable trap strength would require greater than 2000 V amplitude of RF drive, which is typically enough to cause arcing in the RF delivery system. Thus, we do not explore this regime in this paper. We study the two-tone Doppler-cooling of 2D ion crystals with moderate power broadening and demonstrate that larger crystals can be stabilized.

Finally, we note that the steady state picture that we presented in this section is incomplete, since each ion is continuously changing in velocity and hence the amount of Doppler shift. While the steady state solution allows one to compute a laser frequency that results in net cooling over a period of micromotion, in reality, a constant frequency laser tone designed to address ions with a chosen amount of micromotion only cools optimally for part of each RF phase.

6.3 Experimental system and methods

The trap is mostly the same as described in chapter 4, with the addition of some HV capacitors to lower the RF drive frequency. RF at $\Omega = 2\pi \times 10.42$ MHz is delivered to the endcap electrodes via a double-coil helical resonator, resulting in trap voltages in the range 800-1500 V.

Two tones of Doppler cooling light for cooling beams are counter-propagated through the trap in the $\pm$ x direction as shown in Fig. 6.3, making an angle of $\theta \simeq 10^\circ$ with respect to the crystal plane. Both Doppler-cooling lasers at frequencies ν_1 (493 nm beam) and ν_2 (650 nm beam) are divided into two separate beam paths. One branch of each beam is double-passed through an AOM, generating a second frequency tone ($\nu_1' = \nu_1 + \Delta_{\nu_1}$ and $\nu_2' = \nu_2 + \Delta_{\nu_2}$). The AOMs are driven by a signal generators with variable amplitude and frequency (HP8640B), which is then amplified. This allows for the second frequency tone of each beam to be adjusted dynamically while maintaining the beam pointing.

The unshifted beams (ν_1 and ν_2) and shifted beams (ν_1' and ν_1') are combined separately and

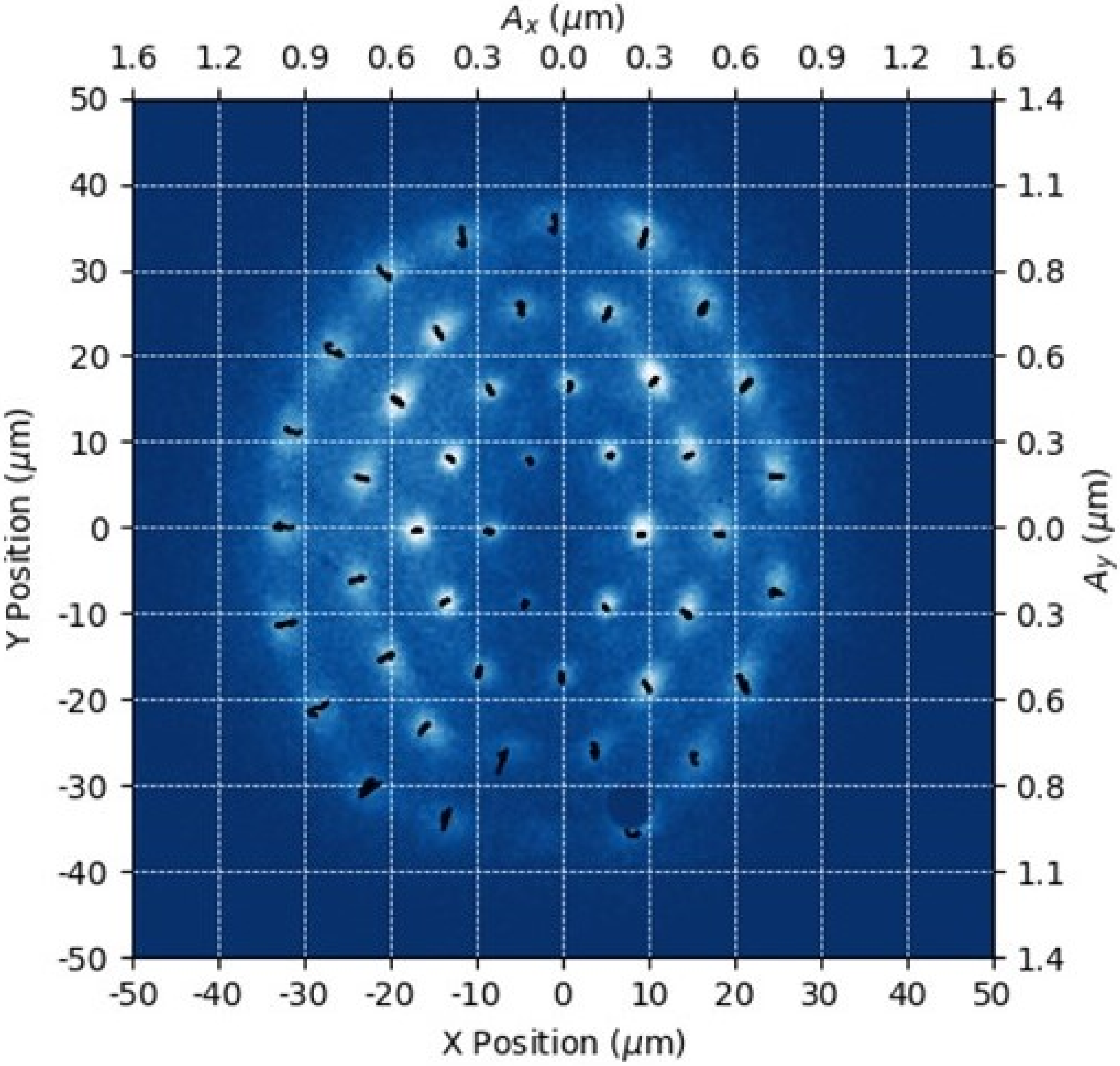

Figure 6.4: Example of data used to determine the location of the trap center and the planar Matthieu parameters q_x and q_y of the trap. (a) A 48-ion crystal, overlaid with the trajectory extracted for each ion over one RF period. There is a dark ion (different isotope of barium) located at the trap center. The dark spot at $(x,y) \simeq (8,-32)$ is a dead spot on the intensifier, which is also present in ion images in Fig. 6.6. The trap secular frequencies are $(\omega_x, \omega_y, \omega_z) = 2\pi \times (214, 185, 788)$ kHz. b) Micromotion amplitude of ions in both the x- and y-direction as a function of the equilibrium position of the ions. The amplitude is allowed to be negative as the phase changes over the RF null. The straight line is a linear fit to the data where the intercept with the horizontal axis indicates the trap center (red dashed lines).

counter-propagated through the trap. The beams are focused to a waist of approximately 50 μm. Trap frequencies are measured by frequency modulating the RF drive and observing fluorescence dips on a PMT, as outlined in chapter 4.

The ions are imaged using the objective described in chapter 4 onto the Tpx3Cam. For the data taken using the Tpx3Cam, we first fold single photon events into a single period of the RF drive (96.0 ns). The position of the ion is tracked over the period by fitting the image of each ion to a rotated elliptical Gaussian for frames that consist of equal increments in time, similarly to previously established methods [79]. The position over T is then fit with a sinusoid according to Eq. 6.2.1. The amplitude of micromotion and the equilibrium position are extracted from the fit. Finally, the micromotion amplitude of each ion is plotted against the equilibrium position position and a linear fit is used to extract the slope and intercept with the horizontal axis, yielding the parameter q_x and q_y and the location of the trap center. This information is used to determine

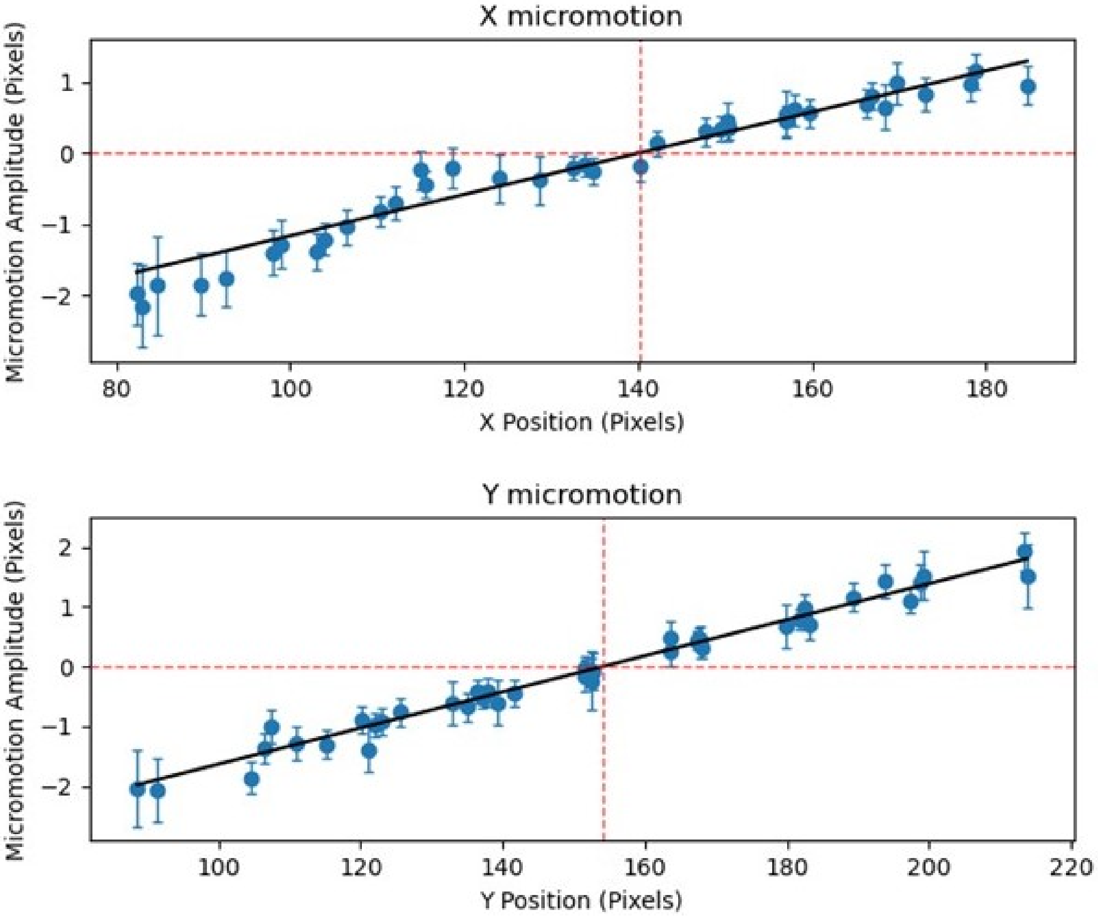

Figure 6.5: Plots of x and y micromotion vs x and y position for each ion from Fig. 6.4. Using a least squares fit, we extract the slop of each line and hence the Matthieu parameters q_x and q_y.

the scale of A_x and A_y in the ion images. Fig. 6.4 shows an example of such a measurement. A 48-ion crystal is stabilized in the trap, shown in Fig. 6.4, and the micromotion amplitude vs. ion equilibrium position for both x- and y-axis is shown in Fig. 6.5.

Δ_{ν_1} and Δ_{ν_2} are empirically determined as follows. We first trap a crystal (3 shells) using only a single, unshifted tone of each cooling beam at ν_1 and ν_2, blocking the blue-shifted tones at ν_1' and ν_2' . We measure the amplitude of micromotion for outer ions using the technique described above. We then use the results of these preliminary measurements as a starting point for the estimating Δ_{ν_1} and Δ_{ν_2} using the simulations depicted in Fig. 6.2, aiming for a detuning that maximizes ρ_{33}.

Next, ν_1 and ν_2 are adjusted so that the outermost ions appear brightest, indicating where ρ_{33} is maximized. The tones at frequencies ν_1' and ν_2' are then unblocked, and their effect on the crystals are observed while dynamically adjusting Δ_{ν_1} and Δ_{ν_2}.

6.4 Results and discussion

We observe that tuning Δ_{ν_1} has a pronounced effect on the ability to cool and stabilize large ion crystals, and often causes crystallization or melting to occur as the value is changed. We observe that increasing Δ_{ν_1} towards its optimal value appears to make the crystal colder, until it is suddenly heated and melts. This likely occurs as the ν_1' reaches a high enough frequency to heat outer ions in the crystal that have higher micromotion amplitudes. We position Δ_{ν_1} just below this point. Δ_{ν_2} is then adjusted around its original setting but observed to affect the crystal to a much lesser extent. We observe that once a crystal with four shells has formed, the second tone can then be blocked and the ions remain crystallized for approximately 10 seconds before melting. The crystal will then not reform until the second tone is reintroduced.

We find that setting $\Delta_{\nu_1} = 101$ MHz and $\Delta_{\nu_2} = 66$ MHz allows us to trap and cool larger radial 2D crystals than we were previously capable of with a single-tone Doppler cooling setup. The best results are achieved by slightly compressing the crystal along the axis of propagation of cooling light, in order to reduce the extent of micromotion along that direction. The crystal shown

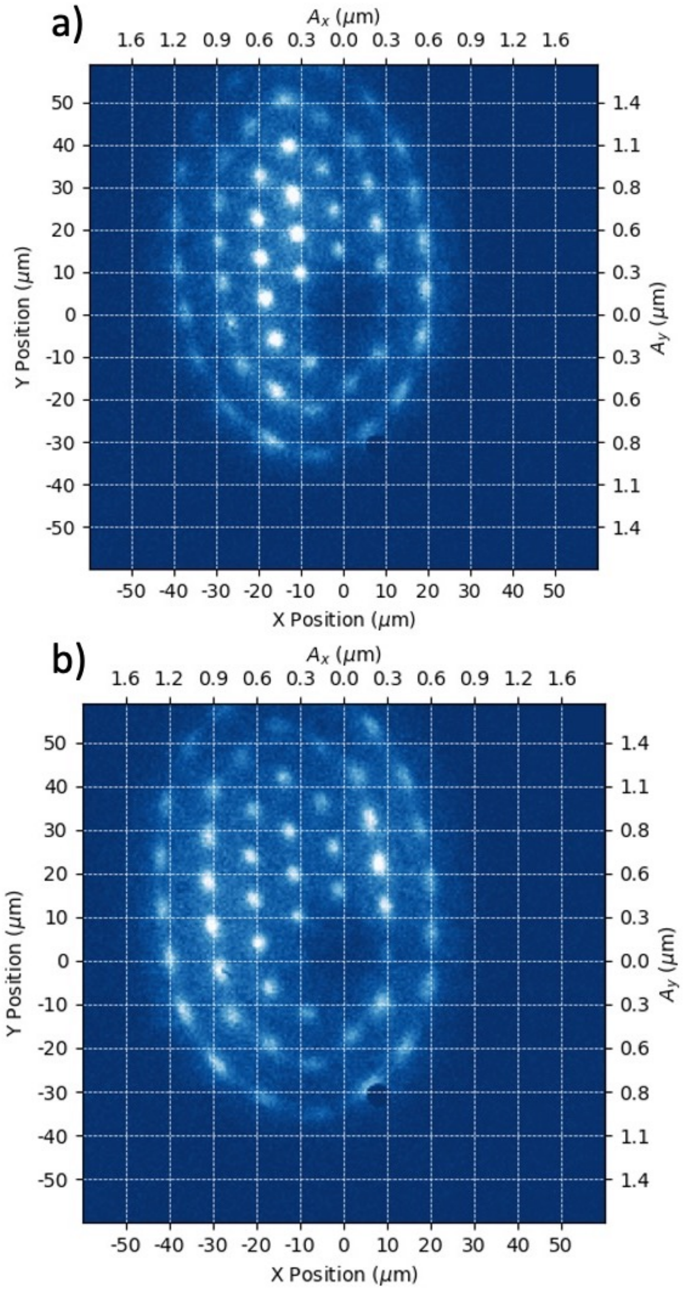

Figure 6.6: A 54-ion radial 2D crystal at different phases of micromotion. There are four dark ions (different isotopes of barium) located near the trap center. The trap secular frequencies are $(\omega_x, \omega_y, \omega_z) = 2\pi \times (203, 147, 768)$ kHz. (a) The minimal extent of the crystal that corresponds to the phase of the micromotion when all ions are closest to the trap center. The top-most ion lies outside of the image area for most of the RF period, but can be seen here. (b) the maximal extent of the crystal that corresponds to the phase of the micromotion when all ions are farthest from the trap center. Both images are integrated over time intervals that correspond to 1/36 of the RF period (approximately 2.67 ns).

in Fig.6.4 has 48 ions. By fitting the data of micromotion amplitude vs. position, we find the horizontal intercept (trap center) (x,y)=(140,153)±(6,6) pixels and the slope (in-plane Matthieu parameters) ($q_x/2$,$q_y/2$)= (0.032,0.028)±(0.001,0.001).

The largest crystal we are able to stabilize is a 54-ion crystal shown in Fig. 6.6. To our knowledge, this is the largest radial 2D ion crystal ever produced, where all ions in the crystal are efficiently cooled and localized to less than the ions' spacings. The two panels in Fig. 6.6 correspond to the two opposite phases of micromotion with the minimal (a) and maximal (b) crystal spatial extent.

The largest amplitude of micromotion here exceeds 1.5 μm, which corresponds to a peak-peak oscillation of 6 pixels on the camera image. This peak-peak distance is more than two times larger than the diffraction limited spot size of our system of 1.1 μm, and is clearly visible in a time-integrated image (Fig. 6.8). In our crystals, β ranges from 0 at the center of the crystal to greater than 15 for ions at the top left corner of Fig. 6.6.

Although the crystals are cooled enough that individual ions can be resolved, thermal motion is clearly visible in the larger crystals. Measuring this temperature may be difficult, since the established methods will likely fail for crystals with significant micromotion. Scanning the cooling laser will not yield useful results, since the response of each ion is different. Methods for thermometry of ion clouds under micromotion have been established [94], but do not extend to the temperature range where crystallization occurs.

We use the MD simulations to estimate the temperature of the 54-ion crystal. By finding a simulation that yields a crystal with a similar spatial extent of the ion images, we estimate the temperature [54]. For the 54-ion crystal, we find that the trajectories are consistent with temperature of $\sim$20 mK, approximately 7x higher than the estimated cooling limit in this power-broadened system. The results are shown in Fig. 6.8.

We also compare this to the spatial extent of outer ions in the crystal with the lowest calculated normal mode frequency [89]. The data collected is folded into a single period of micromotion. In order to separate out spreading due to micromotion from thermal motion, we select data from

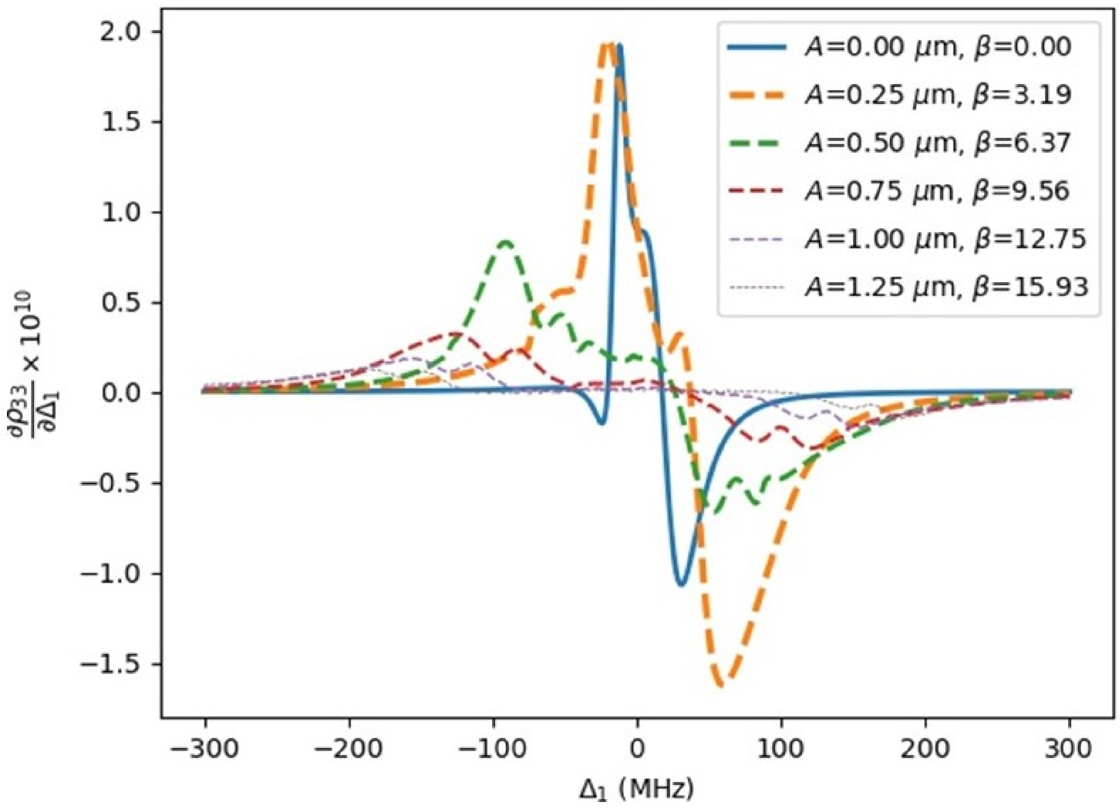

Figure 6.7: Integrated image of 54 ion crystal and simulated images at various temperatures. a) Data taken with the Timpepix3 camera, the same as used in Fig. 6.6. b) Simulated image of the crystal at 10 mK. c) simulated image of the crystal at 20 mK. d) simulated image of the crystal at 30 mK. Here, the onset of radial melting can be seen as the ions in the outer shells begin to delocalize. The point spread function of the imaging optics is not applied to the simulated ion images.

only 1/16th of the period. The ion fluorescence profile is the fit to determine the Gaussian rms spread of the ions in the outer shell, taking into account the finite spot size due to our imaging optics [95]. We assume that at equilibrium, the thermal occupation of all modes is equal. Then, according to the spatial extent of the outer ions' motion and the lowest calculated normal mode frequency, the temperature is approximately 20 mK, in good agreement with the result obtained from the simulated images.

In Fig. 6.7, the derivatives of the curves seen in Fig. 6.2 in the main text are shown, so as to compare the relative cooling rates at different micromotion amplitudes. Even for ions with just 0.25 μm of micromotion amplitude, the cooling rate is decreased by a factor of 10 relative to an ion with no micromotion.

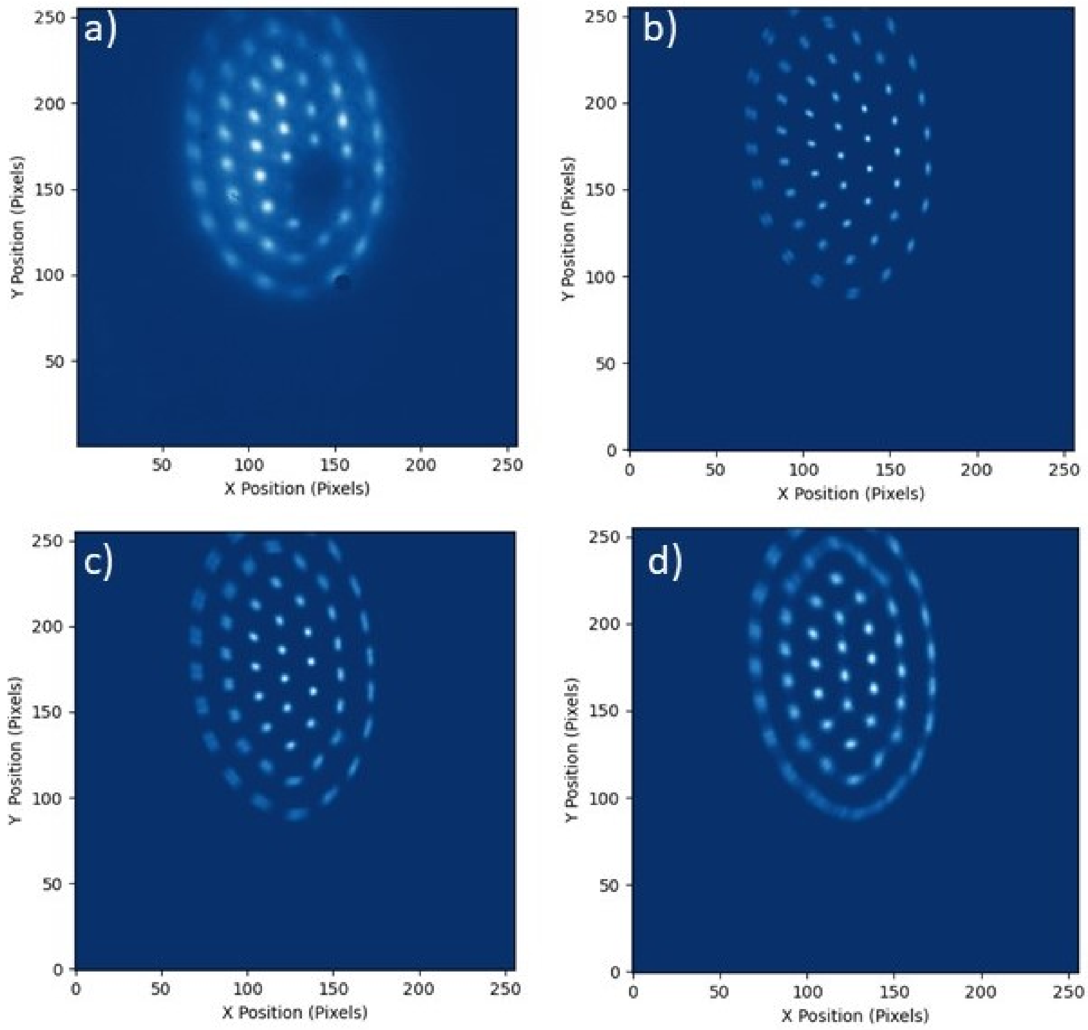

Figure 6.8: Integrated image of 54 ion crystal and simulated images at various temperatures. a) Data taken with the Timpepix3 camera, the same as used in Fig. 6.6. b) Simulated image of the crystal at 10 mK. c) simulated image of the crystal at 20 mK. d) simulated image of the crystal at 30 mK. Here, the onset of radial melting can be seen as the ions in the outer shells begin to delocalize. The point spread function of the imaging optics is not applied to the simulated ion images.

The high temperatures are likely the result of a combination of the decrease in cooling rates in Fig. 6.7 due to the distortion of the atomic lineshape, and due to power broadening. Additional tones may help produce larger, or colder crystals using Doppler cooling techniques. However, while additional tones may increase cooling efficiency in some areas of a crystal, they may lead to heating in others. It may also be necessary to control the spatial extent of the laser beams that provide the additional tones to selectively reduce this effect. Finally, a second set of beams at 90° may also further increase cooling capabilities of large crystals.

For larger crystals than studied here, the frequency of the soft modes may drop even further [27] and lead to even lower melting points. This could further limit the extent of power broadening and in order to keep the Doppler temperature below the melting point, and increase the emphasis on multiple cooling tones. Further study is needed to determine the limitations to radial 2D crystal size using Doppler cooling techniques.

The cooling techniques studied here will need to be further improved in order to be useful for quantum information applications. The large amplitudes of thermal motion may contribute to errors in the addressing of qubits by laser light, as individual ions move out of a focused laser beam or other ions move into its path. However, as long as the amplitude of thermal motion is kept smaller than the inter-ion spacing, the crystals should still form. While the amplitude of thermal motion may be large in the plane of the crystal, in the transverse direction, it has been shown that sub-Doppler cooling is possible [56], and that the transverse motion is well decoupled from in-plane motion [55].

In summary, we demonstrate two-tone Doppler cooling of radial 2D crystals of trapped ions. We show that having a second, counterpropagating laser tone helps cool larger radial 2D crystals. We are able to trap, stabilize and efficiently cool crystals with up to 4 shells, and 54 ions. The micromotion of ions in the crystals is analyzed and used to extract the planar Matthieu parameters q_x and q_y, as well as to locate the trap center.

Chapter 7

Micromotion-synchronized pulsed Doppler cooling

7.1 Introduction

To trap and cool large 2D crystals, it may be important to it least have some of a beam's k-vector point in the direction of micromotion. Hence, the detrimental effects on Doppler cooling must be overcome. Due to micromotion, the cooling laser frequency in each ion's rest frame is continuously Doppler-shifted by varying amounts across a crystal. This causes the absorption spectrum and range of frequencies for which steady state cooling is efficient to vary for different ions. The results of chapter 6 suggest that multi-tone Doppler cooling may be an avenue for stabilizing even larger crystals.

There exist two points per RF period T where the velocity $v = 0$ for all ions simultaneously. In this chapter, I propose to use $\sim$ns laser pulses synchronized with the nodes in the micromotion velocity (dashed line in Fig. 7.1 (a)) in order to narrow the range of ion speeds which need to be addressed by the cooling beam. I then show that this technique can be useful when cooling multiple ions with differing amounts of micromotion using a single-tone laser beam.

Pulsed Doppler cooling has been used before with the intention of broadband cooling [95]

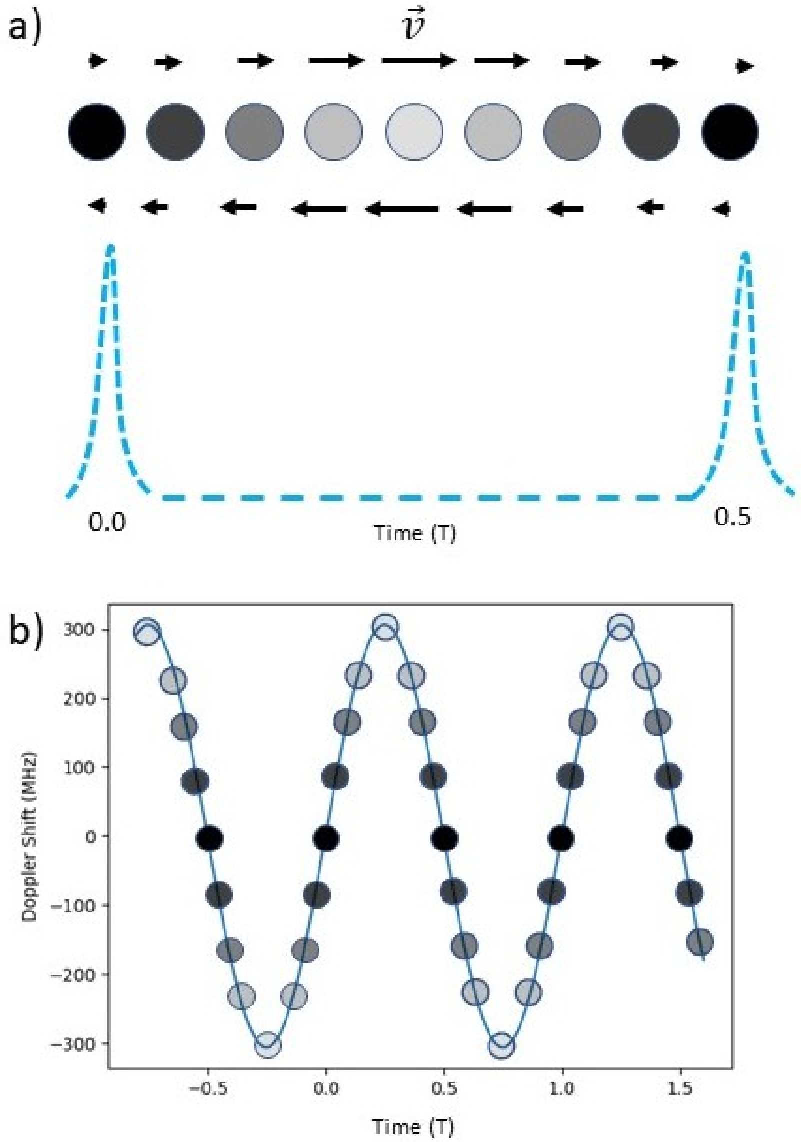

Figure 7.1: a) An ion oscillating back and forth at frequency Ω in the direction of the wave vector $\vec{k}$ of a cooling beam leads to a time dependent Doppler shift. The transparency of each dot represents the magnitude of it's velocity $\vec{v}$, also indicated by the arrows. By pulsing a laser on (laser intensity indicated by the dashed line) during only a small portion of the ion's trajectory when the velocity is minimal (darkest points), one can selectively cool a smaller velocity class. Time is measured in units of the RF period T. b) Doppler shift of a 493 nm light in the reference frame of a Ba^+ ion undergoing micromotion at 8 MHz with 3 μm amplitude. The instantaneous Doppler shifts exceed 300 MHz, which is large compared to the 15 MHz natural linewidth of the transition.

or generating frequency comb teeth deep into the UV range, offering to reduce the complication associated with harmonic generation of light [96, 97]. However, laser pulses have not been used to cool trapped ions synchronized with the trap RF.

Previous approaches to modelling Doppler cooling under micromotion have relied on time averaging steady state solutions to the Schrodinger's equation or the optical Bloch equations by sampling velocities over a period of micromotion to produce an atomic absorption spectrum [93, 29, 24]. Yet in the presence of significant micromotion, the cooling is not steady state since ions may be experiencing Doppler shifts much larger then the linewidth of the atomic transition Γ and rapidly changing on a timescale similar to the excited state lifetime τ. Moreover, pulsed lasers cause frequency combing effects and fast intensity changes that cannot be captured in the steady state. Therefore, to understand how pulsed Doppler cooling works, we numerically solve the time-dependent optical Bloch equations.

7.2 Pulsed Doppler cooling

Consider a crystal of $^{138}\mathrm{Ba}^+$ ions undergoing micromotion at a frequency $\Omega = 2\pi \times 8$ MHz (period $T = 2\pi/\Omega = 125$ ns), interacting with the 493 nm Doppler-cooling laser (natural linewidth $\Gamma_{32} = 2\pi \times 15$ MHz) and 650 nm repump laser (natural linewidth $\Gamma_{32} = 2\pi \times 5$ MHz), Fig. 3.6. These values are similar to what our experiment is capable of, and are well representative of the regime where $\Omega < \Gamma_{32}$. Each ion experiences oscillations around a fixed point described by $\vec{r} = A\cos(\Omega t)$ where $A = qr_0/2$ is the micromotion amplitude. Here, r_0 is the displacement of the equilibrium position of the ion from the trap center, and q is the relevant Matthieu parameter. Hence, the instantaneous velocity is $v = A\Omega\sin(\Omega t)$, and the instantaneous Doppler shift in the ion's rest frame is $\vec{k} \cdot \vec{v} = kA\Omega\sin(\Omega t)$, where $\vec{k}$ is the laser wave vector. An example of this is shown in Fig. 7.1 (b) for an ion with micromotion amplitude $A = 3$ μm.

We now introduce the effect of a pulsed laser. We consider pulses with a Gaussian temporal profile, such that the intensity of the pulse I is given by

$$I(t) = I_{peak} e^{-\frac{(t-t_p)^2}{2\sigma^2}}, \tag{7.2.1}$$

where I_{peak} is the maximum intensity. The pulses are centered at the desired time t_p, and σ is the

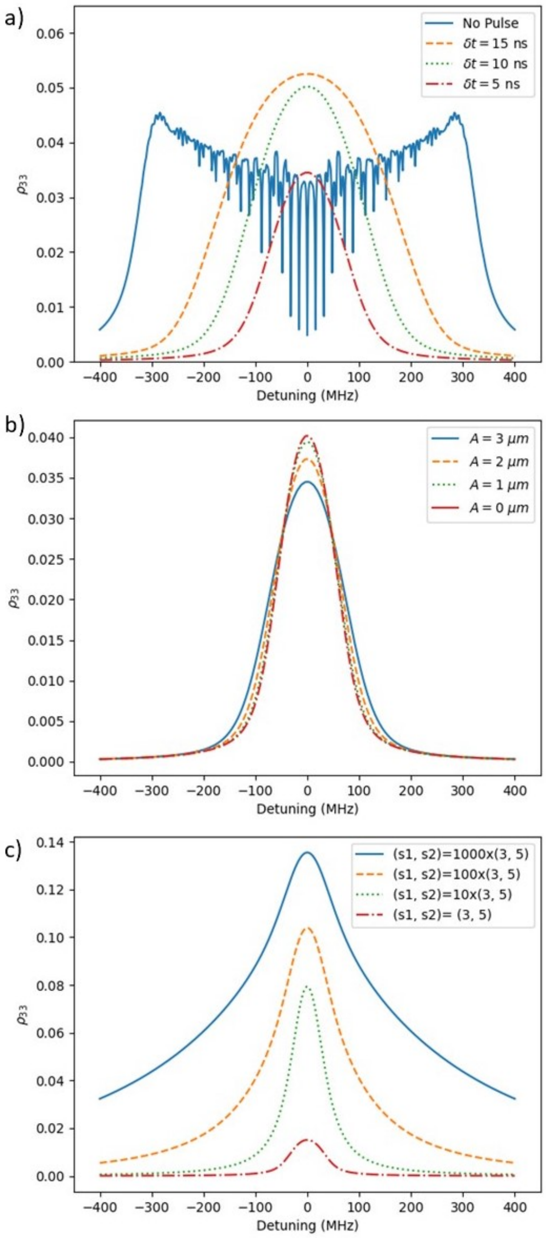

Figure 7.2: Benefits of using pulsed Doppler cooling. Excited state population ρ_{33} is plotted as a function of the cooling laser detuning Δ for: a) different pulse widths δt and fixed amplitude of micromotion $A = 3\ \mu$m, b) fixed pulse width $\delta t = 5$ ns and different micromotion amplitudes A. This is close to the condition of Eq. 7.2.4. c) fixed $\delta t = 10$ ns, $A = 0\ \mu$m and different cooling laser intensities listed in terms of the saturation intensities s1 and s2 of the cooling and the repump lasers, respectively. Narrowing the pulse width narrows the absorption spectrum considerably, leading to a more uniform spectrum across ions with differing amounts of micromotion. This may lead to an improved average cooling rate over the entire crystal. Saturation affects the cooling spectrum in a similar way to the steady-state case, but at higher average laser powers.

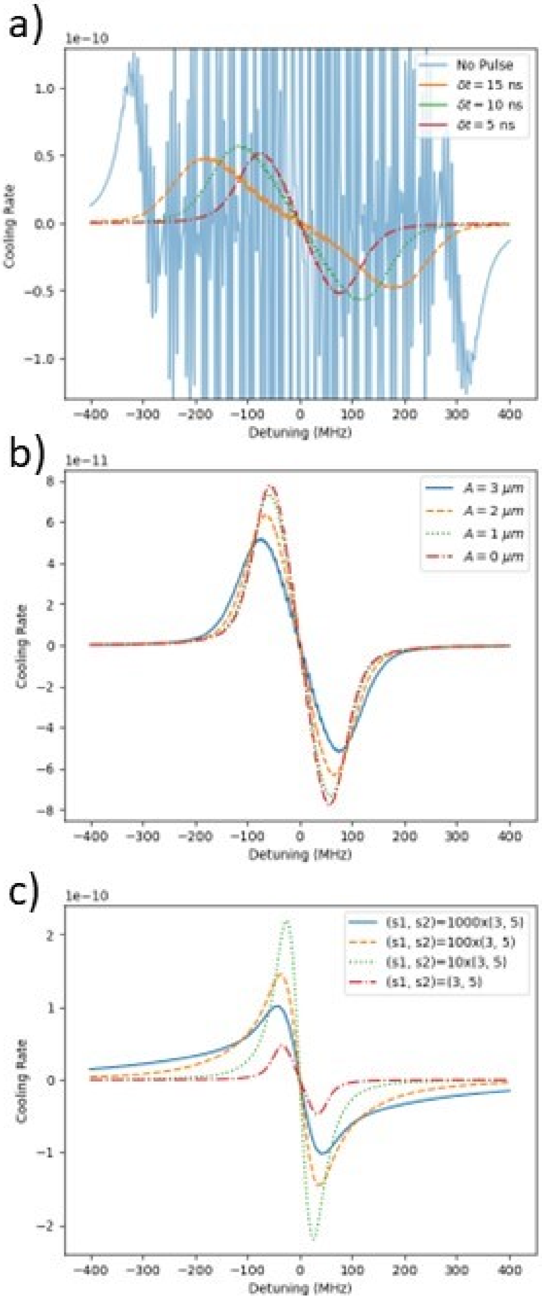

Figure 7.3: Cooling rates corresponding to the scenarios in Fig. 7.2. a) Fixed $A = 3\ \mu$m with different values of δt. b) Fixed $\delta t = 5$ ns with different values of A. c) Fixed δt=10 ns with no micromotion and different saturation levels.

standard deviation of the Gaussian pulse (the FWHM $\delta t = 2.36\sigma$). The ion's velocity crosses 0 at times $t_n = nT/2$ where n is an integer. Therefore, the lasers can be pulsed up at Ω or 2Ω while selecting velocities near $v = 0$. As we will see, I choose to pulse the lasers at Ω, with a phase shift of π between the two beams.

The equations are solved using a 4th order Runge-Kutta algorithm, keeping time steps small compared to T ($<< 1ns$). We let the system evolve until it reaches a form that is periodic over the RF period, typically about 50 T. We then let the system evolve for additional 100 T.

We model the behaviour of the excited state population, ρ_{33}, as shown in Fig. 7.2. In order to compute the absorption spectra, we time-average the solutions over many periods of micromotion. In Fig. 7.2 (a) we show the benefits that can be obtained by pulsing the cooling beams, as opposed to continuous cooling, for different pulse widths. The absorption spectrum for continuous cooling obtained via this method (solid line in Fig. 7.2 (a)) is similar to those found using the steady-state model [93], yet the adverse effects due to CPT are far more pronounced. As the amplitude of micromotion becomes large, multiple dips appear at multiples of Ω. This is in contrast to the steady-state solutions, where these CPT features smooth out as the spectrum becomes power broadened [93]. In Fig. 7.2 (b) we plot the absorption spectra for the fixed laser pulse width of 5 ns and various micromotion amplitudes. We note that the absorption line width remains essentially unchanged as the micromotion amplitude increases from 0 to 3 μm. In Fig. 7.2 (c) we show the effect of power broadening in pulsed cooling, which shows the expected behavior of the line width increasing at higher laser intensities. The cooling rates corresponding to the scenarios in Fig. 7.2 are shown in Fig. 7.3.

In order to cool the ions effectively we must take into consideration the level of velocity selection due to the pulse width, the frequency combing effects from the pulse train, the influence on CPT dips, and the saturation effects. Each has a substantial impact on cooling efficiency and must be considered individually and with respect to each other.

First, we consider the effects of CPT when cooling using pulsed lasers. For a three-level Λ-system such as $^{138}\mathrm{Ba}^{+}$, the combined effect of the CPT and the frequency combing leads to a complicated absorption spectrum that does not yield good cooling. Instead, by alternating the cooling and the repump pulses at frequency Ω (as can be seen, for example, in Fig. 7.4 (b)), we can eliminate the CPT effect altogether. In this case the cooling transition and repump are never illuminated simultaneously and we have that $2\pi/\Gamma = \tau << T$ and the absorption spectrum resembles a two-level system (for the following discussion $\Gamma = \Gamma_{31}$). The CPT dips no longer exist and do not effect the absorption spectrum under micromotion. We also note that for a true two-level system such as $^{114}\mathrm{Cd}^{+}$, the CPT effects would not be a consideration.

Next to consider are the frequency comb effects, which can also be detrimental to the cooling process. Consider a Gaussian laser pulse with a standard deviation σ, and thus a FWHM $\delta t = 2.36\,\sigma$. Narrow pulses give the best velocity selection, but too narrow and combing effects become a nuisance, as more teeth fit into the comb envelope and broaden the absorption spectrum. The repetition rate $f_r = \Omega/2\pi$ with pulse width δt produces a comb with teeth separated by f_r and envelope width $\delta f = 1/\delta t$. If $\Gamma > \Omega$ then the teeth are not resolved and the effect is a broadening of the absorption spectrum to width $\Gamma_c \sim \delta\nu$, where Γ_c is the approximate comb broadened

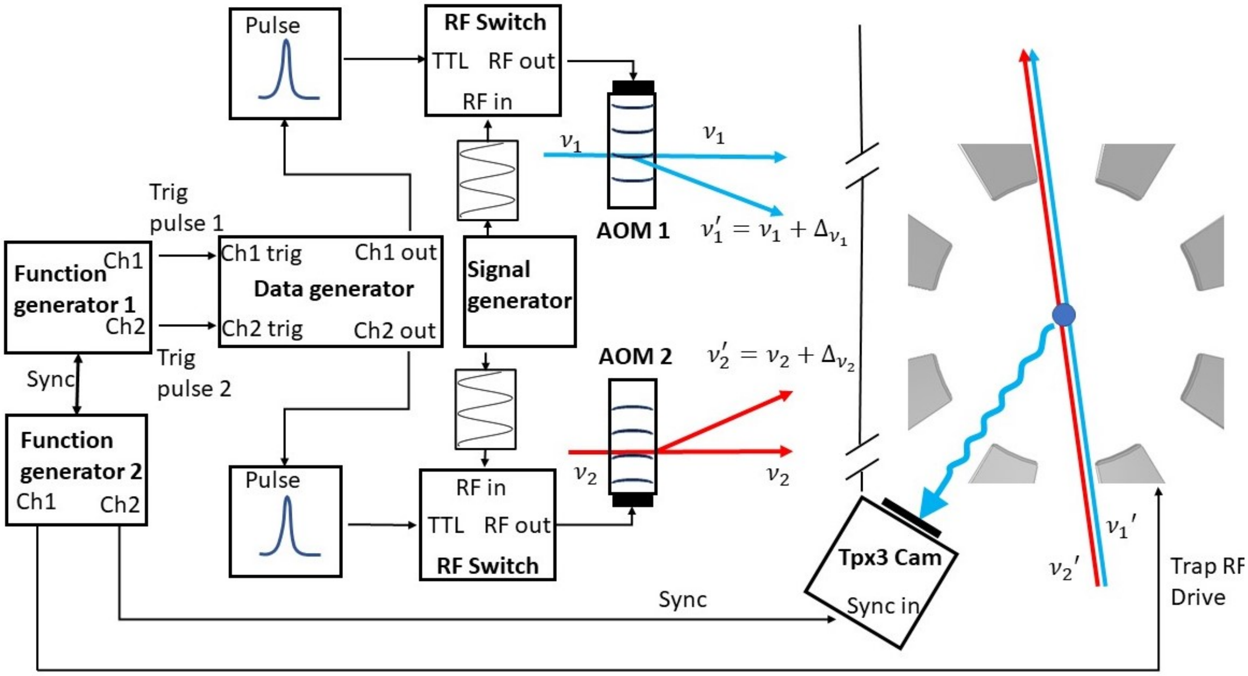

Figure 7.4: Schematic for pulsed laser cooling and temporal profile of laser pulses. a) The schematics of the experimental setup. Optical pulses at frequency ν_1' and ν_2' are generated via AOMs, using the first diffracted order. The two pulsed beams are combined after the AOMs and sent to the trap. RF pulses that drive the AOMs are generated by sending short TTL pulses from a programmable data generator into fast RF switches. Two phase-locked RF synthesizers are used to drive the trap RF, to synchronize data acquisition and time measurement with the fast camera, Tpx3Cam, and to trigger the pulses from the data generator.

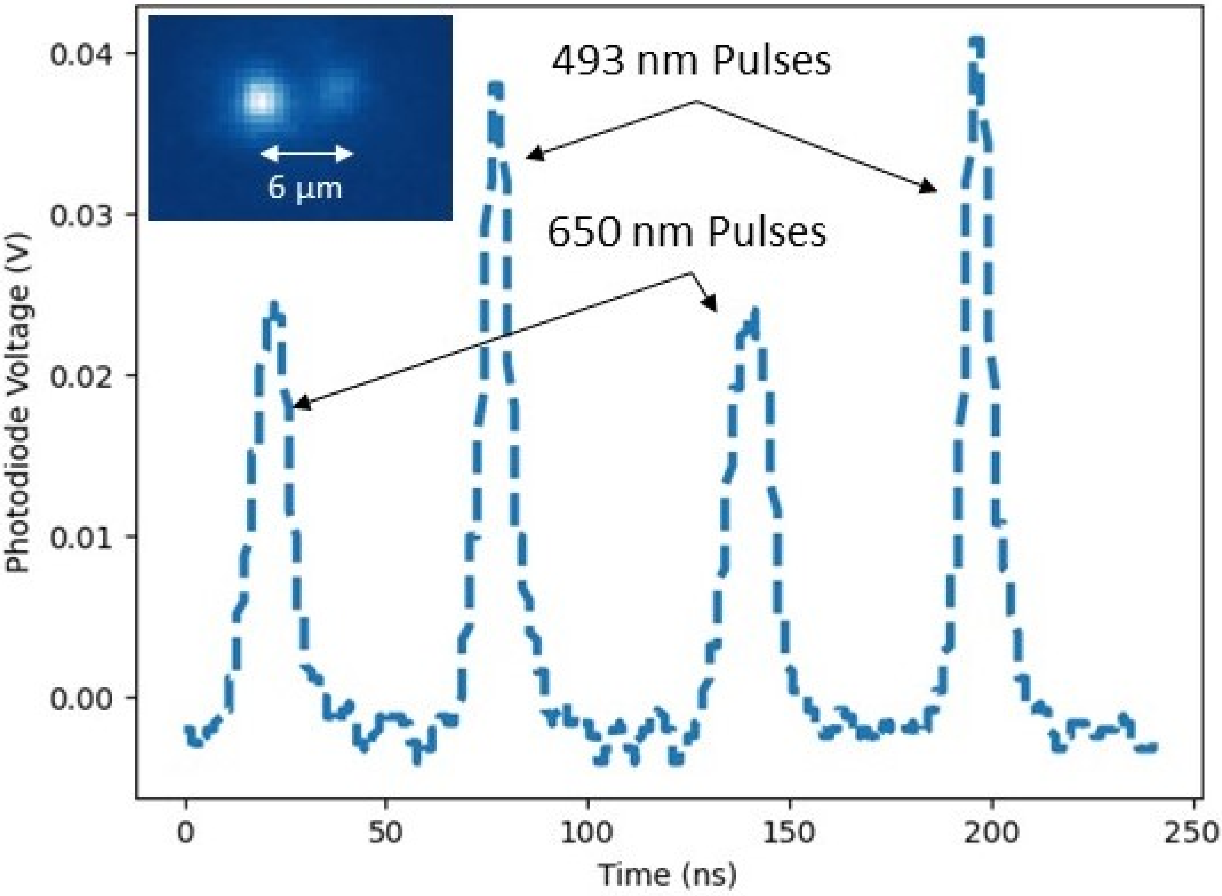

Figure 7.5: Temporal profiles of the combined 493 nm and 650 nm optical pulses used in the experiment measured with a fast photodiode. The pulses are found to have δt of 10 and 13 ns respectively for 493 nm and 650 nm light. Inset: single ion cooled using laser pulses synchronized with the trap RF. Using this technique, the ion is illuminated only at its endpoints of the micromotion trajectory. The micromotion amplitude is measured to be $\sim 3\ \mu$m.

linewidth. In our case, we restrict our attention to the case $\Gamma > \Omega$, since it is experimentally feasible given the range of trap strengths and the ion species used.

On its own, pulsing does not improve the Doppler cooling. However, in the presence of significant micromotion the pulsing can be effective in narrowing the width of the absorption spectrum. The approximate absorption linewidth due to micromotion broadening Γ_Ω is twice the maximum Doppler shift $\vec{k} \cdot \vec{v}_{max}$. Yet in addition to this broadening, the absorption spectrum is also distorted. When we pulse the lasers such that $\Gamma_c < \Gamma_\Omega$, improvements can be seen. This can be thought of as an effective reduction of the micromotion modulation index $\beta = kv_{max}/\Omega$. For an ion cooled by a pulsed laser, velocity selection using a pulse with a width δt leads to $v'_{max} = A\Omega^2\delta t$, while for a continuously cooled ion, $v_{max} = A\Omega$. Therefore we obtain an expression for a reduced modulation index β'

$$\frac{\beta'}{\beta} = \frac{v'_{max}}{v_{max}} = \Omega\delta t \tag{7.2.2}$$

in the limit $\delta t/T << 1$. Thus, we find the approximate condition where pulsing is effective when $\Gamma_c \leq \Gamma_\Omega$, that is

$$2\pi\delta f \leq 2\beta'\Omega \tag{7.2.3}$$

leading to the condition

$$\delta t \geq \sqrt{\frac{\pi}{\beta\Omega^2}}. \tag{7.2.4}$$

For example, with $A = 3\ \mu m$ at $\Omega = 8$ MHz, we have that $\delta t \geq 5.6$ ns. In this limit, the cooling rate of a single ion does not improve, but the average cooling rate across all ions in a crystal can be improved dramatically when considering a single cooling beam.

Finally, one must consider the power broadening. Since the laser is pulsed, only a fraction of the power is delivered to the ion in contrast to the continuous wave laser cooling. Saturation and saturation intensity are steady-state concepts, yet some intuition can be gained by replacing the saturation parameter s with a reduced saturation parameter, $s' = s(\delta t/T)$. The power broadened linewidth is then reduced to $\Gamma_{s'} = \Gamma\sqrt{1+s'}$.

We note that the scenario would be quite different in the case $\Gamma < \Omega$. In this case the effect of micromotion is to cause resolved sidebands in the absorption spectrum spaced at Ω [29, 24]. Therefore, pulsing the laser at Ω would add comb teeth spaced equally to the micromotion sidebands. One could align teeth with sidebands in order to maintain cooling. This would not require selecting nodes in the velocity due to micromotion. Moreover, since the comb teeth are resolved, the features of the absorption spectrum may not be broadened. We leave this regime to be further explored.

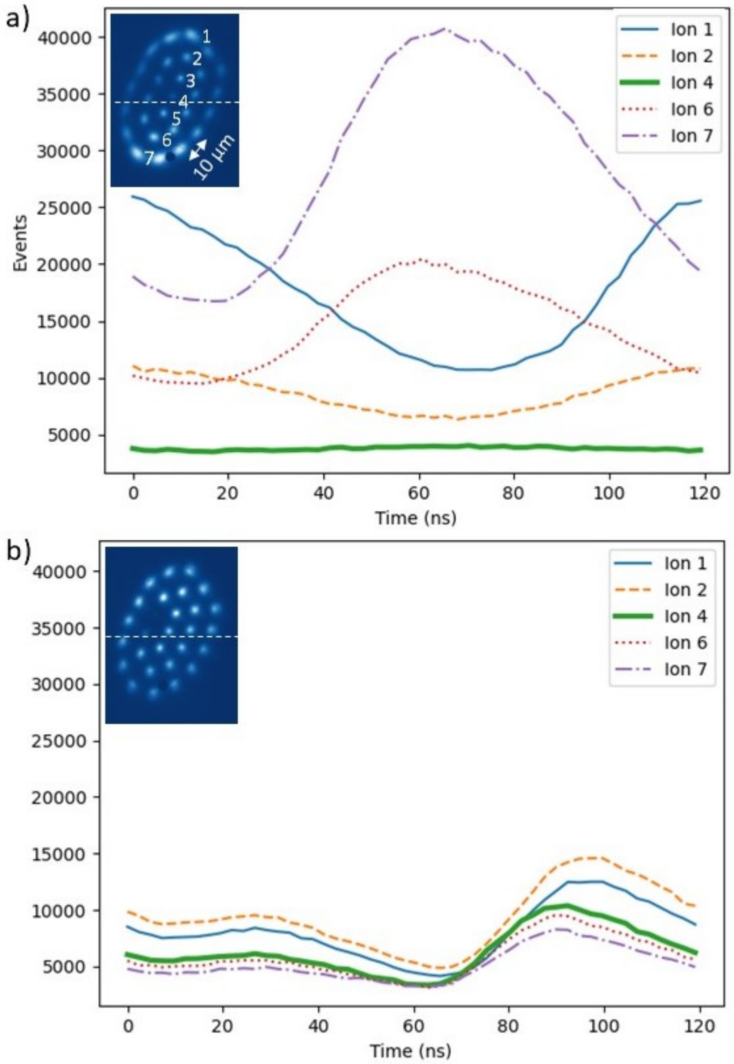

Figure 7.6: Scattering rates of single ions over the RF period T for the continuously cooled (a) and pulsed cooled (b) 28-ion crystal centered near the trap RF null, taken with the Tpx3 camera. The trap frequencies are $(\omega_x, \omega_y, \omega_z) = 2\pi \times (193, 266, 737)$ kHz. Insets are integrated EMCCD images of the crystals. The laser propagates in the y (vertical) direction in these images, and the dashed lines represent $y = 0$. Ion spacing is approximately 10 μm. Each curve represents fluorescence of a single ion, as labelled in the inset of (a). These ions are chosen to represent the wide distribution of micromotion amplitudes across the crystal. Vertical scales in arbitrary units are identical in both panels. a) Relative scattering rates of ions 1,2,4,6 an 7 over an RF period using continuous laser cooling. Broad variations of the scattering rates due to Doppler shifts can be seen between different ions with different micromotion amplitudes. b) Same as (a), but with pulsed laser cooling. Scattering rates for different ions are now nearly identical. The scattering rate variation over the trap period is due to the pulsed nature of the lasers cooling.

In summary, shorter pulses will help to cool an ion until the condition in Eq. 7.2.4 is reached. Therefore, when considering a large crystal, one should consider the distribution of amplitudes of micromotion. Shorter pulses will help cool ions where the amplitude of micromotion is greater and where a large range of micromotion-induced Doppler shifts needs to be covered, but it will not help if the micromotion amplitude is small, or if cooling to near the Doppler limit is needed. However, average cooling rates across all ions may be improved, leading to an overall lower crystal temperature.

7.3 Experiment and methods

The ion trap and the Doppler cooling setup is similar to the one described in chapters 4 and 6, with the RF drive frequency further reduced to 8.39 MHz. Pulses of cooling light are created using Crystal Technology 3200 series AOMs with a central frequency of 200 MHz, driven by a HP 8657D signal generator. The RF signal at 200 MHz is sent to the AOMs through Minicircuits ZASW-2-50DR+ switches that have a typical rise/fall time of 6 ns. The switches are controlled using a DG2020A Data Generator that has a rise/fall time of 2 ns.

The trap RF is produced by a Siglent SDT 2042X arbitrary waveform generator. The second channel of the generator is used to send trigger pulses at 100 kHz to the Tpx3 camera to synchronize the camera internal timing with the trap RF. A second Siglent SDT 2042X arbitrary waveform generator is phase-locked to the first one using the 10 MHz time base, and is used to trigger the DG2020A Data Generator. Two channels of the second Siglent SDT 2042X with adjustable phase allow the relative timing of the 493 nm and 650 nm laser pulses to be tuned, as well as the relative phase of both pulses with respect to the trap RF. A schematic of the setup is shown in Fig. 7.4.

Laser pulses are measured using a Thorlabs PDA10A fast photodiode and Rigol DS 1202-ZE oscilloscope. The pulse parameters are roughly adjusted so that the pulses are separated to as close to $T/2$ as possible given the granularity of DG2020A ($\sim$ 5 ns). The width of the pulses is determined to be 10 ns and 13 ns for the 493 nm and the 650 nm lasers, as depicted in Fig. 7.5. For each beam, the total power is measured to be approximately 1/10th of the continuous wave power.

We find that it is necessary to use full power (i.e. non-pulsing) cooling laser beams when first forming the ion crystals with more than a few ions. We cool crystals using a red-detuned lasers as used in previous experiments [83, 93]. Once the crystal has formed, the pulsing is turned on.While initially trapping, ion crystal formations are observed using the EMCCD camera. For fluorescence data collection, the Tpx3 camera is used.

As soon as the pulsing has begun, if the timing of the pulses is correct, the ions become quite dark. This is because the cooling laser frequency is significantly (a few hundred MHz) red-detuned to enable continuous Doppler cooling. The main cooling beam at 493 nm must be quickly tuned up towards the resonance by $\sim$ 100 MHz. If the crystal appears bright in some areas but not others and easily melts, the phase of the pulses relative to the trap RF is incorrect causing only certain ions with the correct velocity range to fluoresce brightly. Typically, these crystals do not last long before

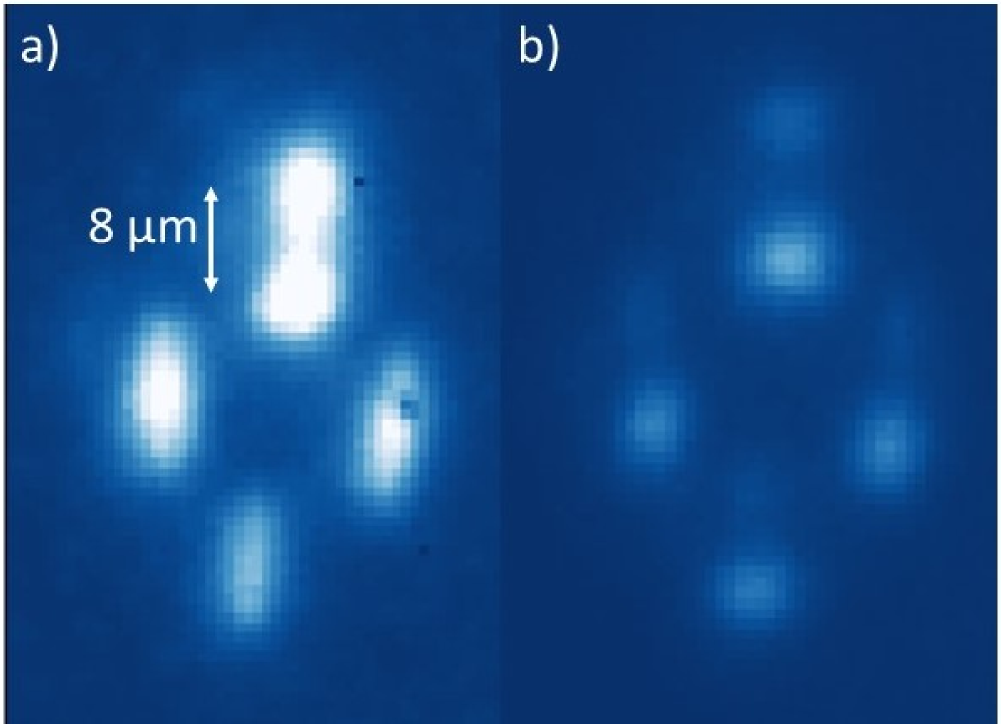

Figure 7.7: Four ions cooled with continuous illumination and by pulsed cooling. Trap frequencies are the same as in Fig. 7.6. a) Time-integrated image of the continuously cooled crystal. b) Integrated image of the crystal cooled using the pulsed method.

melting. If the relative phase is nearly correct, the crystal appears mostly uniform in brightness and does not melt, and the cooling beams are successfully illuminating ions only near $v = 0$.

To fine-tune the relative phase of the laser pulses to the trap RF, we trap and cool a single ion and displace it from the trap center by applying a bias voltage to one of the trap's sector electrodes to induce a large amount of micromotion for the ion. We then dynamically adjust the delay between the laser pulses and the trap RF zero-crossing while monitoring the ion image with the camera. The correct phase is achieved when the ion image appears as two spots corresponding to the ion positions at the micromotion extrema, as shown in the Fig. 7.5 inset. The frequencies of the cooling and repump lasers are then tuned up as far as possible towards the resonance without melting the crystal. When correctly configured, the pulses select velocities near $v = 0$ and the lasers can be tuned farthest into the blue.

We trap and cool a 28-ion, 3-shell 2D crystal centered near the trap's RF null with and without the pulsed laser method, as shown in Fig. 7.6. The cooling laser direction is vertical in the ion crystal images, and the location $y = 0$ of the trap's RF null in that direction is indicated by the dashed white line. Ions in this crystal experience micromotion up to $A \sim 1.5\ \mu m$ ($\beta = 19$), with about half the ions above the $y = 0$ line oscillating out of phase with the ions below. We observe that all ions have a relatively uniform scattering rate (and therefore brightness) when using the pulsed laser method as compared to the continuous laser cooling, where a broad variations of scattering rates are observed. We also note that scattering rates of ions above and below the $y = 0$ line (e.g. ions 1 and 7 in Fig. 7.6 (a)) are out of phase for the continuous laser cooling, as expected. For the pulsed laser cooled ions, this phase flip in fluorescence is not observed, since the scattering rate is now determined by the pulse profiles. In addition, the crystal temperature is reduced modestly from approximately 15 mK in the continuous laser cooling to 13 mK in the pulsed laser cooling case, as determined from the spatial extent of the ions [93]. We also trap and perform pulsed cooling on a 4 ion crystal displaced from the trap RF null where micromotion amplitude for one of the ions exceeds 4 μm (Fig. 7.7), corresponding to a maximum Doppler shift of $\sim$ 400 MHz and $\beta > 50$.

To fully explore the benefits of pulsed Doppler cooling, we need to reduce the pulse widths down to the limit imposed in Eq. 7.2.4. Since we are limited to $\delta t \sim 10$ ns by the available hardware, the cooling rates and the ion fluorescence profiles are still not fully uniform across crystals formed in this trap. Faster RF switches and AOMs, and lower trap RF drive frequencies may enable this region of pulsed laser cooling to be more fully investigated.

7.4 Conclusion

We have proposed and demonstrated the use of pulsed lasers to perform velocity-selective Doppler cooling of ions undergoing micromotion. The pulsed cooling allows ions with differing amounts of micromotion to be addressed by a single cooling beam, and improves the average cooling rate even when the amplitude of micromotion becomes significant. Ultimately, we are limited by available laser power and minimum pulse duration. In future experiments, we intend to use shorter laser pulses to explore the limitations of pulsed Doppler cooling.

Chapter 8

Outlook

2D crystals of trapped ions are already being pursued by many groups for quantum simulations and computation. In this work, I outlined and demonstrated two techniques for improving the Doppler cooling of large 2D crystals under micromotion. However, neither method was explored to its full extent. Multi-tone cooling may allow for a greater range of micromotion to be addressed in a 2D crystal. Moreover, different configurations of beams (i.e. counterpropagating, crossed), in addition to multiple tones, may allow for some improvements. The pulsed cooling technique was demonstrated, yet I did not get close to the limit imposed in Eq. 7.2.4. I expect that significant improvements to both experiments in chapters 6 and 7 can be made in terms of trapping infrastructure, lasers, and control electronics that will lead to cooling and trapping of 100s of ions in radial 2D crystals.

In addition to improving cooling, laser systems will need to be set up for using barium as a qubit. For example, the ground state hyperfine splitting in $^{133}\text{Ba}^{+}$ or $^{137}\text{Ba}^{+}$ are both currently being used as high-quality qubits. For Doppler cooling, electro-optic modulators are needed to span the hyperfine splitting of the ground state. And for single and two-qubit operations, Raman lasers (typically 532 nm for barium) would need to be installed. A system for spatial control of the addressing beams in 2D would be needed to focus the beams onto arbitrary ions within the crystals. I look forward to seeing further progress towards these goals both in our lab and within the ion trapping community.

Bibliography

[1] Pengfei Wang, Chun-Yang Luan, Mu Qiao, Mark Um, Junhua Zhang, Ye Wang, Xiao Yuan, Mile Gu, Jingning Zhang, and Kihwan Kim. Melting of trapped few-particle systems. *Nat Commun*, 12:233, 2021.

[2] C. D. Bruzewicz, J. Chiaverini, Robert McConnell, and J. M. Sage. Trapped-ion quantum computing: Progress and challenges. *Appl. Phys. Rev.*, 6:021314, 2019.

[3] J. W. Britton, B. C. Sawyer, A. C. Keith, J. C.-C. Wang, J. K. Freericks, M. Uys, M. J. Biercuk, and J. J. Bollinger. Engineered two-dimensional ising interactions in a trapped-ion quantum simulator with hundreds of spins. *Nature*, 484:489–492, 2012.

[4] B. C. Sawyer, J. W. Britton, A. C. Keith, C.-C. J. Wang, J. K. Freericks, H. Uys, M. J. Biercuk, and J. J. Bollinger. Spectroscopy and thermometry of drumhead modes in a mesoscopic trapped-ion crystal using entanglement. *Phys. Rev. Lett.*, 108:213003, 2012.

[5] K. A. Gilmore, M. Affolter, R. J. Lewis-Swan, D. Barberena, E. Jordan, A. M. Rey, and J. J. Bollinger. Quantum-enhanced sensing of displacements and electric fields with two-dimensional trapped-ion crystals. *Science*, 373(6555):673–678, 2021.

[6] Elena Jordan, Kevin A. Gilmore, Athreya Shankar, Arghavan Safavi-Naini, Justin G. Bohnet, Murray J. Holland, and John J. Bollinger. Near ground-state cooling of two-dimensional trapped-ion crystals with more than 100 ions. *Phys. Rev. Lett.*, 122:053603, Feb 2019.

[7] J. G. Bohnet, B. C. Sawyer, J. W. Britton, M. L. Wall, A. M. Rey, M. Foss-Feig, and J. J. Bollinger. Quantum spin dynamics and entanglement generation with hundreds of trapped ions. *Science*, 352:1297–1301, 2012.

[8] K.G. Libbrecht and E. D. Black. Improved microparticle electrodynamic ion traps for physics teaching. *Am. Jour. Phys.*, 86:539, 2018.

[9] M. G. Raizen, J. M. Gilligan, J. C. Bergquist, W. M. Itano, and D. J. Wineland. Ionic crystals in a linear paul trap. *Phys. Rev. A*, 45:6493–6501, 1992.

[10] J. D. Prestage, G. J. Dick, and L. Maleki. New ion trap for frequency standard applications. *Jour. Appl. Phys*, 66:1013, 1989.

[11] J. I. Cirac and P. Zoller. Quantum computations with cold trapped ions. *Phys. Rev. Lett.*, 74:4091–4094, 1995.

[12] C. Monroe, D. M. Meekhof, B. E. King, W. M. Itano, and D. J. Wineland. Demonstration of a fundamental quantum logic gate. *Phys. Rev. Lett.*, 75:4714–4717, 1995.

[13] E. Knill and R. Laflamme. Theory of quantum error-correcting codes. *Phys. Rev. A*, 55:900–911, 1997.

[14] P. W. Shor. Scheme for reducing decoherence in quantum computer memory. *Phys. Rev. A*, 52:R2493–R2496, 1995.

[15] L. Egan, D. M. Debroy, C. Noel, A. Risinger, D. Zhu, D. Biswas, M. Newman, M. Li, K. R. Brown, M. Cetina, and C. Monroe. Fault-tolerant control of an error-corrected qubit. *Nature*, 598:281–286, 2022.

[16] D. Porras and J. I. Cirac. Quantum manipulation of trapped ions in two dimensional coulomb crystals. *Phys. Rev. Lett.*, 96:250501, 2006.

[17] S. T. Wang, C. Shen, and L. M. Duan. Quantum computation under micromotion in a planar ion crystal. *Sci. Rep.*, 5:8555, 2015.

[18] L. Balents. Spin liquids in frustrated magnets. *Nature*, 464:199–208, 2010.

[19] R. Moessner, S. L. Sondhi, and P. Chandra. Two-dimensional periodic frustrated ising models in a transverse field. *Phys. Rev. Lett.*, 84:4457–4460, 2000.

[20] R. Nath, M. Dalmonte, A. W. Glaetzle, P. Zoller, F. Schmidt-Kaler, and F. R. Gerritsma. Hexagonal plaquette spin–spin interactions and quantum magnetism in a two-dimensional ion crystal. *New J. Phys.*, 17:065018, 2015.

[21] J. Welzel, A. Bautista-Salvador, C. Abarbanel, V. Wineman-Fisher, C. Wunderlich, R. Folman, and F. Schmidt-Kaler. Designing spin-spin interactions with one and two dimensional ion crystals in planar micro traps. *Eur. Phys. J. D*, 65:285–297, 2011.

[22] J. D. A.Espinoza, M. Mazzanti, K. Fouka, R. X. Schüssler, Z. Wu, P. Corboz, R. Gerritsma, and A. Safavi-Naini. Engineering spin-spin interactions with optical tweezers in trapped ions. *Phys. Rev. A*, 104:013302, 2021.

[23] D. Leibfried, R. Blatt, C. Monroe, and D. Wineland. Quantum dynamics of single trapped ions. *Rev. Mod. Phys.*, 75:281–324, 2003.

[24] D. J. Berkeland, J. D. Miller, J. C. Bergquist, W. M. Itano, and D. J. Wineland. Minimization of ion micromotion in a paul trap. *Journal of Applied Physics*, 83(10):5025–5033, 1998.

[25] Y. Wang, M. Qiao, Z. Cai, K. Zhang, N. Jin, P. Wang W., Chen, C. Luan, B. Du, H. Wang, Y. Song, D. Yum, and K. Kim. Coherently manipulated 2d ion crystal in a monolithic paul trap. *Adv. Quant. Tech.*, 3(11):2000068, 2020.

[26] B. Yoshimura, M. Stork, D. Dadic, W. C. Campbell, and J. K Freericks. Creation of two-dimensional coulomb crystals of ions in oblate paul traps for quantum simulations. *EPJ Quantum Technology*, 2(1):2, 2015.

[27] P. Richerme. Two-dimensional ion crystals in radio-frequency traps for quantum simulation. *Phys. Rev. A*, 94:032320, Sep 2016.

[28] Y.-K. Wu, Z.-D. Liu, W.-D. Zhao, and L.-M. Duan. High-fidelity entangling gates in a three-dimensional ion crystal under micromotion. *Phys. Rev. A*, 103:022419, 2021.

[29] R. G. DeVoe, J. Hoffnagle, and R. G. Brewer. Role of laser damping in trapped ion crystals. *Phys. Rev. A*, 39:4362–4365, 1989.

[30] Mechanical saddle demonstration. *https://www.youtube.com/watch?v=9TH5mFHLmfc*, 2016.

[31] R. F. Wuerker, H. Shelton, and R. V. Langmuir. Theory of quantum error-correcting codes. *Jour. Appl. Phys.*, 39:342, 1959.

[32] A. Kleczewski. *Towards a measurement of the nuclear magnetic octupole moment of barium-137*. PhD thesis, Seattle, WA, 2011.

[33] M. Hoffman. *Observation of the Nuclear Magnetic Octupole Moment of 137Ba+*. PhD thesis, Seattle, WA, 2014.

[34] Wolfgang Paul. Electromagnetic traps for charged and neutral particles. *Rev. Mod. Phys.*, 62:531–540, 1990.

[35] N. W. McLachlan. *Theory and application of Mathieu functions*. Clarendon Press, 1951.

[36] Daniel H. E. Dubin. *Phys. Rev. Lett.*, 71:2753–2756, 1993.

[37] M. Dietrich. *Barium Ions for Quantum Computation*. PhD thesis, Seattle, WA, 2009.

[38] T. Noel. *Ion Photon Entanglement with Barium*. PhD thesis, Seattle, WA, 2014.

[39] L. Zhukas. *Novel Methods in Trapped-Ion Quantum Computing: Single-Photon-Sensitive Time-Resolving Camera, Sympathetic Cooling, and Qutrit*. PhD thesis, Seattle, WA, 2021.

[40] M. Fan, C.A. Holliman, A.L. Wang, and A.M. Jayich. Theory of quantum error-correcting codes. *Phys. Rev. Lett.*, 122:223001, 2019.

[41] D. J. Wineland, R. E. Drullinger, and F. L. Walls. Radiation-pressure cooling of bound resonant absorbers. *Phys. Rev. Lett.*, 40:1639, 1978.

[42] M. Hohenstatt W. Neuhauser, P. Toschek, and H. Dehmelt. Optical-sideband cooling of visible atom cloud confined in parabolic well. *Phys. Rev Lett.*, 42:223, 1978.

[43] S. Foot. *Atomic Physics*. Oxford University Press, Oxford, UK, 2005.

[44] H. J. Metcalf and P. van der Straten. Laser cooling and trapping of atoms. *J. Opt. Soc. Am.*, 20:887–908, 2003.

[45] D. J. Berkeland and M. G. Boshier. Destabilization of dark states and optical spectroscopy in zeeman-degenerate atomic systems. *Phys. Rev. A.*, 65:033413, 2002.

[46] H. Oberst. Resonance fluorescence of single barium ions. Master's thesis, Innsbruck, Austria, 1999.

[47] D. J. Wineland, J. C. Bergquist, Wayne M. Itano, J. J. Bollinger, and C. H. Manney. Atomic-ion coulomb clusters in an ion trap. *Phys. Rev. Lett.*, 59:2935–2938, Dec 1987.

[48] F. Diedrich, E. Peik, J. M. Chen, W. Quint, and H. Walther. Observation of a phase transition of stored laser-cooled ions. *Phys. Rev. Lett.*, 59:2931–2934, 1987.

[49] J. Hoffnagle R. G. DeVoe, L. Reyna, and R. G. Brewer. Order-chaos transition of two trapped ions. *Phys. Rev. Lett.*, 61:255–258, 1988.

[50] M. Block, A. Drakoudis, H. Leuthner, P. Seibert, and G. Werth. Crystalline ion structures in a paul trap. *J. Phys. B.: Atom. Mol. Opt. Phys.*, 33(11):L375–L382, 2000.

[51] I. M. Buluta, M. Kitaoka, S. Georgescu, and S. Hasegawa. Investigation of planar coulomb crystals for quantum simulation and computation. *Phys. Rev. A*, 77:062320, 2008.

[52] I. M. Buluta and S. Hasegawa. The structure of planar coulomb crystals in RF traps. 42(15):154004, 2009.

[53] L. L. Yan, W. Wan, L. Chen, F. Zhou, S. J. Gong, X. Tong, and M. Feng. Exploring structural phase transitions of ion crystals. *Sci Rep*, 6:21547, 2016.

[54] K. Okada, M. Wada, T. Takayanagi, S. Ohtani, and H. A. Schuessler. Characterization of ion coulomb crystals in a linear paul trap. *Phys. Rev. A*, 81:013420, Jan 2010.

[55] M. D'Onofrio, Y. Xie, A. J. Rasmusson, E. Wolanski, J. Cui, and P. Richerme. Radial two-dimensional ion crystals in a linear paul trap. *Phys. Rev. Lett.*, 127:020503, 2021.

[56] M. Qiao, Y. Wang Ye, Z. Cai, B. Du, P Wang, C. Luan, W.Chen, H.-R. Noh, and K. Kim. Double-electromagnetically-induced-transparency ground-state cooling of stationary two-dimensional ion crystals. *Phys. Rev. Lett.*, 126:023604, 2021.

[57] Y. Xie, J. Cui, M. D'Onofrio, A. J. Rasmusson, S. W. Howell, and P. Richerme. An open-endcap blade trap for radial-2d ion crystals. 6(4):044009, 2021.

[58] M. K. Joshi, A. Fabre, C. Maier, T. Brydges, D. Kiesenhofer, H. Hainzer, R. Blatt, and C. F. Roos. Polarization-gradient cooling of 1d and 2d ion coulomb crystals. *New J. Phys.*, 22:103013, 2020.

[59] H. Hainzer, D. Kiesenhofer, T. Ollikainen, M. Bock, F. Kranzl, M. K. Joshi, G. Yoeli, R. Blatt, T. Gefen, and C. F. Roos. Correlation spectroscopy with multi-qubit-enhanced phase estimation. *arXiv*, 2203.126567, 2022.

[60] J. M. Kosterlitz and D. J. Thouless. Long range order and metastability in two dimensional solids and superfluids. *J. Phys. C.: Solid State Phys*, 5:2935–2938, 1972.

[61] V. M. Bedanov and F. M. Peeters. Ordering and phase transitions of charged particles in a classical finite two-dimensional system. *Phys. Rev. B*, 49:2667–2676, 1994.

[62] V.A. Mandelshtam Y.E. Lozovik. Classical and quantum melting of a coulomb cluster in a trap. *Phys. Lett. A*, 165:062320, 1992.

[63] J. Böning, A. Filinov, P. Ludwig, H. Baumgartner, M. Bonitz, and Yu. E. Lozovik. Melting of trapped few-particle systems. *Phys. Rev. Lett.*, 100:113401, 2008.

[64] A. Melzer, A. Schella, J. Schablinski, D. Block, and A. Piel. Instantaneous normal mode analysis of melting of finite dust clusters. *Phys. Rev. Lett.*, 108:225001, 2012.

[65] L. Duca, N. Mizukami, E. Perego M. Inguscio, and C. Sias. Orientational melting in a mesoscopic system of charged particles, 2022.

[66] J. Lilieholm. *Experiments with Trapped Ions: Entanglement, Novel Traps, and Quantum Jumps*. PhD thesis, Seattle, WA, 2020.

[67] Crystal Technologies. Ao modulator data sheet 3200-1115. 2002.

[68] J. D. Siverns, L. R. Simkins, S. Weidt, and W. K. Hensinger. On the application of radio frequency voltages to ion traps via helical resonators. *Appl. Phys. B*, 107:921–934, 2012.

[69] W. W. Macalpine and R. O. Schildknecht. Coaxial resonators with helical inner conductor. *Proc. of theIRE*, 47:2099–2105, 1959.

[70] L. A. Zhukas, P. Svihra, A. Nomerotski, and B. B. Blinov. High-fidelity simultaneous detection of a trapped-ion qubit register. *Phys. Rev. A*, 103:062614, 2021.

[71] C. Ianzano, P. Svihra, M. Flament, A. Hardy, G. Cui, A. Nomerotski, and E. Figueroa. Fast camera spatial characterization of photonic polarization entanglement. *Scientific Reports*, 10(1):6181, 2020.

[72] A. Nomerotski, M. Keach, P. Stankus, P. Svihra, and S. Vintskevich. Counting of hong-ou-mandel bunched optical photons using a fast pixel camera. *Sensors*, 20(12):3475, 2020.

[73] Y. Zhang, D. England, P. Nomerotski, A.and Svihra, P. Ferrante, S.and Hockett, and B. Sussman. Multidimensional quantum-enhanced target detection via spectrotemporal-correlation measurements. *Phys. Rev. A*, 101:053808, 2020.

[74] Y. Zhang, D. England, A. Nomerotski, and B. Sussman. High speed imaging of spectral-temporal correlations in hong-ou-mandel interference. *Opt. Express*, 29(18):28217–28227, 2021.

[75] A. Nomerotski, I. Chakaberia, M. Fisher-Levine1, Z. Janoska, P. Takacs, and T. Tsang. Characterization of timepixcam, a fast imager for the time-stamping of optical photons. *JINST*, 12, 2017.

[76] T. Poikela, J. Plosila, T. Westerlund, M. Campbell, M. De Gaspari, X. Llopart, V. Gromov., R. Kluit, M. van Beuzekom, and F. Zappon. Timepix3: a 65k channel hybrid pixel readout chip with simultaneous toa/tot and sparse readout. *JINST*, 9, 2014.

[77] M. Fisher-Levine and A. Nomerotski. TimepixCam: a fast optical imager with time-stamping. *JINST*, 11(03):C03016, 2016.

[78] A. Nomerotski. Imaging and time stamping of photons with nanosecond resolution in timepix based optical cameras. *Nucl. Inst. Methods A*, 937:26–30, 2019.

[79] L. A. Zhukas, M.J. Millican, P. Svihra, A. Nomerotski, and B. B. Blinov. Direct observation of ion micromotion in a linear paul trap. *Phys. Rev. A*, 103:023105, 2021.

[80] B. van der Heijden, J. Visser, M. van Beuzekom, H. Boterenbrood, S. Kulis, B. Munnek, and F. Schreuder. Spidr, a general-purpose readout system for pixel asics. *JINST*, 12, 2017.

[81] Spinmob wiki. https://github.com/Spinmob/spinmob/wiki.

[82] C.-K. Chou, C. Auchter, J. Lilieholm, K. Smith, and B. B Blinov. Note: Single ion imaging and fluorescence collection with a parabolic mirror trap. *Review of Scientific Instruments*, 88(8):086101, 2017.

[83] M. K. Ivory, A. Kato, A. Hasanzadeh, and B. B. Blinov. A paul trap with sectored ring electrodes for experiments with two-dimensional ion crystals. *Review of Scientific Instruments*, 91(5):053201, 2020.

[84] L. Oden. Lessons learned from comparing c-cuda and python-numba for gpu-computing. *28th Euromicro Int. Con. on Parallel, Distributed and Network-Based Processing*, pages 216–223, 2020.

[85] C. B. Zhang, D. Offenberg, B. Roth, M. A. Wilson, and S. Schiller. Molecular-dynamics simulations of cold single-species and multispecies ion ensembles in a linear paul trap. *Phys. Rev. A*, 76:012719, 2007.

[86] M. Marciante, C. Champenois, A. Calisti, J. Pedregosa-Gutierrez, and M. Knoop. Ion dynamics in a linear radio-frequency trap with a single cooling laser. *Phys. Rev. A*, 82:033406, 2010.

[87] Y. Wu. *Quantum Computation in Large Ion Crystals*. PhD thesis, Ann Arbor MI, 2019.

[88] F. F. Munarin, K. Nelissen, W. P. Ferreira, G. A. Farias, and F. M. Peeters. Hysteresis and reentrant melting of a self-organized system of classical particles confined in a parabolic trap. *Phys. Rev. E*, 77:031608, 2008.

[89] H. Landa, M. Drewsen, B. Reznik, and A. Retzker. Modes of oscillation in radiofrequency paul traps. 14(9):093023, 2012.

[90] W. M. Itano, J. C. Bergquist, and D. J. Wineland. Coulomb clusters of ions in a paul trap. *Proc. of the Workshop on Crystalline Ion Beams*, page 241, 1989.

[91] H. Kaufmann, S. Ulm, G. Jacob, U. Poschinger, H. Landa, A. Retzker, M. B. Plenio, and F. Schmidt-Kaler. Precise experimental investigation of eigenmodes in a planar ion crystal. *Phys. Rev. Lett.*, 109:263003, 2012.

[92] B. Szymanski, R. Dubessy, B. Dubost, S. Guibal, J.-P. Likforman, and L. Guidoni. Large two dimensional coulomb crystals in a radio frequency surface ion trap. *Applied Physics Letters*, 100(17):171110, 2012.

[93] A. Kato, A. Goel, R. Lee, Z. Ye, S. Karki, J. J. Liu, A. Nomerotski, and B. B. Blinov. Two-tone doppler cooling of radial two-dimensional crystals in a radio-frequency ion trap. *Phys. Rev. A*, 105:023101, 2022.

[94] T. Sikorsky, Z. Meir, N. Akerman, R. Ben-Shlomi, and R. Ozeri. Doppler cooling thermometry of a multilevel ion in the presence of micromotion. *Phys. Rev. A*, 96:012519, 2017.

[95] B. B. Blinov, Jr. R. N. Kohn, M. J. Madsen, P. Maunz, D. L. Moehring, and C. Monroe. Broadband laser cooling of trapped atoms with ultrafast pulses. *J. Opt. Soc. Am. B*, 23(6):1170–1173, 2006.

[96] J. Davila-Rodriguez, A. Ozawa, T. W. Hänsch, and T. Udem. Doppler cooling trapped ions with a uv frequency comb. *Phys. Rev. Lett.*, 116:043002, 2016.

[97] A. M. Jayich, X. Long, and W. C. Campbell. Direct frequency comb laser cooling and trapping. *Phys. Rev. X*, 6:041004, 2016.

VITA

Alex grew up on Bowen Island and spent his childhood and teenage years in the woods. Here, he attended Bowen Island Community School. Alex then attended West Vancouver Secondary School and took the ferry too many times back and forth. After graduating, Alex attended McGill University where he had his butt kicked in the honours physics program. After graduating from university, Alex moved with his wife, Audrey, to Boulder, Colorado, where they had some fun in the mountains and began careers. Alex worked as an engineer at ColdQuanta, gaining exposure in atomic physics and quantum computing. Through his tenure here, Alex also met many ion trappers, who inspired him to continue his education. In 2018, Alex moved to Seattle and enrolled in the physics program at the University of Washington, where he started working in Boris Blinov's lab.